# Precision Neutrino Oscillations: Important Considerations for Experiments

Rebekah Faith Pestes

Dissertation submitted to the Faculty of the
Virginia Polytechnic Institute and State University
in partial fulfillment of the requirements for the degree of

Doctor of Philosophy
in
Physics

Patrick Huber, Chair
Shunsaku Horiuchi
Camillo Mariani
Tatsu Takeuchi

April 16, 2021
Blacksburg, Virginia

Keywords: Theoretical High Energy Physics, Simulating Neutrino Experiments, Parameterizing the Mixing Matrix, Artificial Sources, Reactor Antineutrino Anomaly

# Precision Neutrino Oscillations: Important Considerations for Experiments

Rebekah Faith Pestes

(ABSTRACT)

Currently, we are in an era of neutrino physics in which neutrino oscillation experiments are focusing on doing precision measurements. In this dissertation, we investigate what is important to consider when doing these precise experiments, especially in light of significant unresolved anomalies. We look at four general categories of considerations: systematic uncertainties, fundamental assumptions, parameterization-dependence of interpretations, and Beyond the Standard Model (BSM) scenarios. By performing a simulation using GLoBES, we find that uncertainties in the fine structure of the reactor neutrino spectrum could be vitally important to JUNO, a reactor neutrino experiment being built in China, so a reference spectrum with comparable energy resolution to JUNO is needed in order to alleviate this uncertainty. In addition, we determine that with their fix of the fine structure problem, JUNO can test the existence of a quantum interference term in the oscillation probability. We also reason that the $CP$-violating phase is very parameterization dependent, and the Jarlskog invariant is better for talking about amounts of $CP$ violation in neutrino oscillations. Finally, we discover that $CP$-violating neutrino Non-Standard Interactions (NSIs) could already be affecting the outcomes of T2K and NO$\nu$A, two accelerator neutrino experiments, and may be why there is a tension in these two data sets.

# Precision Neutrino Oscillations: Important Considerations for Experiments

Rebekah Faith Pestes

(GENERAL AUDIENCE ABSTRACT)

Neutrinos are very weakly interacting, fundamental particles that are extremely plentiful in the universe. There are three known types (or flavors) of neutrinos, and the fact that they change flavors (or oscillate) informs us that their mass is not zero, but no experiments have been able to put a lower bound on the smallest neutrino mass. Now that experiments measuring neutrino oscillations have become more precise and some significant anomalies remain unresolved, there are considerations that have become important to investigate. In this paper, we look at four of these considerations:

- Uncertainties in the finer shapes in the energy spectrum of neutrinos coming from a nuclear reactor (Chapter 2): We find that these uncertainties could destroy the ability of the Jiangmen Underground Neutrino Observatory (JUNO) to meet one of its major goals, unless they measured the spectrum at a spot close to the reactor with a really good energy resolution (comparable to that of JUNO).
- An assumption about quantum mechanics being the foundation of particles and their interactions (Chapter 3): We determine that by heeding our warning in Chapter 2, JUNO will be able to test the existence of the term in the oscillation probability arising out of quantum interference.

- How the neutrino oscillation parameter known as the $CP$-violating phase is dependent on the parameterization scheme used for the matrix describing how the flavors mix to make neutrino oscillation possible (Chapter 4): We find that the parameterization dependence is drastic, and if we want to discuss how much $CP$ violation (i.e. a measure of how neutrinos behave differently from their anti-matter counterparts) exists in neutrino oscillations, we should talk about a quantity called the Jarlskog invariant.

- The possibility of interactions existing between neutrinos and other particles that are not part of the Standard Model of Particle Physics, i.e. neutrino Non-Standard Interactions (NSIs) (Chapter 5): We discover that NSIs that are $CP$-violating can actually explain a current discrepancy between two neutrino oscillation experiments: Tokai to Kamioka Nuclear Decay Experiment (T2K) and NuMI Off-axis $\nu_e$ Appearance (NO$\nu$A).

# Acknowledgments

I would like to thank the U.S. Department of Energy (DOE) for funding the research I did at Virginia Tech, as well as sponsoring me for a year to participate in the DOE Office of Science Graduate Student Research (SCGSR) program.

My sincere gratitude goes out to my advisor Dr. Patrick Huber for lending me his expertise by guiding me and helping me find the "little" programming mistakes that crashed my code and gave nonsense results. I am particularly thankful for the career advice he has given me and his role in connecting me with other neutrino theorists. Also, I am extremely grateful to my SCGSR program collaborating scientist Dr. Peter Denton, who continues to go out of his way to encourage and advise me.

I wish to thank my collaborators Dr. Hisakazu Minakata, Dr. Julia Gehrlein, and Dr. David Forero for teaching me, assisting me with checking and debugging my code, and drawing me out of working alone. I also want to thank Dr. Zahra Tabrizi for volunteering to read my dissertation and advise me on it, as well as my committee members Dr. Shunsaku Horiuchi, Dr. Camillo Mariani, and Dr. Tatsu Takeuchi for finding all my typos and sharing ways to improve my dissertation.

I appreciate my fellow graduate students, especially Kate Pitchford and Jason Czak, for being ready to listen when I needed to let out my excitement or frustration. Also, I am thankful for my husband Jonathan Pestes, who has been a support for me, stepping in for

me at home when work demanded my attention and suggesting creative solutions when I asked for advice. I wish to acknowledge my mother Charlene Hawkins, too, for her listening ear and helpful advice, as well as the rest of my family for their words of encouragement. Most importantly, I am eternally grateful for the strength, guidance, and provisions God has given me throughout the whole process of earning a PhD.

# Contents

# List of Figures

# List of Tables

# Chapter 1

# Introduction

## 1.1 Neutrinos

In the early 1900's, there were a number of experiments investigating beta decay for various radioactive isotopes [3], which was thought to be given by the formula

$$ {}^{A}_{Z}\mathrm{X} \rightarrow {}^{A}_{Z+1}\mathrm{X}' + e^{-} \,, \tag{1.1} $$

where $A$ and $Z$ are the atomic mass and atomic number of the radioactive isotope $X$ (whose nucleus is called the parent nucleus), $X'$ (whose nucleus is called the daughter nucleus) is the element that is produced by the decay of $X$, and $e^{-}$ is an electron. If this formula was correct, then the electron would carry away all of the difference in energy between the daughter and parent nuclei, so the energy spectrum of the outgoing electrons from beta decays of a single isotope would be mono-energetic. Instead, the experiments observed a continuous electron energy spectrum with a maximum where they thought the mono-energetic line should be [4],

as expressed by

$$ {}^{A}_{Z}\mathrm{X} \rightarrow {}_{Z+1}{}^{A}\mathrm{X}' + e^{-} + (\text{missing energy})\,. \tag{1.2} $$

In 1930, Wolfgang Pauli proposed that an undetected neutral particle was taking away the missing energy, so Eq. (1.2) would be replaced by

$$ {}^{A}_{Z}\mathrm{X} \rightarrow {}_{Z+1}{}^{A}\mathrm{X}' + e^{-} + \bar{\nu}\,, \tag{1.3} $$

where $\bar{\nu}$ is the proposed particle. Since the maximum energy in the electron spectrum was consistent with all the energy difference between the two nuclei, this particle, later named a neutrino by Enrico Fermi [5], would need to have very little, if any, mass. Also, neutrinos would need to have really high penetrating power in order to escape detection by any of the beta decay experiments, so of the forces in the Standard Model of Particle Physics (SM), the weak nuclear force would be the only one to which neutrinos are sensitive. While this makes them very difficult to detect, it is not impossible to observe them, as was shown by the first confirmed detection of neutrinos from a nuclear reactor by Clyde Cowan and Frederick Reines in 1956 [6].

Once muons were discovered and it was determined that a neutrino was produced along with the muon in pion decay (i.e. the formula for the decay of a pion $\pi^{-}$ is

$$ \pi^{-} \rightarrow \mu^{-} + \bar{\nu}\,, \tag{1.4} $$

where $\bar{\nu}$ is an antineutrino), the question arose of whether these neutrinos were the same as the neutrinos in Eq. (1.3). So, a group at Brookhaven National Lab used a pion beam to produce "muon neutrinos" via Eq. (1.4) and detected them in a 10 ton spark chamber via the interaction below:

$$ \bar{\nu} + p^{+} \rightarrow n^{0} + \mu^{+}\,, \tag{1.5} $$

where $p^+$ is a proton and $n^0$ is a neutron. If the neutrinos in Eqs. (1.3) and (1.4) are the same, then positrons ($e^+$) would also be expected to be detected from the following interaction in the detector:

$$\bar{\nu} + p^+ \rightarrow n^0 + e^+ \,. \tag{1.6}$$

In the experiment, they observed that there were only muons produced in interactions of the neutrinos with the detector. Thus, in 1962, this group confirmed that electron neutrinos and muon neutrinos are distinct particles [7], and "electron" and "muon" became known as the "flavor" of the respective types of neutrinos. A third flavor of neutrinos (tau neutrinos) was not positively detected until 2001 [8], though its existence was assumed long before that.

An interesting question to think about is whether there might be more flavors of neutrinos than the three in the SM. This is a question that the Large-Electron Positron Collider (LEP) at the European Organization for Nuclear Research (CERN) aimed at addressing. The half-life of the $Z^0$ boson, which can be determined from the width of the $Z^0$ boson resonance, depends on how many types of neutrinos with a smaller mass than half of the $Z^0$ boson's mass interacted with it. So, in measuring the width of the $Z^0$ boson resonance, the four experiments at LEP were able to determine that the number of light (i.e. less mass than half of $Z^0$'s mass), active (i.e. participate in weak interactions) neutrinos must be 3 [9–12]. The combined measured value for the number of light, active neutrinos is $2.984 \pm 0.008$ [13].

### 1.1.1 Neutrino Detectors

There are two type of weak interactions that neutrinos have with matter: neutral current (NC) interactions and charged current (CC) interactions. In NC interactions, an incoming (anti)neutrino exchanges a $Z^0$ boson with another fermion (see Fig. 1.1). All that may be detectable from this is the fermion's change in momentum; no information about the

neutrino's flavor can be known. In CC interactions, an incoming (anti)neutrino becomes a lepton of the corresponding flavor ($e$, $\mu$, $\tau$) through the exchange of a $W^+$ (or $W^-$) boson with another fermion (see Fig. 1.2). The detector observes the lepton produced in this interaction. For a CC interaction to be possible, the neutrino must have at least as much energy as the mass of its corresponding charged lepton. In most situations, neutrinos are traveling and interacting with "ordinary matter," which is the matter that makes up atoms (i.e. up quarks, down quarks, and electrons).

When Cowan and Reines conducted the experiment that first confirmed the existence of neutrinos, they used a layered setup with a target of cadmium chloride in water and a liquid scintillator with photomultiplier tubes (PMTs) [6]. An electron antineutrino ($\bar{\nu}_e$) from the nuclear reactor would interact with a proton in the target via inverse beta decay, which follows this equation:

$$\bar{\nu}_e + p^+ \rightarrow e^+ + n^0 \,. \tag{1.7}$$

The positron produced would annihilate with an electron in the detector, producing gamma rays that would be absorbed and reemitted by the scintillator and detected by the PMTs. The neutron would be captured by the cadmium, producing a gamma+ ray burst that would also be detected by the scintillator/PMT combination. The coincidence of these two specific signals is what was searched for in order to have a confirmed electron antineutrino detection.

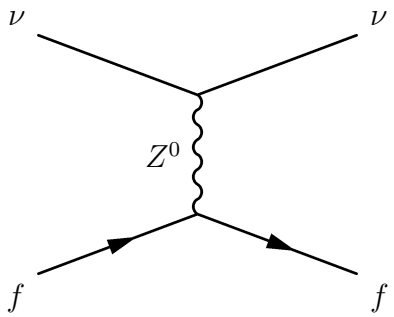


Figure 1.1: Sample neutral current neutrino interactions with matter. The neutrino can be any flavor of neutrino or antineutrino and $f$ is any fermion in the matter (for ordinary matter, $f = u$,$d$,$e^-$).

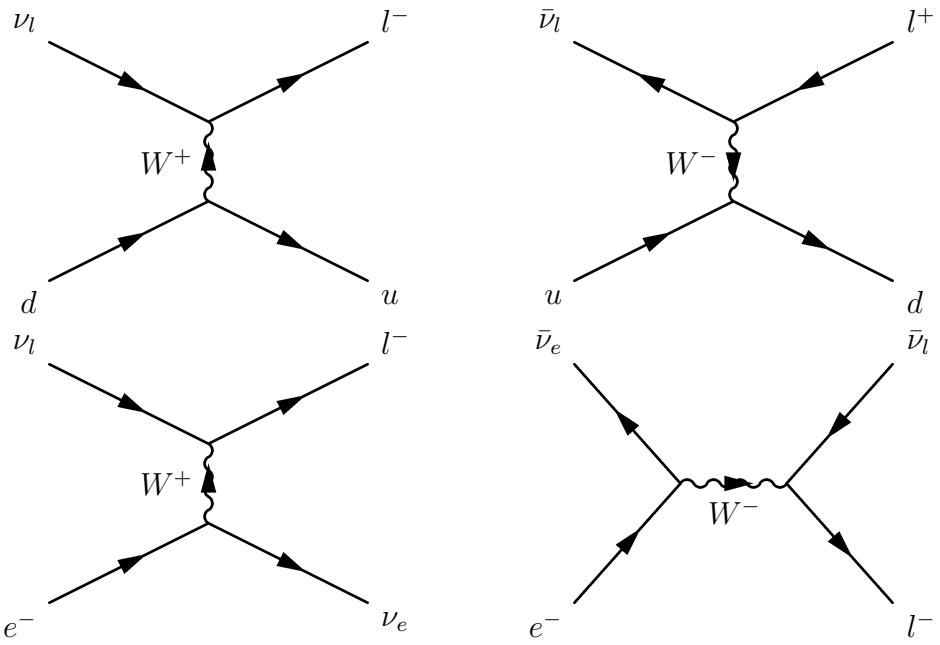


Figure 1.2: Sample charged current neutrino interactions with ordinary matter. The flavor of lepton $l$ can be $e$, $\mu$, or $\tau$.

Neutrino detectors can also use a liquid scintillator as the target medium.

Spark chambers are another early method used to detect the charged lepton produced from a CC interaction [7]. The spark chamber contained aluminum plates and was filled with neon. A charged particle passing through would ionize the neon, and then a high voltage would be applied to the spark chamber, which would make sparks where the ions were.

Another type of neutrino detector that is commonly used today is a water Cherenkov detector. When a neutrino interacts with the water via a CC interaction, the corresponding charged lepton will produce Cherenkov radiation if it is moving faster than the speed of light in water. The fuzziness of the circle of light detected by the PMTs indicates the flavor of the charged lepton. The IceCube Neutrino Observatory, a $\sim 1\,\mathrm{km}^3$ detector in Antarctica, is an example of a water Cherenkov detector that uses ice, instead of liquid water, to observe atmospheric and astrophysical neutrinos. Instead of having PMTs surrounding the detector volume like most other neutrino detectors, the IceCube experiment basically consists of

strings with evenly spaced PMTs that are lowered into the ice primarily in a hexagonal grid pattern.

Liquid argon is another material that can be used as a target material for neutrino detectors to make a time projection chamber. Charged particles produced from the neutrino interaction ionize the argon as they travel through the detector, and the electrons produced thereby drift under the influence of an electric field to a wire, where they produce a current pulse.

## 1.2 Neutrino Oscillation

With multiple distinct flavors of neutrinos comes the possibility that the neutrino mass eigenstates are not equivalent to the flavor eigenstates, as is the case with quarks. This possibility requires that the neutrino masses be different from one another, so not all of the neutrinos could be massless, and results in the neutrinos changing flavor as they propagate, a phenomenon called neutrino oscillation. In 1957, Bruno Pontecorvo was the first to propose the idea that neutrinos might oscillate, though in that paper, he just looked at neutrino-antineutrino oscillation [14]. After it was known that there are more than one flavor of neutrinos, Ziro Maki, Masami Nakagawa, and Shoichi Sakata proposed a two flavor version of the phenomenon of neutrino oscillation described below [15].

### 1.2.1 Neutrino Mixing Matrix

To parameterize the differences between the mass and flavor eigenstates, we use the neutrino mixing matrix $U$, also called the Pontecorvo-Maki-Nakagawa-Sakata (PMNS) matrix, as follows:

$$|\nu_\alpha\rangle = U^*_{\alpha i} |\nu_i\rangle \ , \tag{1.8}$$

where $|\nu_\alpha\rangle$ for $\alpha = e, \mu, \tau$ are the flavor eigenstates and $|\nu_i\rangle$ for $i = 1, 2, 3$ are the mass eigenstates (with eigenvalues $m_i$ for $i = 1, 2, 3$, respectively). We define the mass eigenstates such that $|U_{e1}| > |U_{e2}| > |U_{e3}|$. In general, the elements of $U$ can be complex, and the size of $U$ would need to increase if there are more flavors of neutrinos that mix with the three flavors in the SM. Thus, if we assume that there are only three neutrino flavors and that energy conservation still holds, $U$ should be a unitary matrix. A discussion of how we parameterize this matrix can be found in Section 4.2.3. The result (when assuming $U$ to be unitary and only using the parameters that affect neutrino oscillation) is a matrix with four independent parameters: 3 mixing angles ($\theta_{12}$, $\theta_{13}$, $\theta_{23}$) and 1 phase ($\delta$), in the parameterization used by the Particle Data Group (PDG) [13]. The PDG parameterization of $U$ is

$$U_{\text{PDG}} = \begin{bmatrix} c_{12}c_{13} & s_{12}c_{13} & s_{13}e^{-i\delta} \\ -s_{12}c_{23} - c_{12}s_{13}s_{23}e^{i\delta} & c_{12}c_{23} - s_{12}s_{13}s_{23}e^{i\delta} & c_{13}s_{23} \\ s_{12}s_{23} - c_{12}s_{13}c_{23}e^{i\delta} & -c_{12}s_{23} - s_{12}s_{13}c_{23}e^{i\delta} & c_{13}c_{23} \end{bmatrix}, \tag{1.9}$$

where $c_{ij} \equiv \cos(\theta_{ij})$ and $s_{ij} \equiv \sin(\theta_{ij})$.

### 1.2.2 Oscillation Probability in Vacuum

Assuming $m_i \ll E$ (where $E$ is the neutrino's energy), the Hamiltonian in the mass basis for three flavors of neutrinos in a vacuum is

$$H_{\text{vac}} = \frac{1}{2E}\begin{bmatrix} m_1^2 & 0 & 0 \\ 0 & m_2^2 & 0 \\ 0 & 0 & m_3^2 \end{bmatrix} = \frac{1}{2E}\begin{bmatrix} 0 & 0 & 0 \\ 0 & \Delta m_{21}^2 & 0 \\ 0 & 0 & \Delta m_{31}^2 \end{bmatrix} + \frac{m_1^2}{2E} I_3 \,, \tag{1.10}$$

where $m_i$ is the mass of $|\nu_i\rangle$, $\Delta m^2_{ij} \equiv m^2_i - m^2_j$ for $i, j = 1, 2, 3$ are the neutrino mass-squared differences, and $I_3$ is the $3 \times 3$ identity matrix. Terms in the Hamiltonian that are proportional to the identity matrix can be dropped, since they evolve the three mass eigenstates with the same phase, thereby canceling out the oscillation probability. Now, in the basis of eigenstates of the Hamiltonian (in this case, the mass basis), neutrinos propagate as plane waves, obeying the equation $|\nu_i(t)\rangle = e^{-iHt}\,|\nu_i\rangle$. So, a neutrino of flavor $\alpha$ propagates in a vacuum as follows:

$$|\nu_\alpha(t)\rangle = \sum_i U^*_{\alpha i}\,|\nu_i(t)\rangle = \sum_i U^*_{\alpha i} e^{-iH_{\text{vac}}t}\,|\nu_i\rangle = \sum_i U^*_{\alpha i} e^{-im_i^2 t/(2E)}\,|\nu_i\rangle\ . \tag{1.11}$$

Since we are assuming that $E \gg m_i$, the speed of the neutrino is approximately equal to the speed of light, so the distance traveled by the neutrino is equivalent (in Gaussian units) to the time it took to travel that distance. Thus, the probability that a neutrino produced as flavor $\alpha$ with energy $E \gg m$ will be detected as flavor $\beta$ when it interacts with a detector a distance $L$ from the source is

$$P_{\alpha\to\beta} = |\langle\nu_\beta|\nu_\alpha(t)\rangle|^2 = \left|\sum_{i,j} \langle\nu_j|\,U_{\beta j} e^{-im_i^2 L/(2E)} U^*_{\alpha i}\,|\nu_i\rangle\right|^2 \equiv |S_{\beta\alpha}|^2 \tag{1.12}$$

$$= \sum_i |U_{\alpha i}|^2 |U_{\beta i}|^2 + 2\sum_{i>j} \text{Re}[U_{\alpha i} U^*_{\alpha j} U^*_{\beta i} U_{\beta j}] \cos\left(\frac{\Delta m^2_{ij} L}{2E}\right) + 2\sum_{i>j} \text{Im}[U_{\alpha i} U^*_{\alpha j} U^*_{\beta i} U_{\beta j}] \sin\left(\frac{\Delta m^2_{ij} L}{2E}\right), \tag{1.13}$$

where $S_{\beta\alpha}$[1] is known as the oscillation amplitude. Oftentimes, the symbol $\Delta_{ij}$ is used to simplify the expressions inside the trigonometric functions (i.e. $\Delta_{ij} \equiv \frac{\Delta m^2_{ij}}{2E}$ or $\Delta_{ij} \equiv \frac{\Delta m^2_{ij}}{4E}$). Since there are differences in the literature as to how $\Delta_{ij}$ is defined, I have chosen not to use this substitution in this chapter, but it will be used in later sections.

[1]The definition of the oscillation amplitude found in Eq. (1.12) is important for Chapter 3.

For anti-neutrinos, $CPT$ symmetry, which is a fundamental symmetry of the Standard Model, dictates that $P_{\bar{\alpha}\to\bar{\beta}} = P_{\beta\to\alpha}$. So, since $\mathrm{Re}[U_{\beta i}U^*_{\beta j}U^*_{\alpha i}U_{\alpha j}] = \mathrm{Re}[U_{\alpha i}U^*_{\alpha j}U^*_{\beta i}U_{\beta j}]$ and $\mathrm{Im}[U_{\beta i}U^*_{\beta j}U^*_{\alpha i}U_{\alpha j}] = -\mathrm{Im}[U_{\alpha i}U^*_{\alpha j}U^*_{\beta i}U_{\beta j}]$, the probability that an antineutrino produced as flavor $\alpha$ with energy $E \gg m$ will be detected as flavor $\beta$ when it interacts with a detector a distance $L$ from the source is

$$P_{\bar{\alpha}\to\bar{\beta}} = \sum_i |U_{\alpha i}|^2|U_{\beta i}|^2 + 2\sum_{i>j}\mathrm{Re}[U_{\alpha i}U^*_{\alpha j}U^*_{\beta i}U_{\beta j}]\cos\left(\frac{\Delta m^2_{ij}L}{2E}\right) - 2\sum_{i>j}\mathrm{Im}[U_{\alpha i}U^*_{\alpha j}U^*_{\beta i}U_{\beta j}]\sin\left(\frac{\Delta m^2_{ij}L}{2E}\right). \tag{1.14}$$

Notice that the sign of the third term is the only difference between the oscillation probability expressions for neutrinos, Eq. (1.13), and antineutrinos, Eq. (1.14). It turns out that the value $J \equiv \mathrm{Im}[U_{\alpha i}U^*_{\alpha j}U^*_{\beta i}U_{\beta j}]$ is the same for any values of $\alpha \neq \beta$ and $i \neq j$, up to a negative sign. The quantity $J$ is called the Jarlskog invariant and is discussed more in Section 4.2. If the elements of $U$ are real, the Jarlskog invariant would be zero, and thus, neutrinos and antineutrinos would have the same oscillation probability, that is, $CP$ symmetry would not be violated in neutrino oscillation. In the parameterization of $U$ used by the Particle Data Group ($U_{\mathrm{PDG}}$) [13], there is only one complex phase ($\delta$, shown in Eq. (1.9)) that affects neutrino oscillation, so it is commonly called the "$CP$-violating phase." It turns out that the Jarlskog invariant for $U_{\mathrm{PDG}}$ contains all the parameters of $U_{\mathrm{PDG}}$, so all the mixing angles in $U_{\mathrm{PDG}}$ also need to be non-zero in order for $CP$ violation to exist in neutrino oscillation.

### 1.2.3 Oscillation Probability in Matter

When neutrinos travel through matter, the possibility of the neutrinos interacting coherently (i.e. in such a way as to have the same particles before and after the interaction) with that

matter adds a term to the Hamiltonian called the matter potential. This phenomenon was first pointed out by Lincoln Wolfenstein [16] and further developed for neutrinos moving through matter of varying density (e.g. the Sun) by Stanislas Mikheyev and Alexei Smirnov [17], and it is called the MSW effect. All three flavors of neutrinos in the SM can coherently interact with ordinary matter via NC interactions, but only electron (anti)neutrinos can coherently interact with ordinary matter via CC interactions. So, in the flavor basis, the matter potential (for ordinary matter) is

$$V_{\text{matter}} = \begin{bmatrix} V_{CC} + V_{NC} & 0 & 0 \\ 0 & V_{NC} & 0 \\ 0 & 0 & V_{NC} \end{bmatrix}, \tag{1.15}$$

where $V_{CC} = \sqrt{2} G_F N_e$ and $V_{NC}$ are the interaction potentials, $G_F = 1.166 \times 10^{-23}\,\text{eV}^{-2} = 8.96 \times 10^{-38}\,\text{eV}\,\text{cm}^3$ is the Fermi constant, and $N_e$ is the number density of electrons in the matter being traveled through. Thus, the Hamiltonian for neutrinos traveling through ordinary matter in the mass basis is

$$H_{\text{mat}} = \frac{1}{2E} \begin{bmatrix} 0 & 0 & 0 \\ 0 & \Delta m^2_{21} & 0 \\ 0 & 0 & \Delta m^2_{31} \end{bmatrix} + \sqrt{2} G_F N_e U^\dagger \begin{bmatrix} 1 & 0 & 0 \\ 0 & 0 & 0 \\ 0 & 0 & 0 \end{bmatrix} U + \left( \frac{m_1^2}{2E} + V_{NC} \right) I_3 \,. \tag{1.16}$$

Note that the neutrino mass eigenstates, which we found in the vacuum case, are not eigenstates of this modified Hamiltonian. Solving for neutrino propagation and oscillation in matter requires diagonalizing this Hamiltonian. An example of calculating the oscillation probability in matter using perturbation theory can be found in Appendix A.

### 1.2.4 Oscillation Experiments

To test the existence of neutrino oscillation, one needs 1) a neutrino source for which the produced flux of neutrinos is well known, and 2) a neutrino detector that can either distinguish between neutrino flavors, or detect one particular flavor of neutrino. The distance separating the source and the detector, called the "baseline" of the experiment, must be chosen judiciously to optimize the detection of neutrino oscillation. The neutrinos of flavor $\alpha$ being produced from the source, traveling to the detector, and interacting with the detector as a neutrino of flavor $\beta$ via an interaction of type $I$ comprise a "channel" in the experiment. Generally, we label the channel as a $\beta$ neutrino appearance channel if $\alpha \neq \beta$ and as a $\beta$ neutrino disappearance channel if $\alpha = \beta$. Then, the number of neutrinos detected in channel $c$ ($\alpha \to \beta$, $I$) with a "reconstructed" energy $E$ in energy bin $i$ (i.e. $E_i < E < E_{i+1}$) is related to the oscillation probability $P_{\alpha\to\beta}$ by

$$N_i^c = \int_{E_i}^{E_{i+1}} \mathrm{d}E \int_0^\infty \mathrm{d}E_\nu \, f\Phi_\alpha(E_\nu) P_{\alpha\to\beta}(E_\nu)\sigma_\beta^I(E_\nu) R_\beta^I(E_\nu, E)\epsilon_\beta^I(E)\,, \tag{1.17}$$

where $E_\nu$ is the true energy of the incoming neutrino, $\Phi_\alpha(E_\nu)\,\mathrm{d}E_\nu$ is the flux of neutrinos of flavor $\alpha$ having an energy between $E_\nu$ and $E_\nu + \mathrm{d}E_\nu$ that are produced by the source, $f$ is the fraction of the neutrinos produced by the source that are directed toward the detector, $\sigma_\beta^I(E_\nu)$ is the cross section of the interaction (of type $I$) of a neutrino of flavor $\beta$ (with energy $E_\nu$) with the material in the detector, $R_\beta^I(E_\nu, E)\,\mathrm{d}E$ is the probability that a neutrino of flavor $\beta$ (with energy $E_\nu$) that is detected (via an interaction of type $I$) is reconstructed as having an energy between $E$ and $E + \mathrm{d}E$, and $\epsilon_\beta^I(E)$ represents the efficiency with which a neutrino reconstructed as having energy $E$ is counted after thresholds and cuts are applied [18]. We can find $R_\beta^I$ (also called the energy response) and $\epsilon_\beta^I$ (also called the post-smearing efficiencies) from the energy distribution $D_\beta^I(E_\nu, E')$ of the secondary particle (i.e. the particle produced

by a neutrino of flavor $\beta$ and with energy $E_\nu$ interacting with the detector via interaction type $I$, where $E'$ is the particle's energy), the detector's threshold function $T_\beta(E')$ (which is determined by the detector's resolution and analysis cuts), and the energy resolution $V_\beta(E', E)$ for the secondary particle (i.e. the probability that a secondary particle of energy $E'$ will lead to a reconstructed neutrino energy $E$) by using

$$R^I_\beta(E_\nu, E)\epsilon^I_\beta(E) = \int_0^\infty \mathrm{d}E'\, T_\beta(E') D^I_\beta(E_\nu, E') V_\beta(E', E)\,. \tag{1.18}$$

After observing hints of a deficit in the predicted amount of neutrinos coming from the Sun in 1968 [19], and again from the atmosphere in 1986 [20, 21], the search began in earnest to discover neutrino oscillations. The Super Kamioka Nucleon Decay Experiment (Super-KamiokaNDE or SK) collaboration observed significant neutrino oscillations by atmospheric neutrinos using a water Cherenkov detector [22]. Then, the Sudbury Neutrino Observatory (SNO) collaboration used a heavy water Cherenkov detector to observe the neutrinos coming from the Sun using both NC and CC interactions, so they could compare the number of electron neutrinos observed in CC interactions to the total number of neutrinos observed in NC interactions, and found that the number of NC interactions was consistent with the predictions of the solar neutrino spectrum and that the number of CC interactions was consistent with the electron antineutrinos oscillating via the MSW effect [23].

Once the existence of neutrino oscillations was established, experiments turned their focus to measuring the neutrino oscillation parameters.

### Artificial Sources

To do precision neutrino oscillation measurements, it is helpful to use artificial sources in order to reduce the flux uncertainty, since we have more control over the conditions in which

the neutrinos are produced than for natural sources (like the Sun, atmosphere, etc).

The first artificial source used for neutrino experiments was a nuclear reactor [6]. In nuclear reactors, electron antineutrinos are produced via beta decay of some of the daughter products of the fission reaction. As there are many different possible daughter products and ways that those products could decay, there are thousands of parameters that would need to be measured extremely precisely in order to obtain a meaningful result from summing the neutrino energy spectra from each possible decay. So, calculations of the expected reactor neutrino energy spectrum have been performed using the measured electron energy spectra for each parent isotope used in nuclear reactors ($^{235}$U, $^{238}$U, $^{239}$Pu, $^{241}$Pu) [1, 2]. Reactor experiments are limited to studying antineutrinos at short-medium baseline, since the neutrinos spread out evenly in all directions, so the intensity drops off as the inverse of the baseline squared.

On the other hand, particle accelerators can be used to make a beam of pions ($\pi^+$ or $\pi^-$), which decay into muons and muon (anti)neutrinos. See Appendix B for a calculation of the energy spectrum of muon neutrinos produced by a pion beam. Since the pion beam is focused with a high momentum, the intensity of (anti)neutrinos does not drop off much with distance, so very-long-baseline experiments are possible with accelerator neutrinos. Also, the focusing mechanism used can select either $\pi^+$ or $\pi^-$, so accelerator experiments can study both neutrinos and antineutrinos.

### Experimental Systematic Uncertainties

In any experiment, parameters (called nuisance parameters) are introduced into the model to encode our uncertainties in various inputs into the model. Commonly, in neutrino oscillation experiments, an overall normalization factor is used for the uncertainty in the total rate of neutrinos being produced at the source, and a normalization factor per detector is

used for uncertainties in the detectors' masses. Another normalization factor (or a set of normalization factors, if there are uncertainties for how it varies with energy) can be used for each channel to encode uncertainties in the interaction cross section.

A "pull" term for each nuisance parameter is included in the $\chi^2$ function in order to inflict a penalty on the goodness of fit if the nuisance parameter strays too far from its expected value. The pull term is generally of the form

$$\frac{(p - \langle p \rangle)^2}{\sigma_p^2},$$

where $p$ is the value of the nuisance parameter, $\langle p \rangle$ is the expected value of $p$, and $\sigma_p$ is the standard deviation (i.e. uncertainty) of $p$. In the case of nuisance parameters being correlated with each other, the pull terms for these nuisance parameters can be expressed by the equation below, instead of the previous equation:

$$\sum_{i,j} (p_i - \langle p_i \rangle)\left(V^{-1}\right)_{ij}(p_j - \langle p_j \rangle),$$

where $p_i$ are the correlated nuisance parameters and $V_{ij} \equiv \langle (p_i - \langle p_i \rangle)(p_j - \langle p_j \rangle) \rangle$ is the covariance matrix.

Minimizing the $\chi^2$ with respect to all the nuisance (and oscillation) parameters is what we use to determine the values of these parameters for the best fit of the data to the model. The need for being very meticulous with identifying and parameterizing our experimental uncertainties becomes more apparent when we find disagreements between experiments and theoretical predictions.

### Anomalies

Anomalies (i.e. significant inconsistencies between theory and experiment), have continually been problematic for neutrino physics, but there are three highly significant ones that remain unresolved: the LSND/MiniBooNE Anomaly, the Reactor Antineutrino Anomaly, and the Gallium Anomaly.

The Liquid Scintillator Neutrino Detector (LSND) was an accelerator neutrino experiment that ran from 1993 to 1998, measuring electron antineutrino CC interactions with a liquid scintillator detector from a beam of muon antineutrinos produced at Los Alamos National Laboratory from decay at rest $\mu^+$ [24]. Using the approximation of two-flavor neutrino oscillation, the data LSND collected preferred a mass-squared difference of $\sim 1\,\mathrm{eV}^2$, which is in disagreement with the mass-squared differences measured by solar and atmospheric neutrinos, so a fourth neutrino would be needed to explain this data as analyzed by the LSND collaboration. The Mini Booster Neutrino Experiment (MiniBooNE) was created to test the LSND anomaly [25]. They used a muon (anti)neutrino beam at the Fermi National Accelerator Laboratory and measured both electron and muon (anti)neutrinos with a liquid scintillator detector. Their measurement of electron and muon neutrinos was inconsistent with adding a fourth neutrino to the SM (though they observed an excess of electron neutrinos at low energies), but their measurement of electron antineutrinos is consistent with what LSND observed [26]. This has become known as the LSND/MiniBooNE Anomaly.

Spurred on by the upcoming Double Chooz Reactor Experiment, the expected flux of electron antineutrinos produced by reactors was recalculated in 2010 in order to make the prediction more precise, resulting in the flux predictions commonly known as the Huber-Mueller model [1, 2]. When comparing all the data from reactor neutrino experiments to these new predictions, a significant deficit of electron antineutrinos was observed across all reactor exper-

iments. Daya Bay measured this spectrum with unprecedented precision and also observed this overall deficit, along with a significant "bump" in the spectrum at around 5 MeV [27]. These two effects, the deficit and the bump, are seen at the majority of reactor neutrino experiments and have become known as the Reactor Antineutrino Anomaly [28].

### Beyond the Standard Model Effects

When the SM was originally put together, it was thought that neutrinos were massless, so no mass terms for neutrinos exist in the official SM Lagrangian. There are two different types of mass terms that can be added to the SM in order to incorporate neutrino masses: Dirac and Majorana. For Majorana neutrinos, the antineutrino is simply a neutrino whose chirality is right-handed. For Dirac neutrinos, the antineutrino is a distinct type of particle, as with the other fermions. So far, no experiments have been able to distinguish between the two mass terms.

There are many scenarios not included in the SM, also known as Beyond the Standard Model (BSM) scenarios, that would affect neutrino oscillation experiments. One example is a scenario that would solve the LSND Anomaly, assuming it was consistent with other experiments: sterile neutrinos [29]. As mentioned earlier, we know that there are only three flavors of neutrinos that can interact with the $Z^0$ boson (i.e. that are active) that are lighter than the $Z^0$ boson, so if there's another light neutrino, as LSND proposed, then it must be "sterile" (i.e. cannot participate in weak interactions). The only way a sterile neutrino would affect neutrino oscillation experiments using SM neutrinos is if it mixed with the SM neutrinos, which would appear as a non-unitary neutrino mixing matrix for the SM neutrinos.

Another possible BSM scenario is neutrino Non-Standard Interactions (NSIs), in which neutrinos participate in other types of interactions (besides weak interactions) with SM particles.

This will be discussed more in Chapter 5.

# Chapter 2

# Spectral Uncertainties for Reactor Experiments

## 2.1 Preface

The reactor antineutrino anomaly, described in Section 1.2.4, alerts us to the fact that we do not really know the spectrum of neutrinos coming from the nuclear reactors. The Daya Bay collaboration has measured the spectrum with a detector that has an energy resolution of $8\%/\sqrt{E}$, but the fine structure of the spectrum remains undetermined. To account for this spectral uncertainty, the simulated event rate in each energy bin can be multiplied by a constant that is the same for all detectors but allowed to be different for each energy bin, as described in Section 2.2.3. Allowing these "nuisance parameters" to vary freely corresponds with no prior knowledge of the antineutrino spectrum produced by the source; instead, the parameters are effectively constrained by the spectrum measured by the near detector, which tells us what the spectrum should be at the far detector.

In this chapter, we look at the effects this spectral uncertainty has on the Jiangmen Underground Neutrino Observatory (JUNO) experiment. As the $\chi^2$ minimizer had trouble handling so many free parameters, we had to come up with our own way of calculating what values these parameters needed to have in order to minimize the $\chi^2$, which is discussed in Appendix C.

### 2.1.1 Attributions

Section 2.2 is a reproduction, with slight modifications, of a paper to which I contributed:

David V. Forero, Rebekah Hawkins, and Patrick Huber. *Benefits of a near detector for JUNO*. arXiv:1710.07378.

Patrick Huber made the synthetic antineutrino spectra that we used, created Fig. 2.1, and provided me with code that would retrieve the smearing matrix created by GLoBES for the simulation and that would substitute the true values from one simulated experiment for that of a different simulated experiment. David Forero wrote the code allowing the energy scaling uncertainty to be nonlinear. I wrote the rest of the code needed (including the code discussed in Appendix C), put all the pieces provided to me together, and created Fig. 2.2.

## 2.2 Benefits of a Near Detector for JUNO

### 2.2.1 Abstract

It has been proposed to determine the mass hierarchy of neutrinos by exploiting the beat between the oscillation frequencies corresponding to the two neutrino mass squared differences. JUNO is based on this concept and uses a large liquid scintillator detector at a distance of

53 km from a powerful nuclear reactor complex. We argue that the micro-structure present in antineutrino fluxes from nuclear reactors makes it essential to experimentally determine a reference spectrum with an energy resolution very similar to the one of JUNO.

### 2.2.2 Introduction

The Jiangmen Underground Neutrino Observatory (JUNO) comprises a 20 kt liquid scintillator detector with a broad physics program [30]. One of the key physics goals of JUNO is the determination of the so-called mass hierarchy of neutrinos, that is, whether the third mass eigenstate is the lightest (inverted hierarchy, IH) or heaviest (normal hierarchy, NH) without having to rely on matter effects: with an appropriate choice of experimental parameters, it is possible to *simultaneously* be sensitive to oscillations corresponding to the two mass squared differences $\Delta m^2_{31} \simeq 2.5 \times 10^{-3}\,\mathrm{eV}^2$ and $\Delta m^2_{21} \simeq 7.4 \times 10^{-5}\,\mathrm{eV}^2$ [31]. In this case, also, the beat frequency between the two oscillations will be present, and whether this beat frequency is larger or smaller than the main oscillation driven by $\Delta m^2_{31}$ is a direct measure of the mass hierarchy [32]; the amplitude of the beat is given by $\sin^2 2\theta_{13}$. The relative difference between the beat frequency and main oscillation is of the order $\Delta m^2_{21}/\Delta m^2_{31} \simeq 1/30$, and thus an energy resolution of approximately 3% is required.

JUNO will detect reactor antineutrinos via inverse beta decay (IBD) and is situated 53 km from both the Yangjiang and Taishan nuclear power plants, the distance being carefully chosen to fulfill above conditions and to optimize the mass hierarchy sensitivity. Neutrino energy reconstruction in IBD, $\bar{\nu}_e + p \rightarrow n + e^+$, is relatively straightforward; the visible energy of the positron, $E_{e^+}$, is related to the neutrino energy $E_\nu$ via

$$E_\nu = E_{e^+} + (m_n - m_p - m_e)\,, \tag{2.1}$$

neglecting the kinetic energy of the outgoing neutron, which, for the neutrino energies in question, is an excellent approximation. The energy deposited by the positron in the scintillator is converted to light, and the energy resolution is determined by photon counting statistics and, to first order, scales as $1/\sqrt{E_{e^+}}$.

Attaining the requisite 3% energy resolution is a challenge in itself, but, given the relatively small size of the effect, the question of systematic uncertainties needs to be addressed. There are three main types of systematics for this measurement: uncertainty in $\Delta m^2_{31}$, *i.e.* uncertainty about the main oscillation frequency; uncertainty in the detector energy response, *e.g.* a shift of the energy scale has the same effect as a change in $\Delta m^2_{31}$; and reactor antineutrino flux uncertainties, since one is searching for a high-frequency component in the Fourier spectrum, and any high-frequency components in the flux can lead to confusion. All of these have been discussed in various combinations in the literature, and, in particular, the JUNO collaboration is clearly aware of them [30].

The goal of this letter is to highlight the impact of one source of uncertainty which is recognized but may have been underestimated: the reactor antineutrino flux. For all the systematic effects except the $\Delta m^2_{31}$ uncertainty, some type of parameterization or implementation in the analysis has to be found. We argue, here, that the parameterizations used previously to account for the reactor flux uncertainties are not capturing the relevant degrees of uncertainty; in other words, some of the known unknowns are not accounted for. Using a more physical model for the reactor flux uncertainties results in a large reduction of sensitivity to the mass hierarchy. This problem can be completely resolved by using a reference reactor antineutrino spectrum measured with *a similar energy resolution* as the JUNO detector. We demonstrate this by including a near detector in the simulation.

### 2.2.3 Methods

Reactor antineutrino fluxes have taken center stage as a research subject of their own since a series of papers [1, 2] in 2011 (Huber+Mueller model), which led to a revision of the flux models, giving rise to the reactor antineutrino anomaly (RAA) [28]. Antineutrinos from reactors are not made directly in the fission process; instead, they arise from the beta decays of neutron-rich fission products. There are roughly $10^3$ isotopes with about $10^4$ individual beta decay branches which would have to be known with good accuracy to compute the antineutrino flux with percent level errors. This knowledge does not exist, and thus measurements of the total beta decay spectrum from fission fragments [33–35] are used as a basis for unfolding the antineutrino spectrum. The 2011 papers have triggered significant follow-up work, and this led to the understanding that first forbidden non-unique beta decays, which make up anywhere between 20-30% of all antineutrinos relevant for IBD, and their higher-order corrections, like weak magnetism, are dominating the error budget and likely exceed the estimates [1, 2], a point driven home by the observation of a 5 MeV bump in the measured antineutrino spectrum relative to predictions, see for instance the Daya Bay result [36]; for recent reviews on this topic, see Refs. [37, 38].

As explained, a direct calculation of antineutrino fluxes is not feasible; nonetheless, these direct or *a priori* calculations allow some significant insight into the energy structure of the antineutrino spectrum without being obstructed by real-world detector effects, see for instance Ref. [39]. In Fig. 3 of Ref. [40], it is highlighted that there is significant micro-structure in the antineutrino spectrum at the 50–100 keV scale. This sawtooth shape arises because, in a single beta decay, there is a finite probability to emit an antineutrino with an energy corresponding to the entire available $Q^2$ of the transition due to the Coulomb correction experienced by the outgoing electron. Adding a large number of these, then, results in the sawtooth pattern also visible in Fig. 2.1. In Ref. [40], it is also shown that,

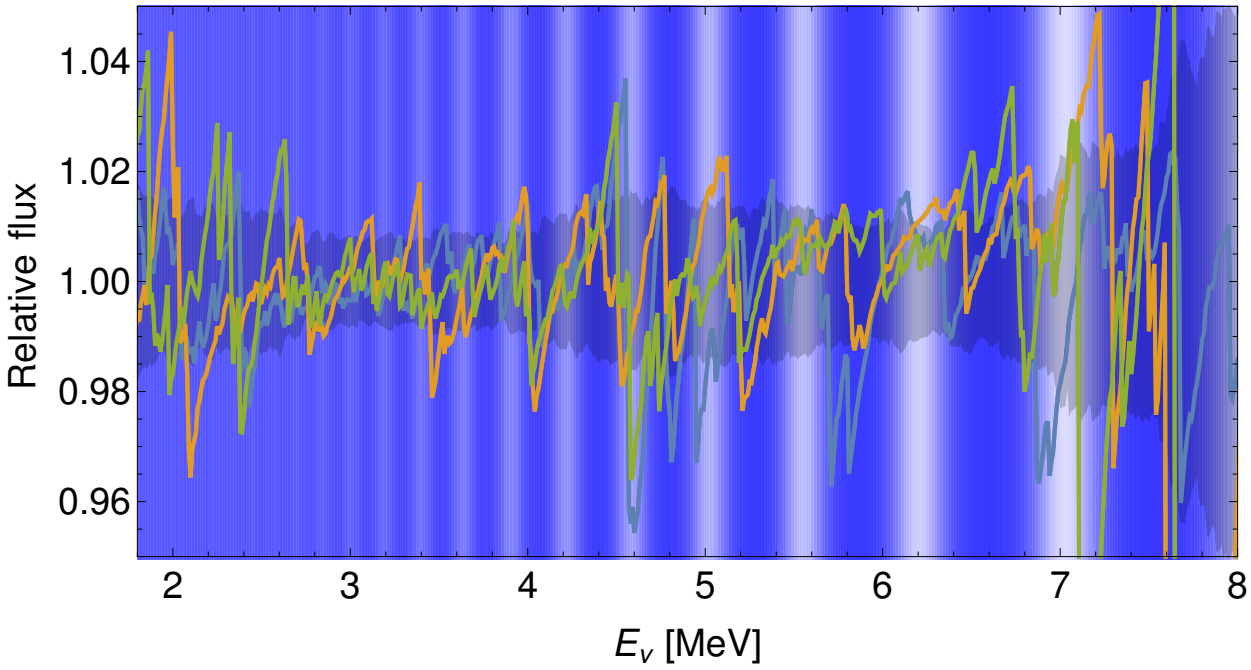


Figure 2.1: Three synthetic antineutrino spectra relative to the antineutrino spectrum predicted from the ILL data [1, 2] (Huber+Mueller model) normalized to the same total IBD event rate. The gray shaded horizontal band shows the standard deviation of the whole population of synthetic spectra. For illustration, the vertical bands indicate the oscillation arising from $\Delta m^2_{31}$ at a distance $L = 53\,\text{km}$ smeared with an energy resolution of $3\%/\sqrt{E}$.

once this sawtooth spectrum is convoluted with a detector energy resolution typical for current reactor neutrino experiments, an entirely smooth spectrum results.

*A priori* calculations account for about 80-90% of all beta decays and, thus, reproduce the total beta spectrum as measured by the ILL experiments to about the same degree [39]. Therefore, there is no reason to expect that the specific energy micro-structure derived from any of these calculations is the actual one: the specific location and size of each sawtooth is likely wrong; the distribution of locations and sizes, on the other hand, will be close to the true one. For the following, we use a model based on thermal neutron fission yields of $^{235}$U, $^{239}$Pu, and $^{241}$Pu from the JEFF database, version 3.1.1 [41], and the fast neutron fission yield of $^{238}$U from ENDF-349 [42]. We use the beta decay information contained in the Evaluated Nuclear Structure Data File (ENSDF) database, version VI [43], and the neutrino spectrum

is computed following the prescription in Ref. [2]. We use this information on fission yields and beta decays to construct a probability density function $p(Q, a)$ for the $Q$-value and amplitude $a$ for each beta decay branch. We then draw at random pairs of values for $Q, a$ and compute the resulting antineutrino spectrum; we stop adding more pairs as soon as we have the same number of antineutrinos above IBD threshold as in the Huber+Mueller model. The resulting antineutrino spectrum is then normalized to the same IBD rate as obtained from the Huber+Mueller model and reweighted to represent the shape of the Huber+Mueller flux at an energy resolution of $8\%/\sqrt{E}$. We repeat the procedure 1000 times to obtain a population of synthetic antineutrino spectra which all correspond to a very similar spectrum at $8\%/\sqrt{E}$ resolution. The results are shown in Fig. 2.1, where we show the resulting distribution for each energy bin relative to its mean (the Huber+Mueller prediction), and we also show three examples of a synthetic spectrum. For comparison, the relevant oscillation is overlayed; it is apparent that much of the structure in the synthetic spectrum is at a similar frequency and amplitude as the effect sought after in JUNO. This indicates that the strategy outlined in Ref. [30] to deal with the reactor flux uncertainty, namely to use the Daya Bay measured spectrum as reference spectrum is fraught with difficulty: the Daya Bay spectrum has been measured with an energy resolution of approximately $8\%/\sqrt{E}$ whereas for JUNO the spectrum at $3\%/\sqrt{E}$ is needed.

The question now is: what energy resolution does the reference spectrum need to be measured with, and what other detector effects could intervene? The effect of having a second detector (near detector) in the hierarchy determination has been discussed in more general terms in Refs. [44–46]. Specifically, we investigate the non-linearity of the energy response as a potential issue in comparing the data from two detectors. The Daya Bay detectors are precision instruments, and their success has inspired the design for JUNO, therefore it makes sense to use them as a proxy for the energy response. For the Daya Bay detectors, the energy

response to positrons is non-linear with the main effect happening below the 4 MeV. This effect is attributed to ionization quenching of scintillation light and Cerenkov light production and peculiarities of the electronics [47].

To include non-linear effects in the reconstruction of the positron energy one can parameterize the effect as a linear combination of functions that are powers of energy, generalizing the linear scaling [45, 48]:

$$\frac{E_{\rm rec}}{E} = 1 + \sum_{k=0}^{n} \alpha_k E^k \equiv 1 + \delta_{\rm scal}(E). \tag{2.2}$$

For $k = 0$, and with only $\alpha_0 \neq 0$, one obtains the linear case (linear scaling). Therefore, to include non-linear effects, $\alpha_k \neq 0$, one needs to include higher energy powers in Eq. (2.2). Even though this approach is conceptually simple, it does offer neither a physical condition when to stop the series nor allows to set the size and to understand the physical meaning of the non-linear coefficients.

Assuming the energy response of the JUNO detector will be similar to the one of Daya Bay Ref. [49], it is possible to estimate the remaining error $S_{\rm scal}(E)$ after the non-linear correction has been applied as a relative deviation from the nominal model. This procedure was implemented in Ref. [45, 48], where the error envelope $S_{\rm scal}(E)$ is taken from the reported detector energy response function in Ref. [49]. The largest energy scale error is around 2% in the low energy region; for most of the energy range the error is below 1%; we follow the procedure outlined in Ref. [45].

To include the effect of the remaining error after the non-linear detector energy response correction in the analysis, we have generalized the algorithm used to account for the linear scaling in GLoBES [50]. Notice that in principle the individual $\alpha_k$ coefficients can be arbitrarily large, except for $|\alpha_0| \lesssim 2\%$, since they have no direct physical meaning, and, at any energy, only the sum of all terms is constrained by the Daya Bay model. This is clearly

a shortcoming of the parameterization given in Eq. (2.2). The overall Daya Bay constraint is implemented as a penalty on the $\chi^2$-function [45]:

$$\chi^2_{\text{scal}} = \max_E \left| \frac{\delta_{\text{scal}}(E)}{S_{\text{scal}}(E)} \right|^2 . \tag{2.3}$$

After implementing the penalty in Eq. (2.3) in the JUNO simulation, we find that the $\chi^2$-function becomes somewhat wider as a function of $\Delta m^2_{31}$, indicating as mentioned previously, the similarity between a linear energy scale uncertainty and a less precise input on $\Delta m^2_{31}$. We also find that the result practically does not change for $k = 2$, and thus there is no reason to go beyond $k = 2$. For $k = 2$ the sensitivity to the mass hierarchy is decreased by $\sim 1.23\ \Delta\chi^2$ units, taking the case of the linear scaling as reference ($\Delta\chi^2_{\text{min}} \simeq 23$), which is compatible with the result in Ref. [45]. Also, a pull on $\Delta m^2_{31}$ has to be included [48], since its effect (within the current errors) can mimic the non-linear effects we are introducing, as was pointed out previously [44, 51].

Now, we can address how well a reference spectrum needs to be measured in terms of energy resolution. To this end, we set up a model with a 5 ton near detector at a distance of 0.5 km, which yields approximately $1.6 \times 10^5$ events per year. For the far detector, we assume 20 kt fiducial mass at a distance of 53 km. For both detectors, we use the non-linearity model described above with $k = 2$, and the $\alpha_k$ are varied independently for near and far detectors, reflecting the assumption that the $\alpha$'s are constrained by the calibration systems of each detector independently. We use 100 bins to compute the spectrum prior to applying the energy resolution function, and for each bin, we introduce a nuisance parameter, which is fully correlated between near and far detectors, but otherwise unconstrained. This corresponds to a flux model where no prior knowledge on fluxes is assumed except that the energy scale of variations can be as small as about 50 keV. We argued in the introduction that the relevant degrees of uncertainty in the flux lie in this micro-structure, and, locally, deviations can be

quite large, see Fig. 2.1, whereas the deviation of the mean is quite small. Finally, we use $3\%/\sqrt{E}$ as energy resolution for the far detector and vary the resolution of the near detector, plotting the result.

### 2.2.4 Results

The result of using the above method is shown in Fig. 2.2. For the solid line, we use the same flux model (Huber+Mueller) to generate the data and fit it. For the dashed lines, we use a synthetic spectrum, drawn at random from the population, to generate the data and attempt to fit it with the Huber+Mueller model: the result is close to the solid line. We conclude that, without a dedicated near detector, the sensitivity while accounting for realistic flux errors decreases from $\Delta\chi^2 \simeq 22$ to $\Delta\chi^2 \simeq 4$; whereas, with a dedicated near detector, the sensitivity may improve beyond the original one, since all flux uncertainties are eliminated.

For comparison, in Fig. 2.2 we also show the $\chi^2$-values obtained by using, instead of a near detector, the measured Daya Bay antineutrino spectrum and its full covariance matrix [36]. Point A corresponds to the case where we allow one nuisance parameter for each Daya Bay energy bin of approximately 250 keV width and find indeed that the Daya Bay data would fully eliminate the effect of flux uncertainties. Point B, however, is computed with one nuisance parameter for each of 100 bins, corresponding to the case of significant micro-structure in the antineutrino flux. Clearly, in that case, the Daya Bay measurement is *insufficient* to eliminate this systematic. Note that point B lies below the black line, which is based on a idealized near detector, because of real-world detector effects that result in significant spectrum uncertainties in the Daya Bay data for very low and very high antineutrino energies.

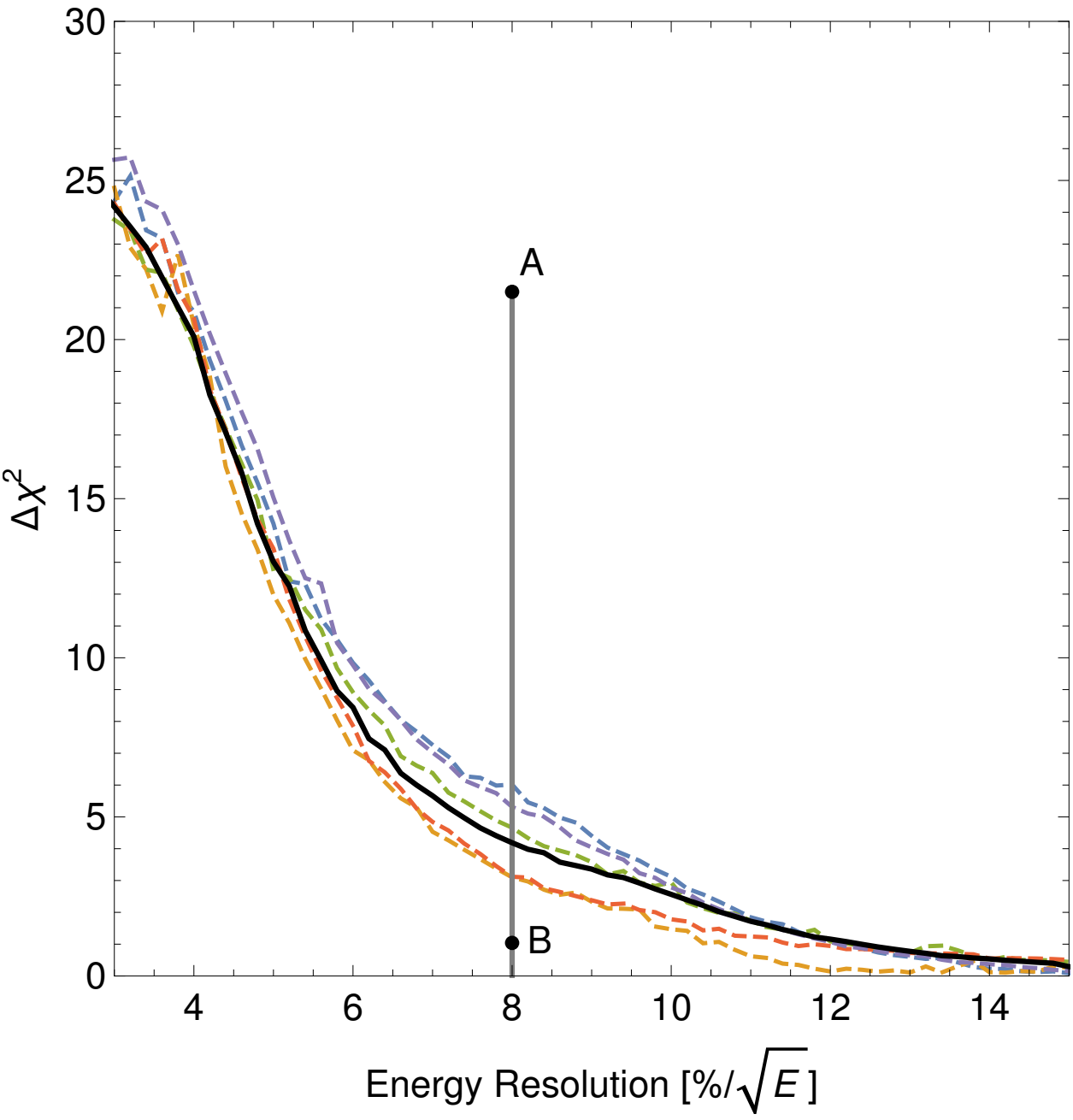


Figure 2.2: $\Delta\chi^2$ between normal and inverted hierarchy (assuming normal hierarchy to be true) for a JUNO-like experiment employing a reference measurement of the reactor spectrum as a function of the energy resolution of the reference measurement. The solid line assumes that the same spectrum is used to generate and fit the data, whereas, for the dashed lines, we use a random synthetic spectrum to generate the data and fit the data with Huber+Mueller model. The points labeled A and B, show the result obtained by using the actually measured antineutrino spectrum from Daya Bay [36]: for point A we are using one nuisance parameter per Daya Bay bin and for point B we are using one nuisance parameter in each of 100 bins.

### 2.2.5 Discussion

In summary, we made the argument that antineutrino reactor fluxes have a micro-structure at the 50 keV level which is similar to the mass hierarchy signal in experiments like JUNO. We performed a careful study of the impact of non-linearities in the energy response and find that, overall, they have a limited impact on these experiments. We show that a reference measurement of the antineutrino spectrum with an energy resolution very similar to the far detector is needed to exclude any sensitivity reduction due to the unknown micro-structure of the antineutrino flux. For simplicity, we implement a near detector, which, for a real experiment, has the added benefit of providing information on the actual running conditions of the reactor(s), and thus helps to eliminate any systematic uncertainties which otherwise could arise. However, a reference measurement performed at a different time and/or different reactor, for the purposes of this study, would be acceptable as long as the energy resolution is similar to the one of the far detector.

# Chapter 3

# Observing Quantum Interference in Neutrino Oscillations

## 3.1 Preface

As a result of the paper in Chapter 2, the JUNO collaboration decided to make a near detector at the Taishan reactor that aims to have $1.7\%/\sqrt{E}$ energy resolution [52]. The placement of the far detector where the oscillations due to both mass-squared differences can be observed, the size and phenomenal energy resolutions of the detectors, and the relatively short distance the neutrinos travel in the earth between the detectors all combine together to make JUNO the ideal experiment for studying vacuum neutrino oscillations. In this chapter, we investigate the ability of JUNO to detect an effect that arises from there being multiple independent mass-squared differences: interference between the mass-squared differences.

There are other types of experiments that are also simultaneously sensitive to both mass-squared differences, but much of those also have significant matter effects, which makes this

basic quantum mechanical effect of interference harder to isolate. I will be talking more about what these other experiments are good at observing, which JUNO cannot observe, in later chapters.

### 3.1.1 Attributions

Section 3.2 is a reproduction, with slight modifications, of a paper to which I contributed that was published in Physical Review D:

Patrick Huber, Hisakazu Minakata, and Rebekah Pestes. *Interference between the Atmospheric and Solar Oscillation Amplitudes*. Phys. Rev. D **101**, 093002 (2020). doi:10.1103/PhysRevD.101.093002. arXiv:1710.07378.

Hisakazu Minakata developed the method of determining the interference and non-interference parts of the oscillation probability, and I reproduced his results. I then modified the code we developed for the paper in Chapter 2 to use a different oscillation probability function, ran the simulation and analysis, and made both of the figures.

## 3.2 Interference between the Atmospheric and Solar Oscillation Amplitudes

### 3.2.1 Abstract

We propose to detect the interference effect between the atmospheric-scale and solar-scale waves of neutrino oscillation, one of the key consequences of the three-generation structure of leptons. In vacuum, we show that there is a natural and general way of decomposing

the oscillation amplitude into these two oscillation modes. The nature of the interference is cleanest in the $\bar{\nu}_e$ disappearance channel since it is free from the CP-phase $\delta$. We find that the upcoming JUNO experiment offers an ideal setting to observe this interference with more than $4\,\sigma$ significance, even under conservative assumptions about the systematic uncertainties. Finally, we discuss the relationship between the mass ordering resolution and the interference effect.

### 3.2.2 Introduction

It is a remarkable feature of nature that the fundamental fermions, quarks, and leptons come into our world in the form of three generations, which has various important consequences. The most dramatic one among them would be to provide a mechanism for CP violation [53]. The Standard Model of particle physics with three families of quarks, not two, allows for the existence of a phase, the Kobayashi-Maskawa (KM) phase [54], by which CP symmetry is broken; and indeed, CP violation has been observed [13, 55, 56]. If a similar phase exists in the lepton sector in the neutrino-mass-embedded Standard Model ($\nu$SM), then there will be CP violation due to the lepton KM phase.[1] The observation of the leptonic CP phase is being and will be actively pursued by the ongoing and next generation neutrino oscillation experiments [58–62].

It is a natural question whether CP violation is the only consequence of the three family structure. In the context of neutrino oscillation, the three generation structure allows for the existence of two independent mass squared differences: $\Delta m^2_{31} \equiv m^2_3 - m^2_1$ and $\Delta m^2_{21}$. Experimentally, we find the $\Delta m^2_{31}$-driven atmospheric neutrino oscillation [22] and the solar $\Delta m^2_{21}$-driven reactor neutrino oscillation [63], as well as the $\Delta m^2_{21}$-matter potential induced

[1] Note, if neutrinos are Majorana particles [57], there is an option of having CP violation with only two generations of leptons.

flavor conversion [16, 17] inside the sun [64].

Building on this success, in this paper, we wish to add a new item to the list of non-trivial consequences of the three generation structure: Quantum interference between the atmospheric-scale and solar-scale waves of neutrino oscillation. So far, the existence of the small $\Delta m^2_{21}$ effects in atmospheric and long-baseline (LBL) accelerator neutrino experiments and, similarly, the effects of the larger $\Delta m^2_{31}$, as well as the $\theta_{13}$ mixing effect, in the solar neutrino observation have been recognized as small sub-leading effects. The simultaneous full existence of both the $\Delta m^2_{31}$ and $\Delta m^2_{21}$ waves and their mutual interference, if observed, would establish another consequence of the three generation structure of neutrinos embedded into the $\nu$SM. For previous discussions which addressed related interference phenomena, see *e.g.* [65, 66] for accelerator/atmospheric neutrinos and [32, 67, 68] for reactor neutrinos.

### 3.2.3 Methods

#### The atmospheric and solar amplitudes

Our first task is to define what the atmospheric and solar amplitudes are in neutrino oscillation. In this paper, we restrict our discussion to vacuum, as a similar generic definition fulfilling the conditions 1 and 2 below is not available — in fact, very likely not existing — in matter [69].[2] The flavor basis $S$ matrix elements $S_{\alpha\beta}$ $(\alpha, \beta = e, \mu, \tau)$, which describe the neutrino flavor transformation $\nu_\beta \to \nu_\alpha$, can be written under the ultra-relativistic approximation of neutrinos as

$$S_{\alpha\beta} \;=\; U_{\alpha 1} U^*_{\beta 1} + U_{\alpha 2} U^*_{\beta 2} e^{-i\frac{\Delta m^2_{21}}{2E}x} + U_{\alpha 3} U^*_{\beta 3} e^{-i\frac{\Delta m^2_{31}}{2E}x}, \tag{3.1}$$

[2] The authors of [66] propose a particular way of decomposition into the "atmospheric" and "solar" amplitudes in matter. We will contrast their method to our own proposal in [69].

where $E$ is the energy and $\Delta m^2_{ji} \equiv m^2_j - m^2_i$ $(i, j = 1, 2, 3)$ denote the mass squared differences of neutrinos. $U_{\alpha i}$ is the element of the lepton flavor mixing matrix which relates the flavor and the mass eigenstates of neutrino as $\nu_\alpha = U_{\alpha i}\nu_i$. In Eq. (3.1), we factor out $e^{-im^2_1 x/2E}$ for simplicity of the expression, which of course does not alter the physical observables. The oscillation probability of the process $\nu_\beta \to \nu_\alpha$ is given by $P(\nu_\beta \to \nu_\alpha : x) = |S_{\alpha\beta}|^2$. Hereafter, again for simplicity of the expressions, we define

$$\Delta_{ji} \equiv \frac{\Delta m^2_{ji}}{2E}. \tag{3.2}$$

We take a heuristic way to find the appropriate definitions of the atmospheric and solar amplitudes. Let us first discuss the appearance channel, $\alpha \neq \beta$. The $S$ matrix elements in Eq. (3.1) can be rewritten as

$$S_{\alpha\beta} = U_{\alpha 3}U^*_{\beta 3}\left(e^{-i\Delta_{31}x} - 1\right) + U_{\alpha 2}U^*_{\beta 2}\left(e^{-i\Delta_{21}x} - 1\right) \tag{3.3}$$

due to unitarity, $U_{\alpha 1}U^*_{\beta 1} + U_{\alpha 2}U^*_{\beta 2} + U_{\alpha 3}U^*_{\beta 3} = 0$. Then, we claim that

$$S^{\rm atm}_{\alpha\beta} \equiv U_{\alpha 3}U^*_{\beta 3}\left(e^{-i\Delta_{31}x} - 1\right) \tag{3.4}$$

is the atmospheric amplitude, and

$$S^{\rm sol}_{\alpha\beta} \equiv U_{\alpha 2}U^*_{\beta 2}\left(e^{-i\Delta_{21}x} - 1\right) \tag{3.5}$$

is the solar amplitude. The atmospheric amplitude, by definition, describes neutrino oscillation due to non-vanishing $\Delta m^2_{31}$, and the solar amplitude describes the one caused by $\Delta m^2_{21}$. Therefore, the obtained expressions in Eqs. (3.4) and (3.5) for them are entirely natural ones.

In disappearance channels, due to a difference in unitarity, $U_{\alpha 1}U^*_{\alpha 1} + U_{\alpha 2}U^*_{\alpha 2} + U_{\alpha 3}U^*_{\alpha 3} = 1$, the $S$ matrix has a slightly different expression when it is written in terms of the atmospheric and the solar amplitudes,

$$\begin{aligned} S_{\alpha\alpha} &= 1 + |U_{\alpha 3}|^2 \left(e^{-i\Delta_{31}x} - 1\right) + |U_{\alpha 2}|^2 \left(e^{-i\Delta_{21}x} - 1\right) \\ &= 1 + S^{\rm atm}_{\alpha\alpha} + S^{\rm sol}_{\alpha\alpha} \end{aligned} \tag{3.6}$$

where $S^{\rm atm}_{\alpha\alpha}$ and $S^{\rm sol}_{\alpha\alpha}$ are defined by extending the definition in Eqs. (3.4) and (3.5), by setting $\beta = \alpha$. They, of course, satisfy the conditions $S^{\rm atm}_{\alpha\alpha} \to 0$ when $\Delta_{31} \to 0$, and $S^{\rm sol}_{\alpha\alpha} \to 0$ when $\Delta_{21} \to 0$, respectively.

Now, we try to elevate the heuristic definitions into the general definition of $S^{\rm atm}_{\alpha\beta}$ and $S^{\rm sol}_{\alpha\beta}$. For a given $S$ matrix element $S_{\alpha\beta}$, we require the following conditions to be satisfied:

1. The atmospheric and the solar amplitudes are defined, respectively, as

$$S^{\rm atm}_{\alpha\beta} = \lim_{\Delta m^2_{21}\to 0} S_{\alpha\beta}, \qquad S^{\rm sol}_{\alpha\beta} = \lim_{\Delta m^2_{31}\to 0} S_{\alpha\beta}. \tag{3.7}$$

2. We demand the completeness condition

$$S_{\alpha\beta} = \delta_{\alpha\beta} + S^{\rm atm}_{\alpha\beta} + S^{\rm sol}_{\alpha\beta}\,, \tag{3.8}$$

   where $\delta_{\alpha\beta}$ denotes the Kronecker delta function.

Consistency requires the so obtained amplitudes to satisfy

$$\lim_{\Delta m^2_{31}\to 0} S^{\rm atm}_{\alpha\beta} = \lim_{\Delta m^2_{21}\to 0} S^{\rm sol}_{\alpha\beta} = 0\,. \tag{3.9}$$

The second condition, the completeness condition, demands that decomposition of the oscillation amplitude into the atmospheric and solar amplitudes is complete. We only have three neutrino states and, therefore, two independent $\Delta m^2$: the atmospheric $\Delta m^2_{31}$ and the solar $\Delta m^2_{21}$. So, there should be two independent amplitudes, not more, not less.

### $\nu_\mu \to \nu_e$ and $\nu_e \to \nu_e$ channels

To obtain a sense of what the atmospheric and solar amplitudes are, we write down their explicit forms in the $\nu_\mu \to \nu_e$ and $\nu_e \to \nu_e$ channels by using the flavor mixing matrix using the Particle Data Group (PDG) convention [13]. We leave the discussions of the other channels to [69].

The atmospheric and solar amplitudes, as defined in Eqs. (3.4) and (3.5), respectively, can be written in the $\nu_\mu \to \nu_e$ channel as

$$\begin{aligned} S^{\text{atm}}_{e\mu} &= 2is_{23}c_{13}s_{13}e^{-i\delta}e^{-i\frac{\Delta_{31}x}{2}}\sin\frac{\Delta_{31}x}{2}\,, \\ S^{\text{sol}}_{e\mu} &= 2is_{12}c_{13}e^{-i\frac{\Delta_{21}x}{2}}\left(c_{12}c_{23}-s_{12}s_{23}s_{13}e^{-i\delta}\right)\sin\frac{\Delta_{21}x}{2}\,. \end{aligned} \tag{3.10}$$

The oscillation probability consists of two terms, each amplitude squared and summed and the interference term:

$$P(\nu_\mu \to \nu_e) = |S^{\text{atm}}_{e\mu} + S^{\text{sol}}_{e\mu}|^2 \equiv P^{\text{non-int-fer}}_{\mu e} + P^{\text{int-fer}}_{\mu e}\,, \tag{3.11}$$

where

$$\begin{aligned} P^{\text{non-int-fer}}_{\mu e} &\equiv |S^{\text{atm}}_{e\mu}|^2 + |S^{\text{sol}}_{e\mu}|^2 \\ &= s^2_{23}\sin^2 2\theta_{13}\sin^2\frac{\Delta_{31}x}{2} + \sin^2\frac{\Delta_{21}x}{2}\times\left[c^2_{23}c^2_{13}\sin^2 2\theta_{12} + s^2_{23}s^4_{12}\sin^2 2\theta_{13} - 8s^2_{12}J_r\cos\delta\right], \end{aligned}$$

and

$$P_{\mu e}^{\text{int-fer}} \equiv 2\text{Re}\left[\left(S_{e\mu}^{\text{atm}}\right)^* S_{e\mu}^{\text{sol}}\right] = 8\left[J_r \cos\left(\delta + \frac{\Delta_{32}x}{2}\right) - s_{23}^2 c_{13}^2 s_{13}^2 s_{12}^2 \cos\left(\frac{\Delta_{32}x}{2}\right)\right] \times \sin\frac{\Delta_{21}x}{2}\sin\frac{\Delta_{31}x}{2}\,. \tag{3.12}$$

We note that the interference term, Eq. (3.12), displays the key feature of the problem. That is, it consists of two terms: one that depends on $\delta$ and another that does not. Therefore, observing effect of $\delta$ is due to the quantum interference between the atmospheric and the solar amplitudes, but only a part of the total effect. A claim of observation of the quantum interference between the atmospheric and the solar amplitudes requires the observation of *both* terms in Eq. (3.12) with the *correct* magnitudes; *i.e.* a measurement of $\delta$ is *not* the same as a measurement of the interference effect.

Now, we discuss the $\nu_e \to \nu_e$ channel, which is identical to the $\bar{\nu}_e \to \bar{\nu}_e$ channel due to $CPT$-invariance. The atmospheric and solar amplitudes are written as

$$\begin{aligned} S_{ee}^{\text{atm}} &= 2s_{13}^2 e^{-i\frac{\pi}{2}} e^{-i\frac{\Delta_{31}x}{2}} \sin\frac{\Delta_{31}x}{2}\,, \\ S_{ee}^{\text{sol}} &= 2s_{12}^2 c_{13}^2 e^{-i\frac{\pi}{2}} e^{-i\frac{\Delta_{21}x}{2}} \sin\frac{\Delta_{21}x}{2}\,. \end{aligned} \tag{3.13}$$

Due to un-oscillated "1" in Eq. (3.6), the $\nu_e$ survival probability $P(\nu_e \to \nu_e)$ takes a slightly complicated form, but can be written in a similar form as in the appearance channel,

$$P(\nu_e \to \nu_e) = P_{ee}^{\text{non-int-fer}} + P_{ee}^{\text{int-fer}}\,, \tag{3.14}$$

where

$$\begin{aligned} P_{ee}^{\text{non-int-fer}} \equiv & 1 + \left|S_{ee}^{\text{atm}}\right|^2 + \left|S_{ee}^{\text{sol}}\right|^2 + 2\text{Re}\left[S_{ee}^{\text{atm}} + S_{ee}^{\text{sol}}\right] \\ = & 1 - \sin^2 2\theta_{13} \sin^2 \frac{\Delta_{31} x}{2} - 4 s_{12}^2 c_{13}^2 \left(1 - s_{12}^2 c_{13}^2\right) \sin^2 \frac{\Delta_{21} x}{2} , \end{aligned} \tag{3.15}$$

and

$$P_{ee}^{\text{int-fer}} \equiv 2\text{Re}\left[\left(S_{ee}^{\text{atm}}\right)^* S_{ee}^{\text{sol}}\right] = 2 \sin^2 2\theta_{13} s_{12}^2 \sin \frac{\Delta_{31} x}{2} \cos \frac{\Delta_{32} x}{2} \sin \frac{\Delta_{21} x}{2} . \tag{3.16}$$

**How to observe the quantum interference effect**

We briefly discuss how to pin down the quantum interference effect between the atmospheric and solar amplitudes. Once we obtain the expression of the oscillation probability as

$$P(\nu_\beta \to \nu_\alpha) = P_{\beta\alpha}^{\text{non-int-fer}} + P_{\beta\alpha}^{\text{int-fer}} , \tag{3.17}$$

we can define a "test oscillation probability" by introducing the $q$ parameter as

$$P(\nu_\beta \to \nu_\alpha) = P_{\beta\alpha}^{\text{non-int-fer}} + q P_{\beta\alpha}^{\text{int-fer}} . \tag{3.18}$$

By fitting the data with the test oscillation probability in Eq. (3.18), we would obtain 1-dimensional $\chi^2$ (1 DOF) for the $q$ parameter. We note that, in the case of appearance experiments, we marginalize over $\delta$ as well as the other mixing parameters in the experimentally allowed ranges.

Though our discussion in this paper covers both the appearance and the disappearance experiments in vacuum, the analysis of the appearance channel in accelerator LBL experiments requires treatment of the matter effect [69], which is beyond the scope of this paper.

The experimental setting of JUNO [30] is *uniquely* suited for our purpose of observing the interference effect between the atmospheric and solar oscillations. In JUNO, the solar and atmospheric oscillation effects coexist with their full magnitudes at the same detector. Both oscillations are fully developed and have left the linear regime of $\sin\frac{\Delta_{k1}x}{2}$ . Even though the atmospheric oscillation may be small wiggles over the long-wavelength solar oscillation, the very good energy resolution of the JUNO detector aims at its precision measurement. Therefore, JUNO is an ideal experiment for the purpose of detecting the atmospheric - solar interference effect. It is very likely the best choice among all possible experiments, ongoing or planned, in vacuum and in matter.

Here, we describe in detail the procedure of our statistical analysis. Using GLoBES [70, 71], we set up an experiment with two detectors: a JUNO-like far detector with a fiducial mass of 20 kt and an energy resolution of $3\%/\sqrt{E}$ at a distance of 53 km from a nuclear reactor source with a total power of 36 GWth, and a TAO-like [72] near detector with a fiducial mass of 1 ton and an energy resolution of $1.7\%/\sqrt{E}$ at a distance of 30 m from a 4.6 GWth nuclear reactor core; we assume a total data taking time of 6 years. For each detector, we use a model for non-linear effects in the reconstruction of the positron energy like that described in [73] up to cubic terms. To account for the uncertainties in the reactor antineutrino flux prediction, we conservatively introduce a nuisance parameter to each of our 100 energy bins with the spectrum computed before applying the energy resolution function. This is equivalent to the assumption of *no* prior knowledge of fluxes, as in [73]. For the purposes of producing simulated data, we assume the normal ordering to be the true mass ordering and the relevant oscillation parameters to be $\Delta m^2_{21} = 7.54 \times 10^{-5}\,\mathrm{eV}^2, \Delta m^2_{31} = 2.43 \times 10^{-3}\,\mathrm{eV}^2, \theta_{12} = 33.6^\circ,$ and $\theta_{13} = 8.9^\circ$. For the analysis of the resulting data, we fit the data obtained from the oscillation probability in Eq. (3.16) with that obtained using the oscillation probability modified with the parameter $q$, as in Eq. (3.18), by minimizing the following $\chi^2$

function for various values of $q$ while allowing all nuisance and standard oscillation parameters to vary:

$$\chi^2 = \sum_{i,I} \frac{\left(\phi^I_{\text{true},i} - \phi^I_{\text{fit},i}\right)^2}{\phi^I_{\text{true},i}} + \text{pull terms}\,, \tag{3.19}$$

where $\phi^I_{\text{true},i}$ and $\phi^I_{\text{fit},i}$ are the simulated rate and modified rate, respectively, in the $i^{\text{th}}$ energy bin for the detector specified by $I$ = Near,Far. The "pull terms," defined in Eq. (3.20), provide a penalty for $\theta_{13}$ with an uncertainty of $\sigma_{\theta_{13}} = 10\%$ and the nuisance parameters $n_k$ for which uncertainties are $\sigma_k$:

$$\text{pull terms} = \frac{\left(\theta_{13,\text{true}} - \theta_{13,\text{fit}}\right)^2}{\sigma^2_{\theta_{13}}} + \sum_k \frac{n_k^2}{\sigma_k^2}\,. \tag{3.20}$$

The nuisance parameters included in the "pull terms" encode the uncertainties for energy calibration (only linear terms), fiducial mass of each detector, and flux, as described in detail in [73].

### 3.2.4 Results

The resulting $\chi^2$ curve is shown as the thick black line in Fig. 3.1. At $q = 0$, the value of $\chi^2$ is 16.7, so the interference effect would be able to be seen in JUNO with a significance of more than $4\sigma$.

The same analysis procedure is repeated except assuming that the energy calibration error for each detector is linear (blue solid line), and then without a near detector while assuming perfect knowledge of detector and source systematics (gray dashed line).

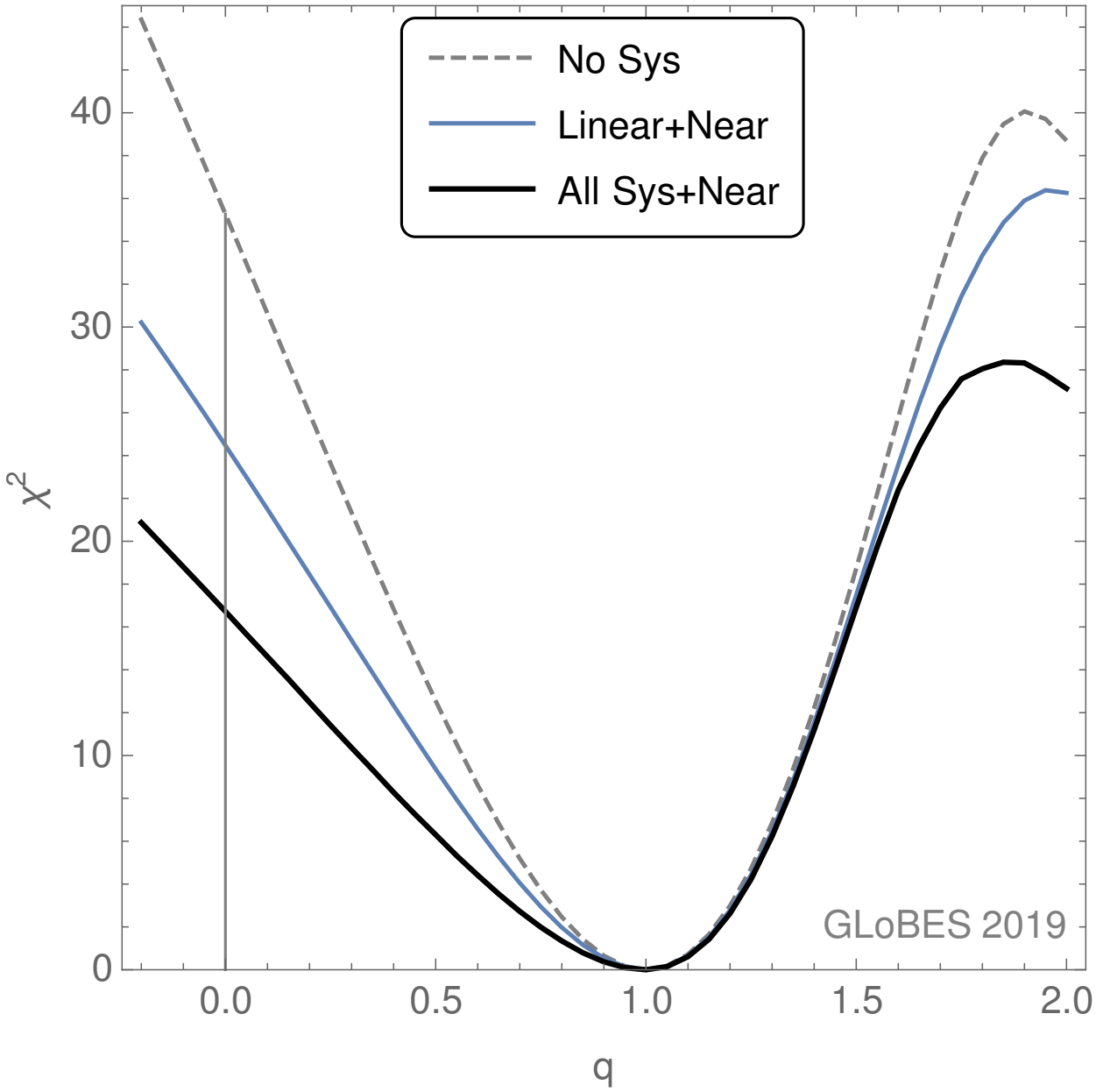


Figure 3.1: $\chi^2$ as a function of the $q$ parameter introduced in Eq. (3.18) for various systematic uncertainty and detector scenarios. The thick solid line includes all systematics with a near detector, whereas the blue line assumes the energy scale errors are linear. The gray dashed line is computed without any systematics and with the assumption of a perfect knowledge of the initial neutrino flux and no near detector.

Note that there is a potential model-dependence, in that we assume that atmospheric oscillation experiments observe $\Delta m^2_{31}$. If, instead, we assume that they measure $\Delta m^2_{32}$, the value of $\chi^2$ at $q = 0$ for the scenario with a near detector and most conservative systematics is still 16.7.

**Interference effect and Mass ordering**

It is a natural question to ask how the sensitivity to the interference effect depends on the neutrino mass ordering, and conversely, whether the capability to determine the mass ordering is due to the interference between the atmospheric and solar waves. Hereafter, we use the abbreviation "NO" and "IO" for the normal and the inverted orderings, respectively.

We start by recalling that the interference term, the second term in Eq. (3.16), must be the origin of sensitivity to the mass ordering because it is the only term which is odd under the inversion NO $\leftrightarrow$ IO. This seems to support the notion, expressed in [32, 67], that the mass ordering resolution is due to the interference between the atmospheric - solar waves. However, we will show that the reality is a little more complicated.[3]

The mass ordering dependence of $\chi^2(q)$ is examined in Fig. 3.2 using the most conservative systematics and including a near detector, as in the previous section. If we use the NO (IO) for both the true mass ordering and the test probability for fitting, the black solid (blue dotted) curve results. These two curves indicate that sensitivity to the interference does not depend on the mass ordering.

The behavior of $\chi^2(q)$ drastically changes if the JUNO data is fit with the wrong mass ordering. In Fig. 3.2, the black dotted (blue solid) curve is the case of true NO (IO) fit with the IO (NO) hypothesis. The large value of $\chi^2(q) \approx 25$ at $q = 1$ tells us that JUNO can

[3] Note also, that the interference term defined in [32, 67] is different from ours.

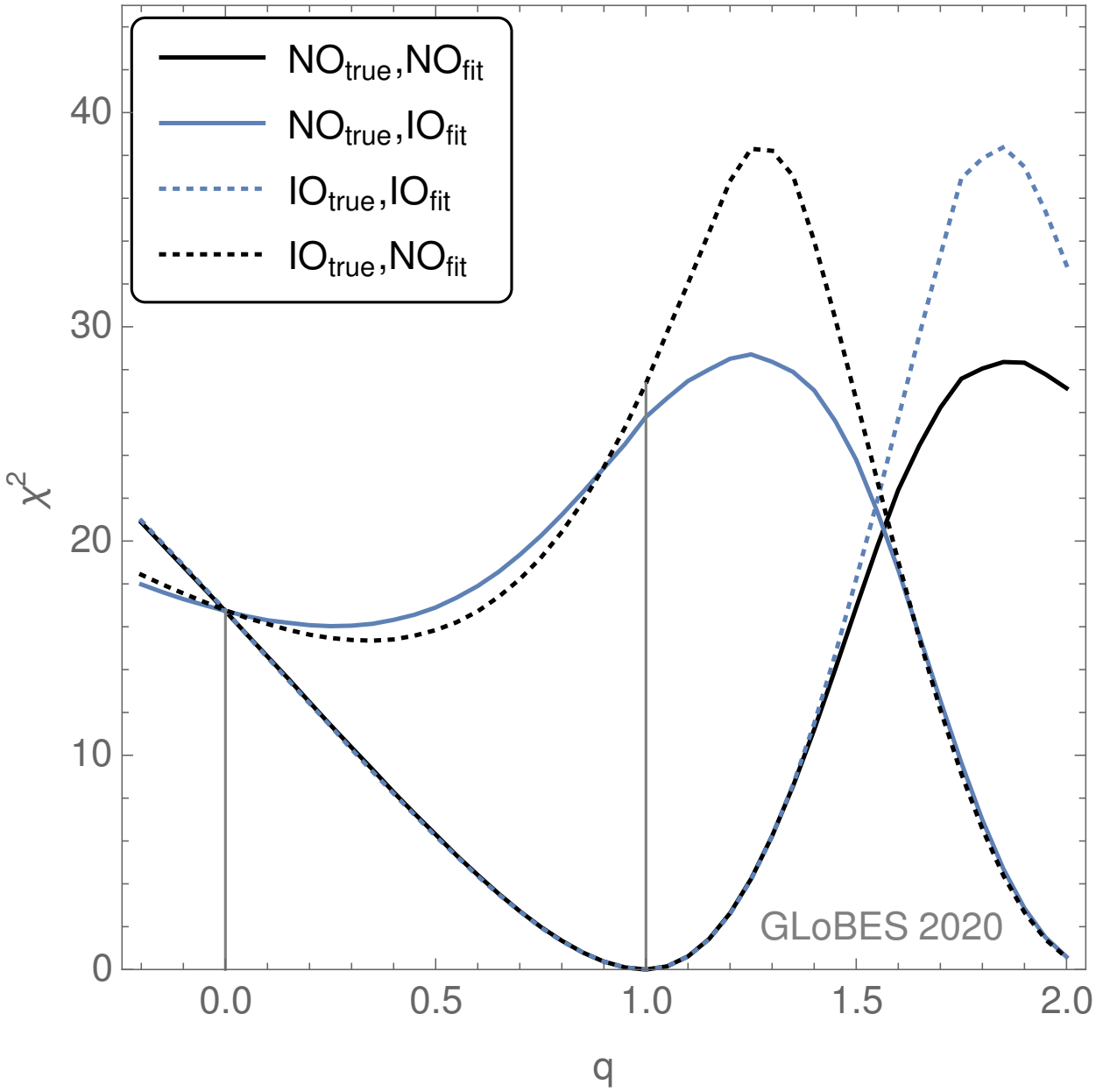


Figure 3.2: $\chi^2$ as a function of the $q$ parameter defined in Eq. (3.18) with all the systematics and with a near detector, considering various mass ordering scenarios. The solid lines are for the case that the true mass ordering is normal, which are fit with the hypotheses of the NO (black line) or IO (blue line). The dotted lines are for the case of true IO, which are fit with the NO (black line) or IO (blue line) hypotheses. The black solid curve is identical with the one in Fig. 3.1.

refute the wrong mass ordering at a confidence level around $5\sigma$ in both cases of the true mass orderings. This result is consistent with the one in [73]. The precise value depends on the details of the systematics implementation (see also [30] and the references cited therein) but is not germane.

### 3.2.5 Discussion

One might naively expect that detection of the interference term [Eq. (3.16)] would be trivial for JUNO, as it is large ($\sim \sin^2 2\theta_{13} \simeq 0.1$). However, this sensitivity is being reduced by a combination of not knowing the values of the oscillation parameters precisely enough to start with and cancellation occurring due to the energy bins. In fact, one can show analytically that an integration over a $\frac{1}{4}$ period of the atmospheric-scale oscillation of $P_{ee}^{\text{int-fer}}$ in Eq. (3.16) cancels the contribution from the adjacent $\frac{1}{4}$ period under the approximation $\sin \Delta_{21} x \sim \Delta_{21} x$. Then, it can be translated into the cancellation among different energy bins in integration over $1/E$, which leads to an imperfect but efficient cancellation in energy space. It is conceivable that such cancellation contributes substantially to the behavior of $\chi^2(q)$ in the right and wrong mass-ordering fits.

Another key feature of the question is the minimum of $\chi^2(q)$ at $q \simeq 2$ in the wrong mass-ordering fit. It is produced by allowing both $\theta_{12}$ and $\Delta m^2_{31}$ to float freely in the fit. If we instead kept all the oscillation parameters fixed, we would find that all of the curves become parabolic with their minimum at $q \simeq 1$, albeit with the wrong mass-ordering fit curves having a much larger value at the minimum. The minimum around $q = 2$ arises as a combined effect of shifting $\Delta m^2_{31}$ by about 1% from its input value and $\sin^2 \theta_{12}$ by about 3%, respectively. The occurrence of this minimum is independent of systematics and energy resolution, which

can be demonstrated by using a pseudo-$\chi^2$, $\hat{\chi}^2$, defined as

$$\hat{\chi}^2(q) = \int dE \, \left[P_{NO}(E, q = 1) - P_{IO}(E, q)\right]^2 \, . \tag{3.21}$$

Apart from an overall scale factor, $\hat{\chi}^2$ reproduces the q-dependence shown Fig. 3.2 if $\theta_{12}$ and $\Delta m^2_{31}$ are allowed to float. Moreover, we find that the value of $q$ for which the IO minimum occurs scales like $\sin^{-2}\theta_{12}$. We conclude that this second minimum is due to a complete cancellation at the probability level by accident, *i.e.* the values of oscillation parameters it occurs at do not represent an intrinsic symmetry of the oscillation probability. This rather striking behavior also demonstrates that a determination of the mass ordering, which entirely takes place at $q = 1$, is *not equivalent* to study the question of whether the q-term (*i.e.*, the interference term) is present at all.

The origin of the local deep minimum of $\chi^2(q)$ at $q \sim 2$ can also be understood by following the analysis technique outlined in [68], which is using the Fourier transform of the event spectrum or probability as a function of $L/E$.[4] In the Fourier spectrum, one observes a main peak at $\Delta m^2_{31}$ with a shoulder at $\Delta m^2_{31} \pm \Delta m^2_{21}$ and the mass hierarchy is determined by the *relative* position of shoulder and main peak. Note that the absolute positions of the peaks are only known within the uncertainty of $\Delta m^2_{31}$, which is much larger than their separation.

Varying $q$ changes the relative amplitudes of the peaks and can thus lead to a confusion of mass ordering. If we use $\hat{\chi}^2$ in Eq. (3.21) with the true NO, which has a local minimum at $q \simeq 2$, the relative positions of the higher and lower peaks exchange positions when $q$ is increased from $q = 1$ and $q \simeq 2$.

Conceptually, it is possible to imagine a world in which $\Delta m^2_{31}$ is determined with superb

[4]Note, that the Fourier approach, while conceptually very clear, is not well suited to a full study including systematic effects on the energy scale and thus, is not used for actual sensitivity estimates, see for example [30].

accuracy ($\ll \Delta m^2_{21}$). In this case, one can show numerically that the degeneracy indeed goes away, and hence, there is no confusion, since now the position of the peaks, instead of their relative heights, can be used to determine the mass hierarchy. Thus, in that case, the sensitivity to mass ordering exists in a robust way independent of the potential strength of the interference term.

To summarize, we failed to see evidence for the intimate, direct connection between sensitivity to the mass ordering and the atmospheric - solar interference effect.

**Summary**

In this paper, we have shown that, in vacuum, a natural and general way of decomposing the oscillation amplitudes into solar and atmospheric parts is possible for appearance and disappearance channels. This decomposition is exact and relying neither on the hierarchical values of the two $\Delta m^2$ nor on the actual values of observed oscillation parameters. With this amplitude decomposition, it becomes possible to define the effect of interference between the two partial amplitudes. For appearance channels, the interference term contains the $CP$-phase $\delta$, but also terms independent of it.

In the $\bar{\nu}_e$ ($\nu_e$) disappearance channel, the oscillation amplitude does *not* depend on $\delta$, and hence, the interference effect we saw has nothing to do with the $CP$-phase. The nature of the interference phenomena indicated by these features is a dynamical, quantum mechanical interference inside the three family of neutrinos, not particularly related to the $CP$-violating phase. We show, by detailed numerical calculation, that JUNO can observe this interference effect with more than $4\,\sigma$ significance.

We have also discussed the relationship between the interference effect and sensitivity to the mass ordering resolution. We argued that though the latter comes from the interference

term in Eq. (3.16), we see no supporting evidence for the hypothesis of the mass ordering resolution being equivalent to the atmospheric - solar wave interference effect.

## Acknowledgments

One of the authors (H.M.) thanks Takaaki Kajita and Hiroshi Nunokawa for intriguing conversations while this project was still in its infancy. The work of P.H. and R.P. is supported by the US Department of Energy Office of Science under award number DE-SC0020262.

Note added: After we completed this work, we have learned that the author of [74] used unitarity as in Eq. (3.4) to derive the alternative form of the oscillation probability in N flavor case which agrees with our formula for N=3. However, neither physics of atmospheric - solar interference, nor the amplitude decomposition with completeness is discussed in that paper.

# Chapter 4

# $CP$ Violation in Standard Neutrino Oscillations

## 4.1 Preface

One parameter in neutrino oscillations that JUNO is not able to measure is often referred to as the $CP$-violating phase ($\delta$), and it is the oscillation parameter in standard neutrino oscillations that we know the least about. The experiments that are most sensitive to $\delta$ are long-baseline experiments using muon (anti)neutrinos from accelerators, such as the Deep Underground Neutrino Experiment (DUNE) and Tokai to Hyper-KamiokaNDE (T2HK), to which NuMI Off-axis $\nu_e$ Appearance (NO$\nu$A) and Tokai to KamiokaNDE (T2K), discussed in Chapter 5, are predecessors. All of these experiments detect both electron and muon (anti)neutrinos via both CC and NC interactions and have methods for discriminating between events in these different channels. It is the comparison between the neutrino and antineutrino channels that give the best sensitivity to $\delta$. As we measure oscillation parameters more precisely and the focus shifts toward the parameter for which we know the least

about its value, we need to be careful to understand what we are actually measuring. Since $\delta$ arises from a scheme of parameterizing the neutrino mixing matrix, we will investigate, in this chapter, how it changes with slightly changing the parameterization scheme and what that means for interpreting data.

### 4.1.1 Attributions

Section 4.2 is a reproduction, with slight modifications, of a paper to which I contributed:

Peter B. Denton and Rebekah Pestes. *The Impact of Different Parameterizations on the Interpretation of CP Violation in Neutrino Oscillations.* arXiv:2006.09384.

A substantially expanded version of this paper was recently published as

Peter B. Denton and Rebekah Pestes. *The impact of different parameterizations on the interpretation of CP violation in neutrino oscillations.* JHEP **2021**, 139 (2021). https://doi.org/10.1007/JHEP05(2021)139.

Using the parameterization schemes Peter Denton chose, I did all the calculations needed to create the tables and figures in this paper and created all the figures. Peter Denton took my results and applied them to T2K's data.

## 4.2 The Impact of Different Parameterizations on the Interpretation of $CP$ Violation in Neutrino Oscillations

### 4.2.1 Abstract

$CP$ violation in the lepton mass matrix will be probed with good precision in upcoming experiments. The amount of $CP$ violation present in oscillations can be quantified in numerous ways and is typically parameterized by the complex phase $\delta_{\text{PDG}}$ in the standard PDG definition of the lepton mixing matrix. There are additional parameterizations of the lepton mixing matrix as well. Through various examples, we explore how, given the current data, different parameterizations can lead to different conclusions when working with parameterization dependent variables, such as $\delta$. We demonstrate how the smallness of $|U_{e3}|$ governs the scale of these results. We then demonstrate how $\delta$ can be misleading and argue that the Jarlskog is the cleanest means of presenting the amount of $CP$ violation in the lepton sector. We also confirm that, among the different parameterizations considered, the standard PDG parameterization has a number of convenient features.

### 4.2.2 Introduction

While the fact that $CP$ violation (CPV) is needed to explain the matter-antimatter asymmetry in the universe [75] is a frequently used motivation for searching for sources of CPV, identifying sources of CPV is interesting in its own right. Not only does it play an important part of the ongoing goal of measuring the parameters of the Standard Model, but also for understanding when $CP$ is and is not violated. In the quark sector, the Cabibo-Kobayashi-

Maskawa (CKM) matrix [54, 76] provides a small amount of CPV [13]. For leptons, three phases relating to how neutrinos and anti-neutrinos behave differently appear in the lepton mixing matrix $U$ [14, 15], one of which ($\delta$) is analogous to the KM phase in the CKM matrix while the other two are physical if and only if neutrinos have a Majorana contribution to their mass. $U$, like the CKM matrix for quarks, describes the mismatch of lepton flavor eigenstates ($|\nu_\alpha\rangle$ for $\alpha = e, \mu, \tau$) and mass eigenstates ($|\nu_i\rangle$ for $i = 1, 2, 3$) via $|\nu_\alpha\rangle = \sum_i U^*_{\alpha i} |\nu_i\rangle$. While all three phases contribute to leptonic CPV, the complex phase $\delta$ contributes to neutrino oscillation while the two Majorana phases, though important for neutrinoless double beta decay, do not. The complex phase $\delta$, however, is convention dependent and thus not a fundamental quantity. The most useful fundamental quantity to describe the amount of CPV in a mass matrix is the Jarlskog invariant [77]:

$$J \equiv \mathrm{Im}[U_{e1} U^*_{e2} U^*_{\mu 1} U_{\mu 2}] \,. \tag{4.1}$$

The choice of the $2 \times 2$ submatrix in Eq. (4.1) is arbitrary; we chose the (3,$\tau$) submatrix resulting from deleting the third column and the $\tau$ row in Eq. (4.1) for concreteness. Any row and any column can be removed.

There are many different ways of parameterizing the lepton mixing matrix, all of which must have at least one complex phase. Depending on the details of the parameterization, the constraint on the complex phase can be quite different. This means that interpreting results and goals of experiments in terms of the complex phase of one parameterization is not a fundamental description of our understanding of CPV.

In addition, new physics scenarios, if they exist in reality, can fundamentally complicate the extraction of $CP$ violation independent of how the mixing matrix is parameterized. For example, the addition of non-standard neutrino interactions (with or without additional $CP$-

violating phases), sterile neutrinos (also with or without additional $CP$-violating phases), or unitary violation can all lead to confusion related to the extraction of the standard $CP$-violating three-flavor phase [78–102]. Some of these degeneracies can be differentiated by combining measurements from different experiments. These scenarios are different from those discussed in this paper in that in the presence of new physics, extracting information about $CP$ violation would suffer from various partial degeneracies *independent* of the choice of parameterization. The optimal choice of parameterization of the $3 \times 3$ (or $4 \times 4$ or larger matrix in the presence of additional neutrinos) mixing matrix in the presence of various new physics scenarios is beyond the scope of this article and we will focus on the standard three-flavor oscillation picture with no new interactions.

In this paper, we will demonstrate exactly how the complex phase of the lepton mixing matrix is not the optimal parameter for understanding CPV in neutrino oscillations and when it can be misleading. We will show how different, perfectly valid, representations of the mixing matrix with one complex phase can lead to rather different conclusions when the complex phase is used as the primary indicator of CPV in oscillations. In section 4.2.3, we will define the parameterizations we are going to consider in this paper. Next, we will show how these different parameterizations affect their respective $\delta'$ and the key role that $U_{e3}$ plays in section 4.2.3. Finally, we will discuss our results in the context of T2K's measurements in section 4.2.5 and we will draw several interesting conclusions in section 4.2.5.

### 4.2.3 Methods

#### Mixing Matrix Parameterizations

We anticipate that the lepton mixing matrix, $U$, should be unitary up to any corrections from sterile neutrinos, which we ignore. Thus, the matrix can be parameterized as three rotation

matrices, containing a total of three Euler mixing angles $(\theta_{12}, \theta_{13}, \theta_{23})$ and six complex phases. However, all rows and columns can be individually rephased if neutrinos are Dirac, or if we restrict ourselves to relativistic neutrinos, as is the case for neutrino oscillations. Rephasing is the fact that any column or row can be multiplied by an arbitrary phase. While this appears to remove all six phases present in an arbitrary $3 \times 3$ unitary matrix, one of these six rephasings is dependent on the other five, which leaves one complex phase remaining for describing neutrino oscillations and is usually labeled as $\delta$. Rephasing invariance also allows us to constrain each mixing angle to a quadrant of our choice, since changing the quadrant of a mixing angle is equivalent to specific combinations of rephasing and shifting $\delta$ by a constant. We choose to constrain all of the mixing angles to the first quadrant $(\theta_{12}, \theta_{13}, \theta_{23} \in [0, 90°))$. The three rotation matrices can be in any order, and the complex phase $\delta$ can be put into any of the rotation matrices.

When we make various parameterizations of $U$ for neutrino oscillations, the magnitudes of the matrix elements remain the same, as does the Jarlskog, but the four parameters change; this is the crux of our paper. Changing the order of the rotation matrices changes the values of the mixing angles and $\delta$ (see Table 4.2), but changing which rotation $\delta$ is on does not (other than trivial redefinitions, such as $\delta \to -\delta$), so we will only consider having $\delta$ in the rotation matrix containing $\theta_{13}$. Thus, the rotation matrices are defined as follows:

$$U_1 \equiv \begin{pmatrix} 1 & 0 & 0 \\ 0 & c_{23} & s_{23} \\ 0 & -s_{23} & c_{23} \end{pmatrix}, \quad U_2 \equiv \begin{pmatrix} c_{13} & 0 & s_{13}e^{-i\delta} \\ 0 & 1 & 0 \\ -s_{13}e^{i\delta} & 0 & c_{13} \end{pmatrix}, \quad \text{and} \quad U_3 \equiv \begin{pmatrix} c_{12} & s_{12} & 0 \\ -s_{12} & c_{12} & 0 \\ 0 & 0 & 1 \end{pmatrix}, \tag{4.2}$$

where $c_{ij} \equiv \cos(\theta_{ij})$ and $s_{ij} \equiv \sin(\theta_{ij})$. In this paper, we are only considering parameterizations of the form $U_{ijk} \equiv U_i U_j U_k$ for $i, j, k = 1, 2, 3$ in which $i$, $j$, and $k$ are all different. Other parameterizations exist [103, 104] including those using the same rotation axis twice ($U_{iji}$)

[105], three of the Gell-Mann matrices parameterizing the generators of SU(3) [106–109], four complex phases [110], the exponential of a complex matrix [111], or five rotations and a complex phase [112][1]. If one wanted to include the Majorana phases in the parameterization for $U$, the symmetric parameterization [113, 114] is advantageous over the PDG method of including the Majorana phases, and it simplifies to the PDG parameterization in the context neutrino oscillations. In this article, we focus on parameterizations containing three rotations and one complex phase although we anticipate that our conclusions qualitatively apply to other scenarios as well.

The parameterization of $U$ used by the Particle Data Group (PDG) [13] without the Majorana phases is

$$U_{\rm PDG} = U_{123} = \begin{pmatrix} c_{12}c_{13} & s_{12}c_{13} & s_{13}e^{-i\delta} \\ -s_{12}c_{23} - c_{12}s_{13}s_{23}e^{i\delta} & c_{12}c_{23} - s_{12}s_{13}s_{23}e^{i\delta} & c_{13}s_{23} \\ s_{12}s_{23} - c_{12}s_{13}c_{23}e^{i\delta} & -c_{12}s_{23} - s_{12}s_{13}c_{23}e^{i\delta} & c_{13}c_{23} \end{pmatrix}, \tag{4.3}$$

and the Jarlskog in this parameterization is

$$J = c_{12}s_{12}c_{13}^2 s_{13}c_{23}s_{23}\sin(\delta_{\rm PDG})\,. \tag{4.4}$$

The mixing matrix and Jarlskog in the other five parameterizations considered are shown in Table 4.1, see also ref. [115] for a related discussion for the quark mixing matrix.

[1]The primary parameterization presented in [112] has the same complex phase as in the $U_{132}$ parameterization below.

Table 4.1: Parameterizations of the neutrino mixing matrix $U$ under consideration in this paper and their corresponding Jarlskog invariant. The primed variables ($\delta'$, $\theta'_{ij}$, $c_{ij'} \equiv \cos(\theta'_{ij})$, $s_{ij'} \equiv \sin(\theta'_{ij})$) denote parameters in the specified alternative parameterization, whereas unprimed variables ($\delta_{\rm PDG}$, $\theta_{ij}$, $c_{ij} \equiv \cos(\theta_{ij})$, $s_{ij} \equiv \sin(\theta_{ij})$) denote parameters in $U_{\rm PDG}$.

| $U_{ijk}$ | Matrix | $J$ |
|---|---|---|
| $U_{123}$ | $\begin{pmatrix} c_{12}c_{13} & s_{12}c_{13} & s_{13}e^{-i\delta} \\ -s_{12}c_{23} - c_{12}s_{13}s_{23}e^{i\delta} & c_{12}c_{23} - s_{12}s_{13}s_{23}e^{i\delta} & c_{13}s_{23} \\ s_{12}s_{23} - c_{12}s_{13}c_{23}e^{i\delta} & -c_{12}s_{23} - s_{12}s_{13}c_{23}e^{i\delta} & c_{13}c_{23} \end{pmatrix}$ | $c_{12}s_{12}c_{13}^2 s_{13}c_{23}s_{23}\sin(\delta_{\rm PDG})$ |
| $U_{132}$ | $\begin{pmatrix} c_{12'}c_{13'} & s_{12'} & c_{12'}s_{13'}e^{-i\delta'} \\ -s_{12'}c_{13'}c_{23'} - s_{13'}s_{23'}e^{i\delta'} & c_{12'}c_{23'} & c_{13'}s_{23'} - s_{12'}s_{13'}c_{23'}e^{-i\delta'} \\ s_{12'}c_{13'}s_{23'} - s_{13'}c_{23'}e^{i\delta'} & -c_{12'}s_{23'} & c_{12'}c_{23'} + s_{12'}s_{13'}s_{23'}e^{-i\delta'} \end{pmatrix}$ | $c_{12'}^2 s_{12'}c_{13'}s_{13'}c_{23'}s_{23'}\sin(\delta')$ |
| $U_{213}$ | $\begin{pmatrix} c_{12'}c_{13'} + s_{12'}s_{13'}s_{23'}e^{-i\delta'} & s_{12'}c_{13'} - c_{12'}s_{13'}s_{23'}e^{-i\delta'} & s_{13'}c_{23'}e^{-i\delta'} \\ -s_{12'}c_{23'} & c_{12'}c_{23'} & s_{23'} \\ s_{12'}c_{13'}s_{23'} - c_{12'}s_{13'}e^{i\delta'} & -c_{12'}c_{13'}s_{23'} - s_{12'}s_{13'}e^{i\delta'} & c_{13'}c_{23'} \end{pmatrix}$ | $c_{12'}s_{12'}c_{13'}s_{13'}c_{23'}^2 s_{23'}\sin(\delta')$ |
| $U_{231}$ | $\begin{pmatrix} c_{12'}c_{13'} & s_{12'}c_{13'}c_{23'} - s_{13'}s_{23'}e^{-i\delta'} & s_{12'}c_{13'}s_{23'} + s_{13'}c_{23'}e^{-i\delta'} \\ -s_{12'} & c_{12'}c_{23'} & c_{12'}s_{23'} \\ -c_{12'}s_{13'}e^{i\delta'} & -c_{13'}s_{23'} - s_{12'}s_{13'}c_{23'}e^{i\delta'} & c_{13'}c_{23'} - s_{12'}s_{13'}s_{23'}e^{i\delta'} \end{pmatrix}$ | $c_{12'}^2 s_{12'}c_{13'}s_{13'}c_{23'}s_{23'}\sin(\delta')$ |
| $U_{312}$ | $\begin{pmatrix} c_{12'}c_{13'} - s_{12'}s_{13'}s_{23'}e^{i\delta'} & s_{12'}c_{23'} & s_{12'}c_{13'}s_{23'} + c_{12'}s_{13'}e^{-i\delta'} \\ -s_{12'}c_{13'} - c_{12'}s_{13'}s_{23'}e^{i\delta'} & c_{12'}c_{23'} & c_{12'}c_{13'}s_{23'} - s_{12'}s_{13'}e^{-i\delta'} \\ -s_{13'}c_{23'}e^{i\delta'} & -s_{23'} & c_{13'}c_{23'} \end{pmatrix}$ | $c_{12'}s_{12'}c_{13'}s_{13'}c_{23'}^2 s_{23'}\sin(\delta')$ |
| $U_{321}$ | $\begin{pmatrix} c_{12'}c_{13'} & s_{12'}c_{23'} - c_{12'}s_{13'}s_{23'}e^{-i\delta'} & s_{12'}s_{23'} + c_{12'}s_{13'}c_{23'}e^{-i\delta'} \\ -s_{12'}c_{13'} & c_{12'}c_{23'} + s_{12'}s_{13'}s_{23'}e^{-i\delta'} & c_{12'}s_{23'} - s_{12'}s_{13'}c_{23'}e^{-i\delta'} \\ -s_{13'}e^{i\delta'} & -c_{13'}s_{23'} & c_{13'}c_{23'} \end{pmatrix}$ | $c_{12'}s_{12'}c_{13'}^2 s_{13'}c_{23'}s_{23'}\sin(\delta')$ |

Table 4.2: Formulas for the four parameters in a given parameterization of $U$ in terms of the absolute value of elements of $U$ and the Jarlskog invariant. Since each mixing angle is in the interval $[0, 90^\circ)$, $\cos(\theta'_{ij}) = \sqrt{1-\sin^2(\theta'_{ij})}$. The formulas for the mixing angles are derived from the magnitudes of the "simple" elements (see definition in the text) of $U$. The formulas for $\cos(\delta')$ are derived from the magnitude of a "complicated" element of $U$. The formulas for $\sin(\delta')$ were derived from the Jarlskog.

| $U_{ijk}$ | $\sin(\theta'_{12})$ | $\sin(\theta'_{13})$ | $\sin(\theta'_{23})$ | $\cos(\delta')$ | $\sin(\delta')$ |
|---|---|---|---|---|---|
| $U_{123}$ | $\frac{\lvert U_{e2}\rvert}{\sqrt{1-\lvert U_{e3}\rvert^2}}$ | $\lvert U_{e3}\rvert$ | $\frac{\lvert U_{\mu 3}\rvert}{\sqrt{1-\lvert U_{e3}\rvert^2}}$ | $\frac{\lvert U_{\mu 1}\rvert^2\left(1-\lvert U_{e3}\rvert^2\right)^2-\lvert U_{e2}\rvert^2\lvert U_{\tau 3}\rvert^2-\lvert U_{e1}\rvert^2\lvert U_{e3}\rvert^2\lvert U_{\mu 3}\rvert^2}{2\lvert U_{e1}\rvert\lvert U_{e2}\rvert\lvert U_{e3}\rvert\lvert U_{\mu 3}\rvert\lvert U_{\tau 3}\rvert}$ | $\frac{J\left(1-\lvert U_{e3}\rvert^2\right)}{\lvert U_{e1}\rvert\lvert U_{e2}\rvert\lvert U_{e3}\rvert\lvert U_{\mu 3}\rvert\lvert U_{\tau 3}\rvert}$ |
| $U_{132}$ | $\lvert U_{e2}\rvert$ | $\frac{\lvert U_{e3}\rvert}{\sqrt{1-\lvert U_{e2}\rvert^2}}$ | $\frac{\lvert U_{\tau 2}\rvert}{\sqrt{1-\lvert U_{e2}\rvert^2}}$ | $\frac{\lvert U_{\mu 1}\rvert^2\left(1-\lvert U_{e2}\rvert^2\right)^2-\lvert U_{e3}\rvert^2\lvert U_{\tau 2}\rvert^2-\lvert U_{e1}\rvert^2\lvert U_{e2}\rvert^2\lvert U_{\mu 2}\rvert^2}{2\lvert U_{e1}\rvert\lvert U_{e2}\rvert\lvert U_{e3}\rvert\lvert U_{\mu 2}\rvert\lvert U_{\tau 2}\rvert}$ | $\frac{J\left(1-\lvert U_{e2}\rvert^2\right)}{\lvert U_{e1}\rvert\lvert U_{e2}\rvert\lvert U_{e3}\rvert\lvert U_{\mu 2}\rvert\lvert U_{\tau 2}\rvert}$ |
| $U_{213}$ | $\frac{\lvert U_{\mu 1}\rvert}{\sqrt{1-\lvert U_{\mu 3}\rvert^2}}$ | $\frac{\lvert U_{e3}\rvert}{\sqrt{1-\lvert U_{\mu 3}\rvert^2}}$ | $\lvert U_{\mu 3}\rvert$ | $\frac{\lvert U_{e1}\rvert^2\left(1-\lvert U_{\mu 3}\rvert^2\right)^2-\lvert U_{\mu 2}\rvert^2\lvert U_{\tau 3}\rvert^2-\lvert U_{e3}\rvert^2\lvert U_{\mu 1}\rvert^2\lvert U_{\mu 3}\rvert^2}{2\lvert U_{e3}\rvert\lvert U_{\mu 1}\rvert\lvert U_{\mu 2}\rvert\lvert U_{\mu 3}\rvert\lvert U_{\tau 3}\rvert}$ | $\frac{J\left(1-\lvert U_{\mu 3}\rvert^2\right)}{\lvert U_{e3}\rvert\lvert U_{\mu 1}\rvert\lvert U_{\mu 2}\rvert\lvert U_{\mu 3}\rvert\lvert U_{\tau 3}\rvert}$ |
| $U_{231}$ | $\lvert U_{\mu 1}\rvert$ | $\frac{\lvert U_{\tau 1}\rvert}{\sqrt{1-\lvert U_{\mu 1}\rvert^2}}$ | $\frac{\lvert U_{\mu 3}\rvert}{\sqrt{1-\lvert U_{\mu 1}\rvert^2}}$ | $\frac{\lvert U_{e3}\rvert^2\left(1-\lvert U_{\mu 1}\rvert^2\right)^2-\lvert U_{\mu 2}\rvert^2\lvert U_{\tau 1}\rvert^2-\lvert U_{e1}\rvert^2\lvert U_{\mu 1}\rvert^2\lvert U_{\mu 3}\rvert^2}{2\lvert U_{e1}\rvert\lvert U_{\mu 1}\rvert\lvert U_{\mu 2}\rvert\lvert U_{\mu 3}\rvert\lvert U_{\tau 1}\rvert}$ | $\frac{J\left(1-\lvert U_{\mu 1}\rvert^2\right)}{\lvert U_{e1}\rvert\lvert U_{\mu 1}\rvert\lvert U_{\mu 2}\rvert\lvert U_{\mu 3}\rvert\lvert U_{\tau 1}\rvert}$ |
| $U_{312}$ | $\frac{\lvert U_{e2}\rvert}{\sqrt{1-\lvert U_{\tau 2}\rvert^2}}$ | $\frac{\lvert U_{\tau 1}\rvert}{\sqrt{1-\lvert U_{\tau 2}\rvert^2}}$ | $\lvert U_{\tau 2}\rvert$ | $\frac{\lvert U_{\mu 1}\rvert^2\left(1-\lvert U_{\tau 2}\rvert^2\right)^2-\lvert U_{e2}\rvert^2\lvert U_{\tau 3}\rvert^2-\lvert U_{\mu 2}\rvert^2\lvert U_{\tau 1}\rvert^2\lvert U_{\tau 2}\rvert^2}{2\lvert U_{e2}\rvert\lvert U_{\mu 2}\rvert\lvert U_{\tau 1}\rvert\lvert U_{\tau 2}\rvert\lvert U_{\tau 3}\rvert}$ | $\frac{J\left(1-\lvert U_{\tau 2}\rvert^2\right)}{\lvert U_{e2}\rvert\lvert U_{\mu 2}\rvert\lvert U_{\tau 1}\rvert\lvert U_{\tau 2}\rvert\lvert U_{\tau 3}\rvert}$ |
| $U_{321}$ | $\frac{\lvert U_{\mu 1}\rvert}{\sqrt{1-\lvert U_{\tau 1}\rvert^2}}$ | $\lvert U_{\tau 1}\rvert$ | $\frac{\lvert U_{\tau 2}\rvert}{\sqrt{1-\lvert U_{\tau 1}\rvert^2}}$ | $\frac{\lvert U_{e3}\rvert^2\left(1-\lvert U_{\tau 1}\rvert^2\right)^2-\lvert U_{\mu 1}\rvert^2\lvert U_{\tau 2}\rvert^2-\lvert U_{e1}\rvert^2\lvert U_{\tau 1}\rvert^2\lvert U_{\tau 3}\rvert^2}{2\lvert U_{e1}\rvert\lvert U_{\mu 1}\rvert\lvert U_{\tau 1}\rvert\lvert U_{\tau 2}\rvert\lvert U_{\tau 3}\rvert}$ | $\frac{J\left(1-\lvert U_{\tau 1}\rvert^2\right)}{\lvert U_{e1}\rvert\lvert U_{\mu 1}\rvert\lvert U_{\tau 1}\rvert\lvert U_{\tau 2}\rvert\lvert U_{\tau 3}\rvert}$ |

We note some important features of the PDG parameterization. The most important of which is the difference between "simple" elements and "complicated" elements. We define a simple element to be one that is only a product of trigonometric functions and $e^{\pm i\delta}$ terms while complicated functions can also be the sum or difference of such terms. Thus in $U_{123}$, we see that the first row and third column are composed entirely of simple elements. In general, using the definitions in Eq. (4.2), $U_{ijk}$ has simple elements along the $i^{\text{th}}$ row and the $k^{\text{th}}$ column.

In the PDG convention, the complex phase $\delta$ is set such that $\arg(U_{e3}) = -\delta$. Within the PDG convention, this phase can be shifted with no effect on any of the oscillation physics. For example, one could multiply the third column by $e^{i\delta}$ and then the second and third rows by $e^{-i\delta}$ so that the first row and third column were all real.

In the PDG parameterization, experiments have measured all of the mixing angles (though the measurements of $\theta_{23}$ are the least precise), but $\delta$ remains largely unconstrained. Plans have been made to measure $\delta$ with good precision in future experiments [116–118], and this paper aims at discussing the meaning of the precision claimed by these measurements. In the rest of this paper, the complex phase in $U_{\text{PDG}}$ will be called $\delta_{\text{PDG}}$ while the complex phase in other parameterizations will be called $\delta'$. Recently, T2K has placed some constraints on $\delta_{\text{PDG}}$ [58, 119][2]; for now, we will consider $\delta_{\text{PDG}}$ to be completely unconstrained and then, in section 4.2.5, discuss the interplay between the T2K measurements and different parameterizations of the mixing matrix.

### $\delta$ Comparison

In order to compare the values of $\delta$ between the various parameterizations of $U$, we use the best fit values for the mixing angles from [120] ($\theta_{12} = 33.8°$, $\theta_{13} = 8.61°$, and $\theta_{23} = 49.7°$)

[2]While NOvA also has sensitivity to $\delta_{\text{PDG}}$, its data is currently not constraining [59].

in $U_{\rm PDG}$, which gives us the following for the magnitudes of the elements in the neutrino mixing matrix:

$$|U| = \begin{pmatrix} 0.822 & 0.550 & 0.150 \\ \sqrt{0.138 + 0.068\cos(\delta_{\rm PDG})} & \sqrt{0.293 - 0.068\cos(\delta_{\rm PDG})} & 0.754 \\ \sqrt{0.186 - 0.068\cos(\delta_{\rm PDG})} & \sqrt{0.405 + 0.068\cos(\delta_{\rm PDG})} & 0.640 \end{pmatrix} . \tag{4.5}$$

The preferred value of the Jarlskog for this parameterization as a function of the complex phase is

$$J = 0.0334\sin(\delta_{\rm PDG}) . \tag{4.6}$$

In Table 4.2, we show how to calculate the four parameters ($\theta'_{12}$, $\theta'_{13}$, $\theta'_{23}$, and $\delta'$) in six different parameterizations of $U$ in terms of the magnitudes of the elements of the matrix and the Jarlksog. Using the expressions in this table combined with Eqs. (4.5) and (4.6), we then plot the relationship between $\delta'$ vs $\delta_{\rm PDG}$ (as well as $\sin(\delta)$ and $\cos(\delta)$).

### 4.2.4 Results

The plotted results are shown in Fig. 4.1. Fig. 4.1 also shows that the effect of varying the mixing angles within their 3 $\sigma$ allowed values has a marginal impact on the values of $\delta'$ in other parameterizations. Varying the mixing angles significantly outside of these ranges, however, can have a dramatic effect on this figure.

We note that there are loops in the $\sin(\delta)$ plot but not in the $\cos(\delta)$ plot. That is, $\cos(\delta_{\rm PDG})$ uniquely determines $\cos(\delta')$, but $\sin(\delta_{\rm PDG})$ does not uniquely determine $\sin(\delta')$. This is because $\cos(\delta')$ comes from the norm of the elements of the matrix, and thus only depends on $\cos(\delta_{\rm PDG})$, while $\sin(\delta')$ comes from the Jarlskog, so it depends on $\sin(\delta_{\rm PDG})$ and $\cos(\delta_{\rm PDG})$ through the mixing angles.

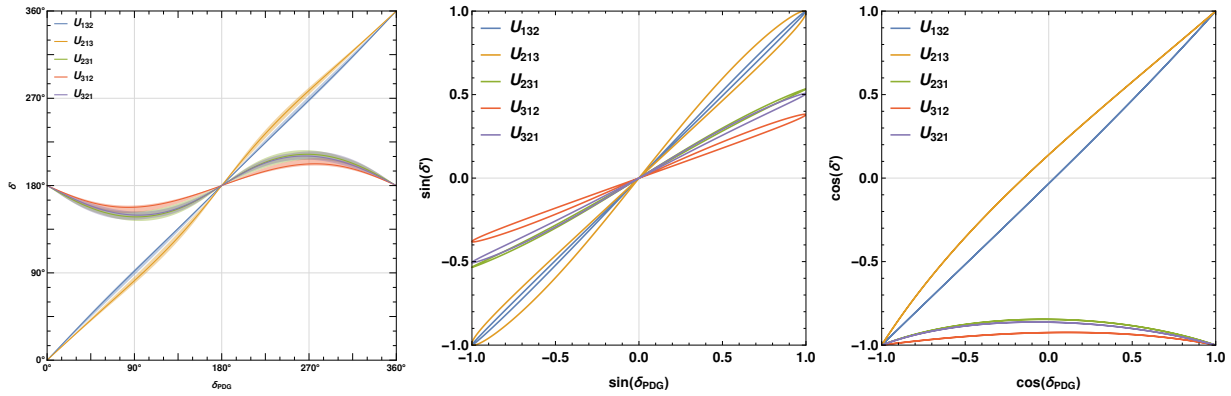


Figure 4.1: Comparison of the $CP$-violating phase of $U_{\rm PDG}$ ($\delta_{\rm PDG}$) and that of other parameterizations of the neutrino mixing matrix ($\delta'$). The shaded regions on the left plot show the range of variations of the curves over the 3 $\sigma$ range of mixing angles from [120].

An interesting feature of this plot is that for some of the alternative parameterizations of $U$, namely $U_{231}$, $U_{312}$, and $U_{321}$, $\delta'$ is restricted to a small domain just by our constraint of the three PDG mixing angles. The parameterizations for which $\delta'$ is bounded and whether it is bounded about $\delta' = 0$ or $\delta' = 180°$ are dependent on the mixing angles. Based on current measurements, the restriction is driven by the size of $\theta_{13}$ in the PDG parameterization or, alternatively, the relative smallness of $|U_{e3}|$. One can see this by looking at $|U_{e3}|$ in each parameterization, which is $s_{13}$ in $U_{\rm PDG}$ (see Table 4.3). In each of the parameterizations for which $\delta'$ is unbounded in Fig. 4.1, $|U_{e3}|$ is simple, whereas in each of the parameterizations for which $\delta'$ is bounded, $|U_{e3}|$ is complicated. Thus, in order to get the comparatively small value of $|U_{e3}|$ in those parameterizations for which $|U_{e3}| = \sqrt{A + B\cos(\delta')}$ with $A$ and $B$ comparatively large, we must have $\cos(\delta') \sim -1$. We can approximate the effect of small $|U_{e3}|$ on the allowed range of $\delta'$ in terms of PDG parameters by leveraging the smallness of $s_{13}$ to find

$$\max_{\delta_{\rm PDG}}[\cos(\delta')] \approx \frac{1}{2} d_{ijk}^2 - 1\,, \tag{4.7}$$

with

$$d_{231} \approx s_{13}\frac{1-s_{12}^2c_{23}^2}{s_{12}c_{12}s_{23}c_{23}} = 0.57\,, \qquad d_{312} \approx s_{13}\frac{1-c_{12}^2s_{23}^2}{s_{12}c_{12}s_{23}c_{23}} = 0.39\,,$$
$$\text{and} \qquad d_{321} \approx s_{13}\frac{1-s_{12}^2s_{23}^2}{s_{12}c_{12}s_{23}c_{23}} = 0.54 \tag{4.8}$$

for the three parameterizations with complicated $|U_{e3}|$. We then see that $\sin(\delta')$ is approximately contained within $\pm d_{ijk}$. In fact,

$$\sin(\delta') \approx d_{ijk}\sin(\delta_{\rm PDG})\,, \tag{4.9}$$

provides a simple approximation for the expressions shown in Fig. 4.1 and is accurate at the $\lesssim 10\%$ level (Eq. (4.7) is accurate to $< 2\%$). From Eq. (4.8), we can easily see how the three different parameterizations behave. For example, we see that $U_{213}$ and $U_{321}$ should be quite similar since they differ only by $c_{23}^2 \leftrightarrow s_{23}^2$, which are quite similar. Thus, swapping $U_{231}$ and $U_{321}$ is the same (up to higher order corrections) as changing the octant. Meanwhile, we see that the slope of $\sin(\delta')$ as a function of $\sin(\delta_{\rm PDG})$ is the smallest for $U_{312}$ (and thus $\delta'$ is the most constrained), since it has a factor $c_{12}^2$ instead of the factor of $s_{12}^2$. This is all consistent with the top right panel in Fig. 4.1.

Table 4.3: $U_{e3}$ in various parameterizations of $U$. The primed variables ($\theta'_{ij}$, $s_{ij'} \equiv \sin(\theta'_{ij})$, $c_{ij'} \equiv \cos(\theta'_{ij})$, $\delta'$) denote the parameters in the alternative parameterization and the unprimed variables ($\theta_{ij}$, $\delta_{\rm PDG}$, $c_\delta \equiv \cos(\delta_{\rm PDG})$) denote the parameters in $U_{\rm PDG}$. We also show an approximation for $|U_{e3}|$ in terms of the PDG parameterization variables at $\cos(\delta_{\rm PDG}) \approx 0$.

| $U_{ijk}$ | $U_{e3}(\theta'_{12}, \theta'_{13}, \theta'_{23}, \delta')$ | $\lvert U_{e3}(\delta', \delta_{\rm PDG}, \theta_{12} = 33.8^\circ, \theta_{13} = 8.61^\circ, \theta_{23} = 49.7^\circ)\rvert$ | $\approx \lvert U_{e3}(\delta', c_\delta \approx 0, \theta_{12}, \theta_{13}, \theta_{23})\rvert$ |
|---|---|---|---|
| $U_{132}$ | $c_{12'}s_{13'}$ | 0.150 | $s_{13}$ |
| $U_{213}$ | $s_{13'}c_{23'}$ | 0.150 | $s_{13}$ |
| $U_{231}$ | $s_{13'}c_{23'}e^{-i\delta'} + s_{12'}c_{13'}s_{23'}$ | $\frac{\sqrt{0.108-0.007c_\delta+0.005c_\delta^2+0.085\cos(\delta')\sqrt{1.62-0.17c_\delta-0.34c_\delta^2+0.07c_\delta^3}}}{0.861-0.068c_\delta}$ | $\frac{2s_{12}c_{12}s_{23}c_{23}}{1-s_{12}^2c_{23}^2}\lvert\cos(\delta'/2)\rvert$ |
| $U_{312}$ | $c_{12'}s_{13'}e^{-i\delta'} + s_{12'}c_{13'}s_{23'}$ | $\frac{\sqrt{0.105-0.024c_\delta+0.005c_\delta^2+0.048\cos(\delta')\sqrt{4.74-2.04c_\delta-0.08c_\delta^2+0.07c_\delta^3}}}{0.595-0.068c_\delta}$ | $\frac{2s_{12}c_{12}s_{23}c_{23}}{1-c_{12}^2s_{23}^2}\lvert\cos(\delta'/2)\rvert$ |
| $U_{321}$ | $s_{12'}s_{23'} + c_{12'}s_{13'}c_{23'}e^{-i\delta'}$ | $\frac{\sqrt{0.108+0.018c_\delta+0.005c_\delta^2+0.108\cos(\delta')\sqrt{1+0.29c_\delta-0.16c_\delta^2-0.03c_\delta^3}}}{0.814+0.068c_\delta}$ | $\frac{2s_{12}c_{12}s_{23}c_{23}}{1-s_{12}^2s_{23}^2}\lvert\cos(\delta'/2)\rvert$ |

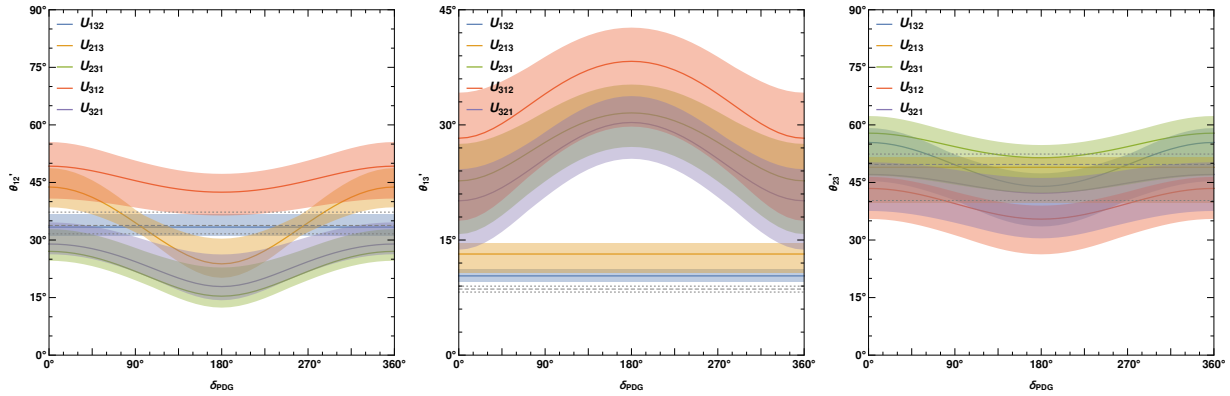


Figure 4.2: Mixing angles in each parameterization as a function of $\delta_{\rm PDG}$. The shaded regions show the range of variations of the curves over the 3 $\sigma$ range of mixing angles from [120] while the dashed (dotted) gray lines are best fit values (maxima and minima of 3 $\sigma$ ranges) in the standard parameterization.

We show the values of the three mixing angles in the different parameterizations in Fig. 4.2, along with bands representing the region covered by these curves when the mixing angles in $U_{\rm PDG}$ are allowed to vary independently within their 3 $\sigma$ ranges. We note that $\theta'_{12}$ is only independent of $\delta_{\rm PDG}$ in $U_{132}$ while $\theta'_{23}$ is only independent of $\delta_{\rm PDG}$ in $U_{213}$. On the other hand, $\theta'_{13}$ is independent of $\delta_{\rm PDG}$ in both $U_{132}$ and $U_{213}$. We can also see how the precision on the different oscillation parameters changes in different parameterizations[3]. Notably $\theta'_{13}$ is quite a bit less precise in other parameterizations, in particular those with complicated $U_{e3}$ elements.

We also show the reduced Jarlskog in different parameterizations as a function of $\delta_{\rm PDG}$ in Fig. 4.3. The reduced Jarlskog is defined by,

$$J'_r \equiv \frac{J'}{\sin(\delta')} \,. \tag{4.10}$$

(See Table 4.1 for explicit expressions in each of the parameterizations considered.) This

[3]In the $U_{123}$ parameterization, there is some dependence on the constraints from $\delta_{\rm PDG}$; these correlations are ignored here for simplicity.

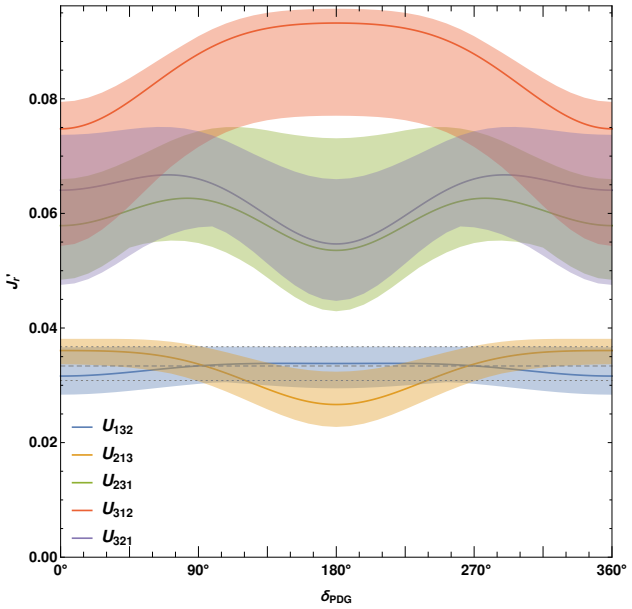


Figure 4.3: The "reduced Jarlskog" $J_r' \equiv \frac{J}{\sin(\delta')}$ for each parameterization as a function of $\delta_{\text{PDG}}$. The shaded regions show the range of variations of the curves over the 3 $\sigma$ range of mixing angles from [120]. The dashed gray line is $J_r$ for $U_{\text{PDG}}$ using the best fit mixing angles from [120] and the dotted gray lines are the maximum and minimum of $J_r$ for $U_{\text{PDG}}$ when allowing the mixing angles to vary over their 3 $\sigma$ ranges. The sharp features are due to switching the preferred octant of $\theta_{23}$.

quantity represents the contribution to the Jarlskog from the mixing angles in a given parameterization. We can see that in the parameterizations with complicated expressions for $U_{e3}$ ($U_{231}$, $U_{312}$, and $U_{321}$), the reduced Jarlskog is notably much larger than it is in the parameterizations with simple expressions for $U_{e3}$ ($U_{123}$, $U_{132}$, and $U_{213}$). This provides another means of showing why $\sin(\delta')$ in some parameterizations is restricted in its allowed range, as shown in Fig. 4.1 and Eqs. (4.7)-(4.9).

To further understand the impact of $|U_{e3}|$ on the tightly constrained nature of $\cos(\delta')$ in other parameterizations, we plotted the allowed range (assuming $\delta_{\text{PDG}}$ is unconstrained) of $\delta'$ for various different parameterizations as a function of $\theta_{13}$ in the PDG definition in Fig. 4.4, with all the other mixing angles fixed. In the $U_{132}$ parameterization, $\delta'$ is always unconstrained for any value of $\theta_{13}$ up to 45°. For $U_{213}$, $\delta'$ is unconstrained until $\theta_{13} > 35°$ past which point

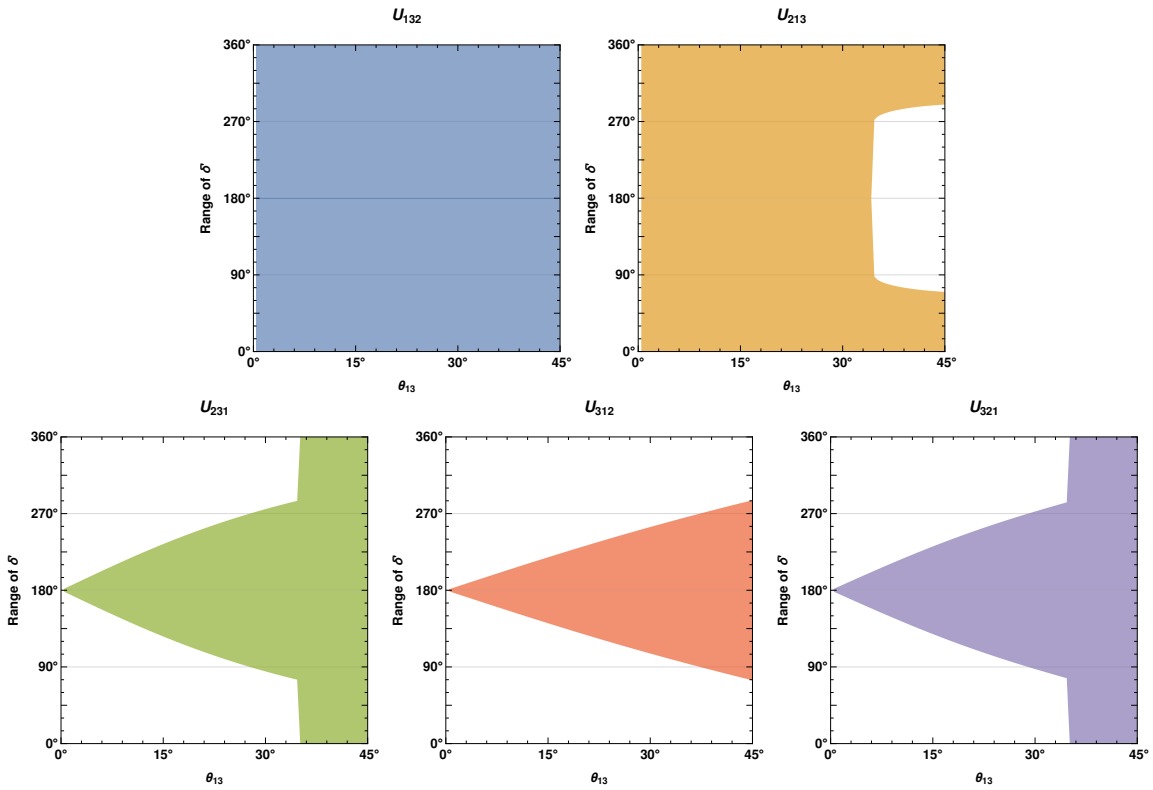


Figure 4.4: The allowed range of $\delta'$ in various parameterizations of the neutrino mixing matrix as a function of $\theta_{13}$ in the PDG parameterization. We have fixed the other mixing angles to their best fit values while $\delta_{\rm PDG}$ is unconstrained.

$\cos(\delta')$ is constrained to be near 1. In the three remaining parameterizations, we see that $\cos(\delta')$ is constrained to be near $-1$ and that the allowed region increases as $\theta_{13}$ increases roughly linearly with $\theta_{13}$ for smaller values of $\theta_{13}$, which is consistent with $d_{ijk} \propto s_{13}$ (see Eq. (4.8)).

Next generation long-baseline accelerator experiments are aiming to not only detect CPV, but measure it with some precision. Various targets on the precision on $\delta_{\rm PDG}$ have been presented based on theoretical concerns motivated by discrinimating among different flavor symmetries. The 2013 Snowmass report stressed $\Delta\delta_{\rm PDG} = 15^\circ$ as an important goal [121] and a more recent theory overview emphasized $\Delta\delta_{\rm PDG} = 10^\circ$ [122] as a useful target. We take as a benchmark number $\Delta\delta_{\rm PDG} = 15^\circ$ and plot the corresponding $\Delta\delta'$ (with fixed mixing

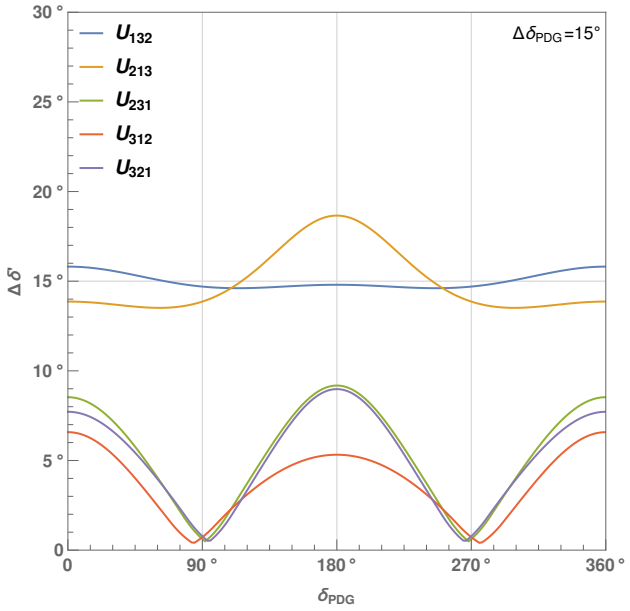


Figure 4.5: Uncertainty of the $CP$-violating phase of alternate parameterizations of the neutrino mixing matrix ($\delta'$) as a function of $\delta_{\rm PDG}$, given an uncertainty on $\delta_{\rm PDG}$ of 15°.

angles) in the other parameterizations for various values of $\delta_{\rm PDG}$ (see Fig. 4.5). We find that in different parameterizations of the lepton mixing matrix, a precision on $\delta_{\rm PDG}$ of 15° will lead to extremely different precision in different parameterizations, in particular in the three parameterizations with complicated expressions for $U_{e3}$. In Fig. 4.5, we see that while $U_{132}$ and $U_{213}$ aren't too different from the PDG parameterization (as seen before), in the other three parameterizations, a measurement of $\delta_{\rm PDG}$ to within 15° precision could result in $\sim 1°$ precision on $\delta'$, depending on the parameterization and the value of $\delta_{\rm PDG}$. In addition, since the Jarlskog (and thus the precision on the Jarlskog) is the same in each parameterization, Fig. 4.5 indicates that the precision on the mixing angles, in particular $J_r \equiv c_{12}s_{12}c_{13}^2 s_{13}c_{23}s_{23}$, is comparable in $U_{132}$ and $U_{213}$ as in the PDG parameterization. Meanwhile, since $\delta'$ (and thus $\sin\delta'$) becomes more precise in $U_{231}$, $U_{312}$, and $U_{321}$, the mixing angles must become less precise in those parameterizations to compensate, as confirmed in Fig. 4.3. This is due to the fact that $U_{231}$, $U_{312}$, and $U_{321}$ have complicated $U_{e3}$ elements while the others all have simple $U_{e3}$ elements.

### 4.2.5 Discussion

As we have seen in Fig. 4.1, in some parameterizations, in particular $U_{213}$, $U_{312}$, and $U_{321}$, $\cos(\delta')$ is restricted to be $\lesssim -0.8$, and correspondingly, $|\sin(\delta')| \lesssim 0.6$. That is, if the lepton mixing matrix was parameterized differently, we would already know that $150^\circ \lesssim \delta' \lesssim 210^\circ$ (and, given T2K's preference for $170^\circ \lesssim \delta_{\rm PDG} \lesssim 360^\circ$, this implies that $170^\circ \lesssim \delta' \lesssim 210^\circ$). This highlights the fact that $\delta_{\rm PDG} = \pm 90^\circ$ by itself is not maximal in any fundamental way; it does lead to the largest amount of CPV allowed *given the other measured oscillation parameters*.

In much of the previous discussion and figures, we have assumed that we have measured the three oscillation parameters perfectly and have no information on $\delta_{\rm PDG}$. In reality, of course, each of the four parameters are somewhat constrained, although $\delta_{\rm PDG}$ is largely unconstrained at the moment except via T2K appearance data. We have verified, however, that even over the allowed 3 $\sigma$ range of $40^\circ \lesssim \theta_{23} \lesssim 50^\circ$ (and even quite a bit beyond this), $\cos(\delta')$ is restricted in 3 of the parameterizations to a region near $-1$, and there is a corresponding constraint on $\sin(\delta')$, as shown by the shaded regions in Fig. 4.1.

The strongest constraint on CPV currently comes from T2K [58]. T2K has measured a high amount of neutrino appearance and a low amount of anti-neutrino appearance, implying that $J < 0$ at close to 3 $\sigma$. In addition, they seem to see slightly more neutrino events and fewer anti-neutrino events than allowed by $\delta_{\rm PDG} = 270^\circ$ given other constraints, although this tension is at low significance. Nonetheless, T2K has interpreted this as a constraint on $\theta_{13}$, which (very weakly) suggests a larger value than that from precise medium baseline reactor experiments [123–125]. In this analysis, however, they assume priors on solar parameters. If, instead, a prior on $\theta_{13}$ from reactors was used since it is extremely well measured, one would find that this slight tension could be more somewhat more easily accommodated in terms of

a constraint on solar parameters.

We now take this slight tension seriously and consider the implications if it persists with additional data. If it is confirmed at high precision, then we would look to the constraint on the other oscillation parameters, since the measurement depends on $c_{13}^2 s_{13} c_{12} s_{12} c_{23} s_{23} \frac{\Delta m_{21}^2}{\Delta m_{31}^2}$ up to matter effects. Based on the best fit value for $\theta_{13}$ from T2K, this results in a 14% excess in this quantity. The 1 $\sigma$ allowed regions for $c_{13}^2 s_{13}$, $c_{12} s_{12}$, $\Delta m_{31}^2$, and $\Delta m_{21}^2$ are 1.4%, 1.1%, 1.3%, and 2.8%. This suggests that the best place to understand any tension in the T2K data with the rest of the oscillation data is in terms of the solar mass splitting[4]. We note that the matter effect only slightly modifies the situation at T2K, as the corrections to the Jarlskog can be determined in a straightforward fashion [126], as can the corrections to the $\Delta m_{ij}^2$'s [127, 128].

In addition, T2K's constraint on $\delta_{\rm PDG}$ is that it is constrained to within $[165°, 358°]$ at 3 $\sigma$, which is about half the allowed space using a uniform prior on $\delta_{\rm PDG}$[5]. However, we find that if the lepton mixing matrix was parameterized as $U_{312}$, the allowed range on the complex phase is only $[173°, 208°]$ including the 3 $\sigma$ uncertainty on the oscillation parameters. This is only 7.5% of the total $\delta'$ space, compared with 53.6% of the total $\delta_{\rm PDG}$ space. Similarly, small regions exist for the $U_{231}$ and $U_{321}$ parameterizations. Note that this means that in the $U_{312}$ parameterization, the uncertainty is already down to $\Delta\delta' = 18°$ at 3 $\sigma$ CL, accounting for the uncertainty in the oscillation parameters.

Thus, we propose that a more useful metric for quantifying $CP$ violation is amount of allowed Jarlskog space. Extracting the Jarlskog only requires (up to matter effects) knowing the ratio of $\Delta m^2$'s (and really just $\Delta m_{21}^2$, as T2K measures $\Delta m_{31}^2$) as opposed to $\sin(\delta_{\rm PDG})$, which also

[4]While it is interesting to note that there was a slight tension in the solar mass splitting data, it goes in the wrong direction to explain the T2K tension.

[5]The Haar measure applied to lepton mass mixing indicates that the correct prior on the complex phase is uniform in $\delta$ under the assumption of anarchy, instead of $\sin(\delta)$ or other possible choices [129].

requires knowing $\theta_{13}$, $\theta_{12}$, and $\theta_{23}$. The Jarlskog is always within the range $J \in [-\frac{1}{6\sqrt{3}}, \frac{1}{6\sqrt{3}}]$, which numerically is $[-0.096, 0.096]$. These maximum (minimum) values of $J$ occur when $\theta_{12} = \theta_{23} = 45°$, $\theta_{13} = \text{atan}\big(1/\sqrt{2}\big) = 35.3°$, and $\sin(\delta_{\text{PDG}}) = +1$ ($\sin(\delta_{\text{PDG}}) = -1$). From nu-fit v4.0, it is found that the allowed range is reduced to $[-0.033, 0.033]$ without including any $\sin(\delta_{\text{PDG}})$ information. This represents 35% of the total allowed space, and it mostly comes from the fact that $\theta_{13} = 8.6°$ is small compared to the value for maximal CPV, 35.3°. A subleading contribution comes from the fact that $\theta_{12} = 34°$, compared to 45°, which results in a reduction in the allowed space to 93%. Thus given T2K's measurement, the allowed space of the Jarlskog is about 22%, which is a parameterization independent statement.

We also note that certain parameterizations are very similar. In particular, we see in Fig. 4.1 that $U_{123}$ (the PDG parameterization) is quite similar to $U_{132}$. In addition, $U_{231}$ is quite similar to $U_{321}$. Thus, we can conclude that $U_2$ and $U_3$ roughly commute within the context of the discussion of CPV. That is, the effect of $\delta'$ in the different parameterizations doesn't change much when commuting $U_2$ and $U_3$. This makes sense since the associated angles in the PDG parameterization, $\theta_{13}$ and $\theta_{12}$ are the two smallest angles, so while rotations are not commutative in general, the correction scales with the size of the rotations.

Before concluding this section, we make one comment on the usefulness of $\delta$ in a given parameterization (or $\delta_{\text{PDG}}$ in the usual parameterization). While we have extensively demonstrated the shortcomings of $\delta$ in general and as a proxy for understanding $CP$ violation, as well as the benefit of using the Jarlskog to quantify the amount of $CP$ violation in the leptonic mass matrix, there is still some value in the $\delta$ quantity. In particular, it comes from the goal of physics to measure everything. That is, measuring the Jarlskog with arbitrary precision, as well as three rotation angles, leaves one sign undetermined: the sign of $\cos\delta$. While the sign of $\cos\delta$ does not affect $CP$ violation, it is still a fundamental parameter in the Standard Model and is physical, and thus it must be measured. Thus we do not advocate entirely

ignoring measurements of $\delta$ as measuring parameters in the Standard Model is the primary goal of particle physics, but we do encourage experimentalists and theorists to focus on the Jarlskog when discussing $CP$ violation.

### Conclusion

Three of the four degrees of freedom in the lepton mixing matrix have been measured reasonably well. In the standard PDG parameterization, these parameters are labeled $\theta_{12}$, $\theta_{13}$, and $\theta_{23}$. The final parameter, $\delta_{\text{PDG}}$, is related to the amount of $CP$ violation (CPV) in the lepton sector affecting neutrino oscillations. While it is certainly the case that $\sin(\delta_{\text{PDG}}) = 0$ implies no CPV in neutrino oscillations and $\sin(\delta_{\text{PDG}}) \neq 0$ is proof of CPV (given that all three mixing angles are non-zero), $\delta_{\text{PDG}}$ and CPV in neutrino oscillations are not exactly equivalent concepts. One clear way to see this is that in different parameterizations with one complex phase, the allowed range of the new phase $\delta'$ may be already severely constrained, as shown in Fig. 4.1, without even considering any constraint on $\delta_{\text{PDG}}$ coming from T2K or other experiments. This also highlights the fact that the precision with which $\delta_{\text{PDG}}$ is measured is not truly fundamental (see Fig. 4.5), so the precision on the Jarlskog should be considered instead. The cause of the surprisingly strong constraint on $\delta'$ in certain other parameterizations without any information on $\delta_{\text{PDG}}$ is the smallness of $|U_{e3}|$, which requires a fairly strong cancellation, which only happens for $\cos(\delta')$ near $-1$.

We use this time to revisit the topic of optimality with regards to the choice of parameterization for the leptonic mixing matrix in the context of neutrino oscillations, giving the presently known data[6]. While this is of course a matter of taste, we here list some desirable features of a matrix:

[6]There are other potentially interesting criteria such as computational efficiency, for which $SU(N)$ generators may be more efficient than rotations [130].

- Since $|U_{e3}|$ is small, it is favorable to have a simple element there; this picks out parameterizations $U_{123}$, $U_{132}$, or $U_{213}$.

- It is useful to be able to write approximate two-flavor oscillations as a simple function of a single mixing angle for the various experimental probes that are available to us. By looking at solar ($U_{e2}$), medium-baseline reactor ($U_{e3}$), and long-baseline accelerator/atmospheric disappearance ($U_{\mu 3}$), we find that the preferred parameterizations from Table 4.2 (i.e. parameterizations in which the element concerned is simple) are:

| | $U_{123}$ | $U_{132}$ | $U_{213}$ | $U_{231}$ | $U_{312}$ | $U_{321}$ |
|---|---|---|---|---|---|---|
| $\|U_{e2}\|$ | ✓ | ✓ | ✗ | ✗ | ✓ | ✗ |
| $\|U_{e3}\|$ | ✓ | ✓ | ✓ | ✗ | ✗ | ✗ |
| $\|U_{\mu 3}\|$ | ✓ | ✗ | ✓ | ✓ | ✗ | ✗ |

The only parameterization that satisfies all of these conditions is $U_{123}$, which is the same as the PDG parameterization (without the Majorana phases). The only remaining choice is the location of the oscillation phase on one of the three rotations: $U_1$, $U_2$, or $U_3$. As this does not lead to any redefinition of the phase other than possibly a sign, its location is less important than the order of rotations. Nonetheless, there are some theoretical benefits to putting the phase on $U_1$ (the $\theta_{23}$ rotation) instead of the more conventional $U_2$ (the $\theta_{13}$ rotation) when discussing the matter effect, see e.g. [127, 131]. For consistency, however, we recommend that in most applications, the conventional PDG parameterization, including associating the phase with the $\theta_{13}$ rotation, should be used; see Eq. (4.3).

In addition, one could examine the impact the choice of parameterization has on a given symmetry structure such tribimaximal, trimaximal, golden ratio, and others along with their modifications [132–137]. Since these are typically written in the PDG parameterization, the statements in this article apply in a straightforward fashion to each model. That is,

if a given model predicts a certain range for $\delta_{\rm PDG}$, then in a different parameterization, that range would be given by Fig. 4.1. Nonetheless, one could investigate whether or not the sum rules connected with various models exhibited any useful simplifications in certain parameterizations; this is, however, beyond the scope of the present article.

Finally, as neutrino oscillation measurements improve and the values of the lepton mixing matrix fall into sharp relief, we hope that when quantifying the amount of CPV present, the Jarlskog is used, which depends on all four parameters in any parameterization, instead of just $\delta_{\rm PDG}$.

**Acknowledgements**

We thank Stephen Parke for useful conversations. PBD acknowledges the United States Department of Energy under Grant Contract desc0012704. The work presented here that RP did was supported by the U.S. Department of Energy, Office of Science, Office of Workforce Development for Teachers and Scientists, Office of Science Graduate Student Research (SCGSR) program. The SCGSR program is administered by the Oak Ridge Institute for Science and Education (ORISE) for the DOE. ORISE is managed by ORAU under contract number DE-SC0014664. All opinions expressed in this paper are the authors' and do not necessarily reflect the policies and views of DOE, ORAU, or ORISE.

# Chapter 5

# Neutrino Non-Standard Interactions in Oscillation Experiments

## 5.1 Preface

The long distances neutrinos travel through the earth in long-baseline experiments make these experiments much more sensitive to the matter effect. So, if there are any interactions between neutrinos and ordinary matter in addition to the ones in the standard model, these neutrino Non-Standard Interactions (NSIs) would modify the matter effect, and the effects could be seen as inconsistencies when comparing data from a long-baseline experiment with data from an experiment with a significantly different baseline. We need to be careful to rule out such possibilities before interpreting the data as telling us about the parameters in the standard oscillation picture.

In the last data sets released by T2K and NO$\nu$A, there is a tension between the results of their analyses. Since T2K and NO$\nu$A have significantly different baselines, NSIs could have

a role in this discrepancy. In this chapter, we investigate this possibility in as general of a way as we can.

### 5.1.1 Attributions

Section 5.2 is a reproduction, with slight modifications, of a paper to which I contributed that was published in Physical Review Letters:

Peter B. Denton, Julia Gehrlein, and Rebekah Pestes. *CP-Violating Neutrino Nonstandard Interactions in Long-Baseline-Accelerator Data*. Phys. Rev. Lett. **126**, 051801 (2021). doi:10.1103/PhysRevLett.126.051801. arXiv:2008.01110.

Julia Gehrlein and I both gathered the needed data from plots by T2K and NO$\nu$A and found the parameters needed to give the best fit of Eq. (5.4) to the data gathered. Peter Denton took our results and used them in his code to make Figs. 5.1, 5.2, 5.3, and 5.4, as well as Table 5.1. The approximations were calculated by Peter Denton and Julia Gehrlein.

## 5.2 $CP$-Violating Neutrino Non-Standard Interactions in Long-Baseline-Accelerator Data

### 5.2.1 Abstract

Neutrino oscillations in matter provide a unique probe of new physics. Leveraging the advent of neutrino appearance data from NOvA and T2K in recent years, we investigate the presence of $CP$-violating neutrino non-standard interactions in the oscillation data. We first show how to very simply approximate the expected NSI parameters to resolve differences between two

long-baseline appearance experiments analytically. Then, by combining recent NOvA and T2K data, we find a tantalizing hint of $CP$-violating NSI preferring a new complex phase that is close to maximal: $\phi_{e\mu}$ or $\phi_{e\tau} \approx 3\pi/2$ with $|\epsilon_{e\mu}|$ or $|\epsilon_{e\tau}| \sim 0.2$. We then compare the results from long-baseline data to constraints from IceCube and COHERENT.

### 5.2.2 Introduction

Neutrino oscillations have provided the only particle physics evidence for new physics beyond the standard model (BSM) to date [22, 64], making it an excellent place to probe new physics scenarios. The phenomenology of neutrino oscillations is fairly unique, as it provides an opportunity to observe the accumulation of a relative phase over macroscopic distances, making neutrino oscillations one of the purest probes of quantum mechanics available. During propagation, the environment may also modify the phases due to an interaction. Such an interaction exists in the standard model (SM) and is called the Wolfenstein matter effect [16], wherein a neutrino in the electron state of the flavor basis experiences a potential with the background electrons via a charged-current (CC) interaction.

In the same paper that pointed out the SM matter effect, Wolfenstein also suggested the possibility of a new interaction that provides a matter effect, so-called neutrino non-standard interactions (NSI) [16, 138, 139]. Since then, there has been an explosion of interest to probe these new interactions. Numerous UV-complete models have been developed [140–147][1] and the phenomenology has been generalized beyond vector currents [148–151]. In addition, several NSI parameters introduce various interesting degeneracies in oscillation or scattering experiments [78–80, 82–87, 90–95, 98, 99, 138, 152–161], which demonstrates the importance of complementary measurements of the NSI parameters.

[1] These models allow for sizable NSI via various mechanisms such as constraining the direct coupling of the NSI mediator to the heavier generations or to sterile neutrinos that mix with the active ones.

One of the most complete ways to probe neutrino oscillations is through long-baseline accelerator experiments with electron (anti)neutrino appearance. While these measurements are extremely challenging experimentally, they provide a wealth of information, as they are sensitive to many oscillation parameters, including those that are the least constrained, like the CP-violating phase $\delta$ from the leptonic mass mixing matrix. In addition, appearance measurements provide a crucial probe of certain NSI parameters.

The two state-of-the-art long-baseline neutrino experiments are NOvA and T2K [162, 163]. Both are off-axis; therefore, each detects a flux of neutrinos with a relatively narrow energy distribution. The latest results from both experiments [164, 165] show a slight tension at the $\sim 2\sigma$ level, depending on how exactly it is quantified. Both experiments prefer the normal mass ordering, but T2K prefers $\delta \sim 3\pi/2$ while NOvA does not have much preference and is generally around $\delta \sim \pi$. While this is not yet significant, it provides an interesting test case for new physics should it persist, as both experiments plan to accumulate additional data.

The parameters for this tension are particularly interesting. Since a new physics explanation probably has to depend on the matter effect and since T2K with less matter effect sees some evidence of CPV, this means that CPV is present not only in the mass matrix but also in the new physics sector. Thus we are presenting evidence of two cases of relatively "large" CPV in the neutrino sector. Given the complex picture of CP with some parts of physics violating it maximally and others seeming to conserve it, these hints for extra CPV play a crucial role in our larger understanding of CP symmetry in physics.

In this paper, we review NSI and show how to approximate the NSI parameters that describe the NOvA and T2K data. We then describe our treatment of the NOvA and T2K data. Then, we show that the NOvA and T2K data can be resolved by the inclusion of NSI with complex CPV phases with a preference for CPV values over CP-conserving values. Finally, we discuss our results in a broader picture of other neutrino measurements and present some possible

plans to improve these results, and we conclude.[2] All the relevant data files are available at peterdenton.github.io/Data/NOvA+T2K_NSI/index.html.

### 5.2.3 Methods

#### NSI Overview

NSI in oscillations provides an additional contribution to the matter potential of the neutrino oscillation Hamiltonian in the weak basis

$$H = \frac{1}{2E}\left[U^\dagger M^2 U + a\begin{pmatrix} 1+\epsilon_{ee} & \epsilon_{e\mu} & \epsilon_{e\tau} \\ \epsilon_{e\mu}^* & \epsilon_{\mu\mu} & \epsilon_{\mu\tau} \\ \epsilon_{e\tau}^* & \epsilon_{\mu\tau}^* & \epsilon_{\tau\tau}\end{pmatrix}\right], \tag{5.1}$$

where $E$ is the neutrino energy, $U \equiv R_{23}(\theta_{23})U_{13}(\theta_{13},\delta)R_{12}(\theta_{12})$ is the PMNS mixing matrix [14, 15] that is parameterized in the usual way [13], $M^2 \equiv \text{diag}(0, \Delta m^2_{21}, \Delta m^2_{31})$ is the diagonal mass-squared matrix, $a \equiv 2\sqrt{2}G_F N_e E$ parameterizes the matter effect, and $N_e$ is the electron density. The $\epsilon_{\alpha\beta}$ terms parameterize the size of the new interaction relative to the weak interaction and typically arise from effective Lagrangians of the form

$$\mathcal{L}_{\text{NSI}} = -2\sqrt{2}G_F \sum_{\alpha,\beta,f} \epsilon^f_{\alpha\beta}(\bar{\nu}_\alpha\gamma^\mu\nu_\beta)(\bar{f}\gamma_\mu f)\,. \tag{5.2}$$

For simplicity, we only consider NSI with vector mediators. The Lagrangian level NSI parameters in Eq. (5.2) are related to the Hamiltonian level terms in Eq. (5.1) by $\epsilon_{\alpha\beta} = \sum_f \frac{N_f}{N_e}\epsilon^f_{\alpha\beta}$, where $N_f$ is the number density of fermion $f$. In the context of oscillations, it isn't possible to identify which matter particles (electrons, up quarks, or down quarks) the new physics is

[2] We also provide supplemental material for a derivation of some of our analytic results, our results in the standard oscillation picture, and some additional NSI results which includes [61, 77, 123, 166–176].

coupled to without comparing neutrino trajectories through materials with different neutron fractions, such as the Earth and the sun. Within the context of long-baseline trajectories through the crust, the neutron fraction is close to one. While the NSI parameters are often taken to be real for simplicity, we consider complex NSI, where $\epsilon_{\alpha\beta} = |\epsilon_{\alpha\beta}|e^{i\phi_{\alpha\beta}}$ for $\alpha \neq \beta$, which violate CP [78, 177, 178], see ref. [179] for more on complex NSI. Diagonal non-universal NSI [180] does not lead to CPV assuming CPT invariance and will not be considered here.

One can analytically estimate the magnitude of the NSI parameter that would resolve different measurements of $\delta$ in experiments experiencing distinct matter potentials. We find that if two experiments at two different matter potentials measure two disparate values of $\delta$ due to $\epsilon_{e\beta}$ NSI for $\beta \in \{\mu, \tau\}$, the magnitude of the NSI in the normal ordering (NO) is approximately given by

$$|\epsilon_{e\beta}| \approx \frac{s_{12}c_{12}c_{23}\pi\Delta m^2_{21}}{2s_{23}w_\beta}\left|\frac{\sin\delta_{\rm T2K} - \sin\delta_{\rm NOvA}}{a_{\rm NOvA} - a_{\rm T2K}}\right| \approx \begin{cases} 0.22 & \text{for } \beta = \mu \\ 0.24 & \text{for } \beta = \tau \end{cases}, \tag{5.3}$$

where $w_\beta = s_{23}$ or $c_{23}$ for $\beta = \mu$ or $\tau$ respectively[3], see the supplemental material for a derivation. The preferred value of $\epsilon_{e\tau}$ is larger than that for $\epsilon_{e\mu}$ since T2K prefers the upper octant and T2K is less affected by NSI than NOvA. The difference between $\epsilon_{e\mu}$ and $\epsilon_{e\tau}$ makes sense since long-baseline oscillations are dominated by $\nu_3$, which contains more $\nu_\mu$ in the upper octant, and thus not as much NSI affecting $\nu_\mu$ is required to produce a given effect. We also note that the approximations presented here are quite consistent with our numerical results discussed below and shown in Fig. 5.1 and Table 5.1. In addition, in some regions of

[3]We use the standard $c_{ij} = \cos\theta_{ij}$, $s_{ij} = \sin\theta_{ij}$ shorthand.

parameter space, it may be possible to connect $\delta$ and the NSI phases via a technique known as phase reduction [153, 181].

**Analysis Details**

The appearance channels at NOvA and T2K can be approximated by counting experiments, while for the disappearance channels, the energy distribution of the events is important. This approximation ignores several potentially problematic issues: the energy distributions aren't exactly delta distributions, there are correlated systematics between the different channels, and the cross section systematics may well be related even between the different experiments. Nonetheless, we find an acceptable reproduction of the results with the simple treatment described below.

NOvA measures neutrinos with $E \sim 1.9$ GeV after traveling 810 km through the Earth with density $\rho = 2.84$ g/cc, while T2K measures neutrinos with $E = 0.6$ GeV after traveling 295 km through the Earth with average density $\rho = 2.6$ g/cc. For the appearance channels, we find that the number of events can be expressed as a constant normalization term and a constant factor which multiplies the oscillation probability in matter (see also [182] for a similar approach). These constant factors can be derived from the provided bi-event plots in [164, 165, 183]. As wrong sign leptons contribute to the flux, especially in antineutrino mode, we parameterize the predicted numbers of events as

$$n(\nu_e) = xP(\nu_\mu \to \nu_e) + yP(\bar{\nu}_\mu \to \bar{\nu}_e) + z\,, \tag{5.4}$$

and similarly for the antineutrino channel, where $x,\ y,\ z$ are real numbers which roughly translate to the weighted neutrino (antineutrino) flux times cross-section for this particular

energy, and the background rate in this channel[4]. For NOvA, a good fit is obtained for the neutrino channel without including the wrong sign leptons,

$$n(\nu_e)^{\mathrm{NOvA}} = 31.15 + 1149.7 \times P(\nu_\mu \to \nu_e) \ , \tag{5.5}$$

$$n(\bar{\nu}_e)^{\mathrm{NOvA}} = 13.97 + 472.60 \times P(\bar{\nu}_\mu \to \bar{\nu}_e) + 22.96 \times P(\nu_\mu \to \nu_e) \, , \tag{5.6}$$

while for T2K, we find

$$n(\nu_e)^{\mathrm{T2K}} = 19.71 + 1284.16 \times P(\nu_\mu \to \nu_e) + 36.90 \times P(\bar{\nu}_\mu \to \bar{\nu}_e) \ , \tag{5.7}$$

$$n(\bar{\nu}_e)^{\mathrm{T2K}} = 5.84 + 231.32 \times P(\bar{\nu}_\mu \to \bar{\nu}_e) + 49.51 \times P(\nu_\mu \to \nu_e) \ . \tag{5.8}$$

At leading order, the oscillation probability for neutrinos and antineutrinos is the same for the disappearance channel. However, this changes in the presence of NSI. In the following, we will assume that the results in the disappearance channel are dominated by the neutrino sample, which provides higher statistics than the antineutrino sample. We adapt the results from [182] for the disappearance channel at NOvA, where they found as best fit $|\Delta m^2_{32}| = (2.41 \pm 0.07) \times 10^{-3}$ eV$^2$ and $4|U_{\mu 3}|^2(1 - |U_{\mu 3}|^2) = 0.99 \pm 0.02$. For T2K, we obtain the test statistic for $\theta_{23}$ and $\Delta m^2_{32}$ from the 1D distributions of the test statistics provided by the experiment [164][5].

For the appearance channel, incorporating the effect of NSIs as described in Eq. (5.1) is

[4]Unlike other recent analyses of NOvA and T2K data, we include the wrong sign lepton contribution as it considerably improves our description of the experiment.

[5]While these distributions do include information from the appearance mode, we assume that they are dominated by the high statistics measurements made in disappearance mode.

straightforward. For the disappearance channels, we calculate the effective vacuum mixing parameters by solving

$$U^\dagger M^2 U + A + N = \widetilde{U}^\dagger \widetilde{M}^2 \widetilde{U} + A\,, \tag{5.9}$$

where $A \equiv \mathrm{diag}(a, 0, 0)$ and the $N$ matrix contains the $\epsilon$'s and is proportional to the matter potential $a$. Then, by diagonalizing $U^\dagger M^2 U + N$, one finds the vacuum parameters that a long-baseline accelerator experiment would extract in the presence of NSI at a given energy. Various approximate techniques for the diagonalization of matrices in the context of neutrino oscillations in matter have been explored in [127, 128, 184–189]. The approach presented in Eq. (5.9) is exact in the case of constant matter density; it does not apply to solar or atmospheric neutrinos, and additional care is necessary there. Finally, one can compare the effective vacuum mixing parameters extracted from $\widetilde{M}^2$ and $\widetilde{U}$ to the measured oscillation parameters.

To analyze the data, we construct a test statistic using a log likelihood ratio with Poisson statistics for the appearance data and simple $\chi^2$ pulls for the disappearance constraints. We show the results in the standard oscillation picture in the supplemental material, which show the preference for the IO when the two experiments are combined without NSI.

In the next section, we find that, in the presence of NSI however, the long-baseline data is better described by the NO than the IO, so we assume the true mass ordering is normal, unless otherwise specified. This is crucial as the mass ordering affects many other experiments including end point, neutrinoless-double-beta decay, and cosmological measurements. The MO can be confirmed independently of the presence of NSI via JUNO [190].

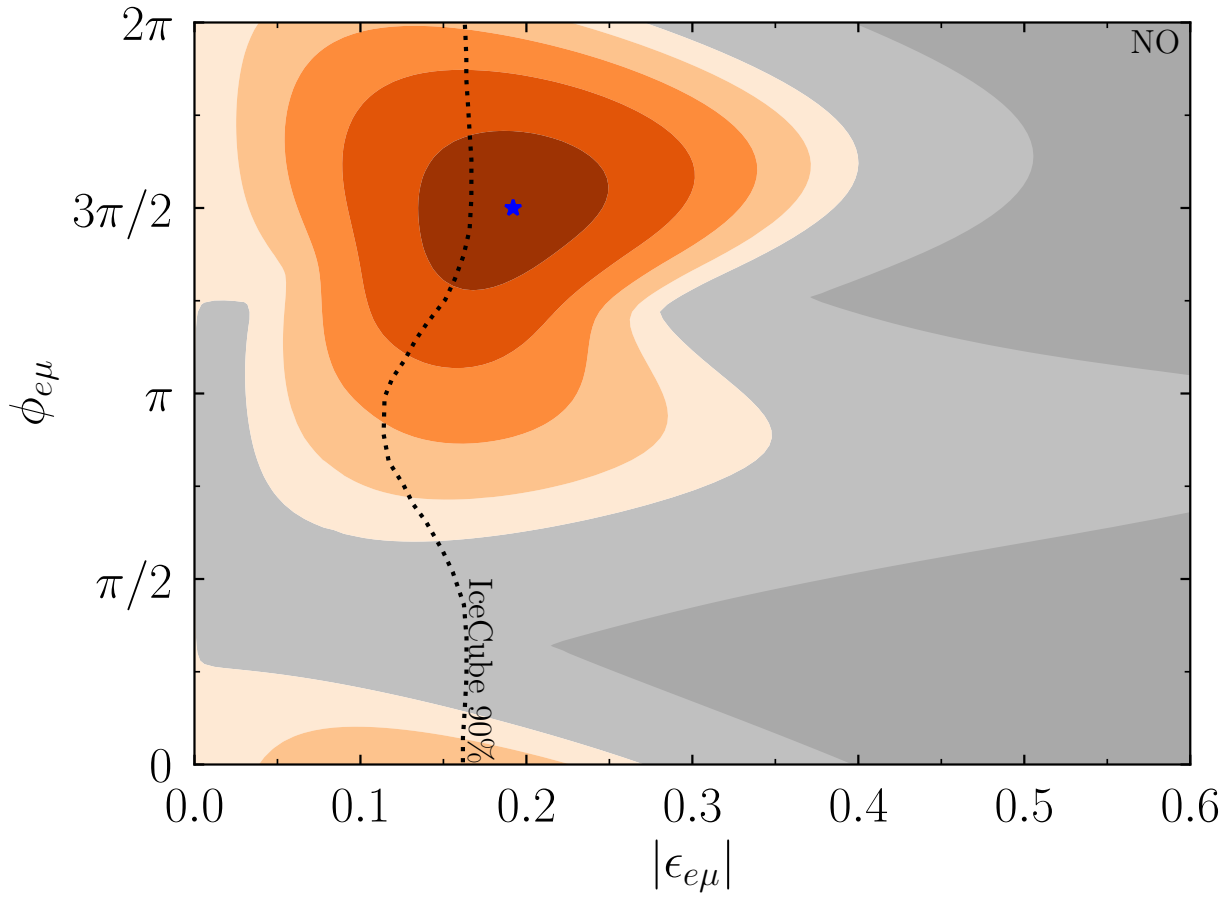


Figure 5.1: The preferred parameter regions for $\epsilon_{e\mu}$ using the newest appearance and disappearance data from NOvA and T2K and assuming the NO. The gray region is disfavored compared to the SM, and the dark gray region is ruled out by NOvA and T2K data at $\Delta\chi^2 \leq -4.61$. The blue star shows the best fit point. Each of the orange contours are drawn at integer values of $\Delta\chi^2$. See Table 5.1 for the best parameters. IceCube disfavors the region to the right of the black dotted curve at 90% [191].

Table 5.1: Best fit values and corresponding $\Delta\chi^2 = \chi^2_{\text{SM}} - \chi^2_{\text{NSI}}$ for a fixed MO, considering one complex NSI parameter at a time. (For the SM, $\chi^2_{\text{NO}} - \chi^2_{\text{IO}} = 2.3$ .)

| MO | NSI | $\lvert\epsilon_{\alpha\beta}\rvert$ | $\phi_{\alpha\beta}/\pi$ | $\delta/\pi$ | $\Delta\chi^2$ |
|---|---|---|---|---|---|
| NO | $\epsilon_{e\mu}$ | 0.19 | 1.50 | 1.46 | 4.44 |
| | $\epsilon_{e\tau}$ | 0.28 | 1.60 | 1.46 | 3.65 |
| | $\epsilon_{\mu\tau}$ | 0.35 | 0.60 | 1.83 | 0.90 |
| IO | $\epsilon_{e\mu}$ | 0.04 | 1.50 | 1.52 | 0.23 |
| | $\epsilon_{e\tau}$ | 0.15 | 1.46 | 1.59 | 0.69 |
| | $\epsilon_{\mu\tau}$ | 0.17 | 0.14 | 1.51 | 1.03 |

### 5.2.4 Results

We analyze one complex NSI parameter at a time, using the appearance and disappearance data from NOvA and T2K and assuming the NO. In Fig. 5.1, we present the allowed parameter regions in the $|\epsilon_{\alpha\beta}|$-$\phi_{\alpha\beta}$ plane for $\epsilon_{e\mu}$. The results for $\epsilon_{e\tau}$ and $\epsilon_{\mu\tau}$ can be found in the supplemental material. For simplicity, we fix $\theta_{13}$, $\theta_{12}$, and $\Delta m^2_{21}$ to the best fit values from Daya Bay and KamLAND as described above, as these experiments are not affected by NSI[6], and marginalize over $\Delta m^2_{31}$, $\delta$, and $\theta_{23}$, including the pull on $\Delta m^2_{31}$ from Daya Bay. We have verified that including the pulls associated with $\theta_{13}$, $\theta_{12}$, and $\Delta m^2_{21}$ do not significantly affect our results. The best fit values for the parameters for each case of $\epsilon_{e\mu}$, $\epsilon_{e\tau}$, and $\epsilon_{\mu\tau}$ in both MOs are given in Table 5.1. Note that while the combination of both experiments raises the $\chi^2$ by about 5.5 as mentioned in the supplemental material, that can be nearly completely alleviated with the addition of $\epsilon_{e\mu}$ which provides an improvement in the test statistic of 4.44 (compare this to switching to the IO which only improves the test statistic by 2.3 and is in tension with SK data). In the presence of NSI, we still find that the upper octant is preferred with $\sin^2\theta_{23} = 0.56$ for all three NSI parameters and both MOs.

Consistent with our analytic estimates, we find moderate evidence for CP-violating NSI. The best solution is with the $\epsilon_{e\mu}$ parameter with maximal CP-violating phases for both the standard CP phase and the new NSI CP phase.

Other oscillation probes of NSI come from atmospheric and solar experiments. As atmospheric constraints are expected to be stronger than those from solar, we focus on those. The constraints on complex NSI parameters from IceCube [191] slightly disfavor the preferred region for $\epsilon_{e\mu}$, although it is possible to get an improved fit to the NOvA and T2K data while not being in too strong of tension with the IceCube data. In fact, the best fit

[6]The slight discrepancy between the determination of the solar mass splitting by KamLAND and SuperK could be resolved by NSI in the Sun [192].

point to the IceCube data for $\epsilon_{e\mu}$ is at $|\epsilon_{e\mu}| = 0.07$ and $\phi_{e\mu}/\pi = 1.91$, close to the relevant numbers for NOvA and T2K. It is also interesting to note that IceCube slightly disfavors $|\epsilon_{e\mu}| = 0$ at just over $1\sigma$.

We show the constraints from IceCube on complex NSI from [191] on Fig. 5.1 and in the supplemental material, which only slightly disfavors this NSI explanation of long-baseline data with $\epsilon_{e\mu}$. The IceCube constraints are comparable to other constraints in the literature on real NSI from oscillation experiments [138, 157, 193]. Constraints on complex off-diagonal NSI from solar measurements are expected to be weak [152].

COHERENT's measurement of the coherent elastic neutrino nucleus scattering (CEvNS) process [194] provides constraints [149, 157, 159, 195–201] on the NSI parameter space that is also an explanation of the NOvA and T2K data. Further constraints come from elastic neutrino electron scattering [202]. While the parameters relevant for NOvA and T2K are not strongly ruled out by scattering experiments yet [197, 203], they can be probed by COHERENT in coming years. It should be noted, however, that the NSI constraint derived from COHERENT only applies to NSI governed by mediators heavier than $\sim$ 10 MeV [157, 204]. Constraints for lower mediator masses down to $\sim$ 1 MeV can by placed with upcoming low-threshold CEvNS experiments at nuclear reactors. Meanwhile, early universe measurements constrain mediators lighter than $\sim$ 5 MeV [205, 206]. Thus we anticipate that COHERENT or future reactor CEvNS experiments should be able to probe the NSI parameters that could explain the NOvA and T2K data in coming years.

### 5.2.5 Discussion

Measuring and understanding CP violation is of the utmost importance in particle physics. Somewhat confusingly, the weak interaction violates CP while the strong interaction seems

to conserve CP. Meanwhile, the quark mass mixing matrix has relatively small CP violation. To better understand the important role that CPV plays in particle physics, we must measure it and understand it in the leptonic sector.

In this manuscript, we have analyzed a new physics explanation for the slight tension in the recent NOvA and T2K data. We performed a fit to the data and showed that this tension can be resolved when introducing complex CP-violating NSI parameters. As an example, we analyzed non-zero $\epsilon_{e\mu},\ \epsilon_{e\tau},\ \epsilon_{\mu\tau}$ one at a time and found that the best fit points for the new complex phases of $\epsilon_{\alpha\beta}$ prefers not only maximal CPV in the new interaction around $3\pi/2$ for $\alpha = e$, but also large CPV in the leptonic mass matrix. These NSI parameters are best constrained (not counting long-baseline experiments) by atmospheric oscillation measurements by Super-KamiokaNDE and IceCube. These measurements rule out the favored parameter region for $\epsilon_{\mu\tau}$, whereas the atmospheric constraints only partially disfavor the preferred regions of $\epsilon_{e\mu}$ and $\epsilon_{e\tau}$. We anticipate that improvements from Super-KamiokaNDE and IceCube can further test this hypothesis in the future[7]. Furthermore, experiments that probe coherent elastic neutrino nucleus scattering will provide strong constraints on NSI parameters of a similar order of magnitude, though they currently only apply to mediators heavier than the $\sim 10$ MeV scale.

The connections between combining experiments, the mass ordering, and NSI lead to this narrative:

1. Without new physics, NOvA and T2K each individually prefer the NO.

2. Their combination, without new physics, slightly prefers the IO over NO, despite #1 above.

[7]Future long-baseline experiments also have improvedsensitivity to the range of NSI parameters considered here [86, 192].

3. When allowing for CPV NSI, the preference is for the new physics in the NO over the standard oscillation picture.

We also point out that JUNO's measurement of the MO, which has almost no dependence on the matter effect, will determine the MO independent of NSI.

We can see clearly from e.g. Eq. (5.9) that in order to measure NSI with long-baseline neutrinos, one needs to either compare two different experiments or use a broad band beam such as that which DUNE will have [62]. If this hint for CPV NSI persists, T2HK will find a similar value for $\delta$ as T2K has, while DUNE should be able to see some evidence for NSI directly.

To summarize, we have shown that the tension of the recent NOvA and T2K data can be resolved in a BSM scenario with the introduction of CP-violating NSI parameters, which can be further probed with near-future experiments. It would be interesting to see if other new physics models could also explain the discrepancy, such as the presence of sterile neutrinos, decoherence, or neutrino decay.

**Acknowledgements**

We acknowledge support from the US Department of Energy under Grant Contract DE-SC0012704. The work presented here that RP did was supported by the U.S. Department of Energy, Office of Science, Office of Workforce Development for Teachers and Scientists, Office of Science Graduate Student Research (SCGSR) program. The SCGSR program is administered by the Oak Ridge Institute for Science and Education (ORISE) for the DOE. ORISE is managed by ORAU under contract number DE-SC0014664. All opinions expressed in this paper are the authors' and do not necessarily reflect the policies and views of DOE, ORAU, or ORISE.

### 5.2.6 Supplemental Material

#### Analytic Derivation

Since the inclusion of NSI allows one, in principle, to exactly map one set of vacuum parameters onto another (see Eq. 9 in the main text), we can write down a system of equations of the form

$$P(\epsilon = 0, \delta_{\text{meas}}) = P(\epsilon, \delta_{\text{true}}) \,, \tag{5.10}$$

$$\bar{P}(\epsilon = 0, \delta_{\text{meas}}) = \bar{P}(\epsilon, \delta_{\text{true}}) \,, \tag{5.11}$$

where we require both neutrino and antineutrino modes are equal for a given experiment. For simplicity, we assume that the effect of NSI is completely absorbed in the CP phase; in principle, the other parameters are also altered by NSI, specifically $\theta_{23}$ and $\Delta m^2_{31}$, but we assume that the impact of NSI on those parameters is small, as will be justified by comparing our analytic and numerical results. Here, $\delta_{\text{meas}}$ is the value of $\delta$ extracted by the experiment when assuming the standard oscillation picture. That is, the LHS represents the probabilities as a function of the parameters extracted, assuming no new physics, while the RHS represents the probabilities in terms of the "true" parameters.

We can use approximate expressions for NSI in long-baseline experiments to determine the relationship among the measured values of $\delta$, the true value of $\delta$, and the magnitude and phase of the NSI. From refs. [153, 166] after some manipulation, we find, for neutrinos and

antineutrinos respectively,

$$-s_{12}c_{12}c_{23}\frac{\pi}{2}\Delta m^2_{21}\sin\delta + a_{\rm NOvA}|\epsilon_{e\beta}|\left[w_\beta s_{23}\cos(\delta+\phi_{e\beta}) - v_\beta c_{23}\frac{\pi}{2}\sin(\delta+\phi_{e\beta})\right] \approx -s_{12}c_{12}c_{23}\frac{\pi}{2}\Delta m^2_{21}\sin\delta_{\rm NOvA}\,, \tag{5.12}$$

$$s_{12}c_{12}c_{23}\frac{\pi}{2}\Delta m^2_{21}\sin\delta - a_{\rm NOvA}|\epsilon_{e\beta}|\left[w_\beta s_{23}\cos(\delta+\phi_{e\beta}) + v_\beta c_{23}\frac{\pi}{2}\sin(\delta+\phi_{e\beta})\right] \approx s_{12}c_{12}c_{23}\frac{\pi}{2}\Delta m^2_{21}\sin\delta_{\rm NOvA}\,, \tag{5.13}$$

where $w_\beta = s_{23}$ ($c_{23}$), $v_\beta = c_{23}$ ($-s_{23}$) for $\beta = \mu$ ($\tau$), and we have assumed that the NO is correct and that both experiments measure the NO. A similar expressions exists for T2K, as well. The fact that the only true phase that appears in these approximations is $\delta + \phi_{e\beta}$ is connected to the concept of phase reduction [153].

From the requirement that the probabilities in the neutrino and antineutrino channel should both be satisfied with the same parameters, one immediately finds that $\sin(\delta+\phi_{e\beta}) = 0$. This means $\delta + \phi_{e\beta} = 0$ or $\pi$ and that either $\cos(\delta+\phi_{e\beta}) = 1$ or $\cos(\delta+\phi_{e\beta}) = -1$, respectively. Plugging this in and subtracting the NOvA and T2K equations, we find

$$|\epsilon_{e\beta}| \approx \frac{s_{12}c_{12}c_{23}\pi\Delta m^2_{21}(\sin\delta_{\rm T2K} - \sin\delta_{\rm NOvA})}{2s_{23}w_\beta(a_{\rm NOvA} - a_{\rm T2K})\cos(\delta+\phi_{e\beta})}\,. \tag{5.14}$$

Given that $a_{\rm NOvA} > a_{\rm T2K}$ and that the data suggests that $\sin\delta_{\rm T2K} < \sin\delta_{\rm NOvA}$, we find that $\cos(\delta+\phi_{e\beta}) = -1$, and thus, $\delta + \phi_{e\beta} = \pi$. In any case, we can write down the general result using absolute values, as shown in Eq. 3 in the main text. We obtain,

$$|\epsilon_{e\beta}| \approx \frac{s_{12}c_{12}c_{23}\pi\Delta m^2_{21}}{2s_{23}w_\beta}\left|\frac{\sin\delta_{\rm T2K} - \sin\delta_{\rm NOvA}}{a_{\rm NOvA} - a_{\rm T2K}}\right| \approx \begin{cases} 0.22 & \text{for } \beta = \mu \\ 0.24 & \text{for } \beta = \tau \end{cases}\,, \tag{5.15}$$

where we plugged in the numbers for the last part which result in NSI values generally

consistent with those from the exact numerical searches.

We can instead divide the NOvA and T2K equations to find

$$\sin\delta \approx \frac{\sin\delta_{\rm NOvA}a_{\rm T2K} - \sin\delta_{\rm T2K}a_{\rm NOvA}}{a_{\rm T2K} - a_{\rm NOvA}}\,. \tag{5.16}$$

Plugging in the numbers, we find that the true value of $\delta$ one would expect is $\sin\delta = -1.7$ (the unphysicality of this is due to our $\theta_{23}$ approximation, but it does not mischaracterize the general features of these approximations). This means that for an NSI explanation of NOvA and T2K, we would expect $\sin\delta = -1$, and T2K would infer $\sin\delta_{\rm T2K}$ slightly larger than $-1$. In addition, the effect of Eq. (5.16) in our situation of $\sin\delta_{\rm T2K} \sim -1$ is somewhat alleviated by changes in $\theta_{23}$ due to NSI which we have not accounted for. Given that we have $\cos(\delta + \phi_{e\beta}) = -1$ in our scenario, in the limit where $a_{\rm T2K} \to 0$, we see from Eq. (5.16) that $\sin\delta \approx \sin\delta_{\rm T2K}$ as expected and that $\delta_{\rm T2K} + \phi_{e\beta} = \pi$, and thus $\phi_{e\beta} = 3\pi/2$, consistent with our numerical results.

All of these results are derived assuming the approximate expressions from ref. [166], that the experiments are at the first oscillation maximum, and that the matter potentials are small relative to $\Delta m^2_{31}$ (for NOvA (T2K) we have $a/\Delta m^2_{31} \approx 1/6$ (1/20)).

**Standard Oscillation Results**

In addition to addressing new physics in the neutrino sector, we also show the preferred regions in the standard oscillation picture in Fig. 5.2. Contours are drawn relative to the best fit point at $\Delta\chi^2 = \chi^2 - \chi^2_{\rm bf} = 4.61$. Note that combining the data sets within the normal mass ordering (NO) raises the minimum $\chi^2$ by $\sim 5.5$ over either experiment individually; this tension can be somewhat alleviated by switching the mass ordering [167, 182]. We show the preferred regions of $\theta_{23}$ and the Jarlskog invariant where $J = s_{12}c_{12}s_{13}c^2_{13}s_{23}c_{23}\sin\delta$ is the

Jarlskog [77], which is a parameterization-independent quantification of CPV in the leptonic mass matrix [168]. Note that the maximum value of the Jarlskog is $1/6\sqrt{3} \approx 0.096$; we are already quite far from maximal CPV in the leptonic sector due primarily to the fact that $\theta_{13}$ is fairly small.

For Fig. 5.2 we include a minimization over the four other standard oscillation parameters and the sign of $\cos\delta$ for the Jarlskog panel. We include priors from KamLAND [169] $\tan^2\theta_{12} = 0.436^{+0.029}_{-0.025}$ and $\Delta m^2_{21} = (7.53 \pm 0.18) \times 10^{-5}$ eV$^2$ as well as from Daya Bay [123] $\sin^2 2\theta_{13} = 0.0856 \pm 0.0029$ and $\Delta m^2_{32} = (2.471^{+0.068}_{-0.070}) \times 10^{-3}$ eV$^2$. We find that the best fit parameters are at $J = -0.0120$, $\delta/\pi = 1.21$, and $\sin^2\theta_{23} = 0.556$ in the NO. In the inverted mass ordering (IO) the best fit parameters are $J = -0.0328$, $\delta/\pi = 1.54$, and $\sin^2\theta_{23} = 0.560$. These are compatible at the $< 1\sigma$ level with the latest global fit to all oscillation experiments [167].

We see that in the NO, while T2K has some significance to disfavor $J = 0$, the inclusion of NOvA data weakens this, making CPV in the standard oscillation picture an important goal for NOvA and T2K [170, 171] in coming years, as well as upcoming long-baseline accelerator neutrino experiments such as DUNE and T2HK [61, 62]. This weakening of the significance in the NO when the experiments are combined emphasizes the slight tension between the experiments.

Similarly to refs. [167, 182], we also find that while NOvA and T2K both individually prefer the NO, the combination shows a slight preference for the IO at $\chi^2_{\text{NO}} - \chi^2_{\text{IO}} = 2.3$. When combined with Super-KamiokaNDE (SK) atmospheric data [172, 173], the best fit mass ordering (MO) remains normal [167, 182][8]. This MO question is of crucial significance beyond just measuring parameters in the SM. It may provide guidance about the structure of neutrino

[8] SK preferred the NO at $\chi^2_{\text{IO}} - \chi^2_{\text{NO}} > 5$, but with their latest data release, the significance dropped to $\sim 3.2$, although it is still enough to prefer the NO in total.

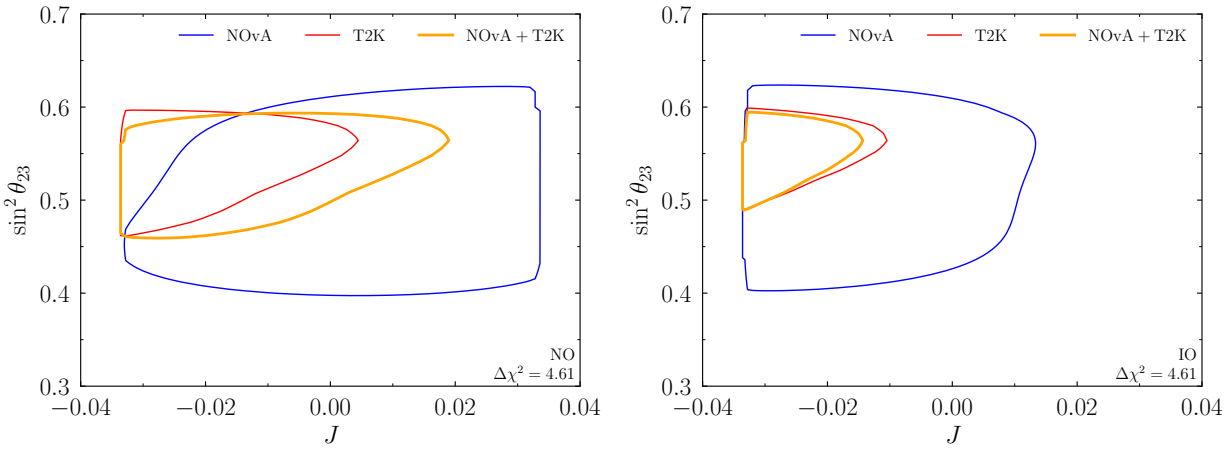


Figure 5.2: The preferred regions in $\sin^2\theta_{23}$-$J$ space for the NO (left) and IO (right) for NOvA data, T2K data, or their combination at $\Delta\chi^2 = 4.61$ within the standard oscillation picture. This includes a marginalization over $\Delta m^2_{21}$, $\Delta m^2_{31}$, $\theta_{13}$, $\theta_{12}$, and the sign of $\cos\delta$ with pulls from KamLAND and Daya Bay.

mass [174] and is a key input for many experimental measurements of neutrinos, including cosmological measurements of neutrino properties, kinematic measurements of neutrinos, and neutrinoless-double-beta decay measurements should neutrinos have a Majorana mass term, see e.g. [175].

We see that in the NO the allowed region for both experiments is larger than that for T2K which highlights the tension between the experiments in the NO. On the other hand, in the IO the allowed region for both experiments is smaller than that for either experiment which shows that both experiments find slightly better agreement in the IO than in the NO.

### Results for $\epsilon_{e\tau}$ and $\epsilon_{\mu\tau}$

We found that $\epsilon_{e\mu}$ explain the data well. We also see in Fig. 5.3 that $\epsilon_{e\tau}$ explains the data fairly well and is comparably allowable by other constraints.

It is expected that $\epsilon_{\mu\tau}$ will not easily address the NOvA and T2K tension. Moreover, there

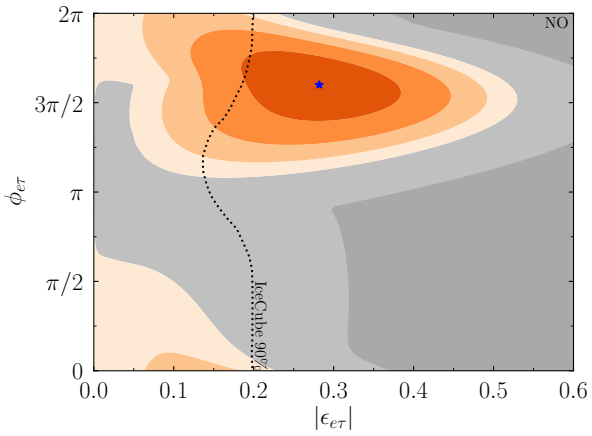


Figure 5.3: The preferred parameter regions for $\epsilon_{e\tau}$ using the newest appearance and disappearance data from NOvA and T2K and assuming the NO. The gray region is disfavored compared to the SM, and the dark gray region is ruled out by NOvA and T2K data at $\Delta\chi^2 \leq -4.61$. The blue star shows the best fit point. Each of the orange contours are drawn at integer values of $\Delta\chi^2$. See the table in the main text (Table 5.1) for the best parameters. IceCube disfavors the region to the right of the black dotted curve at 90% [191].

are very strong constraints on $\epsilon_{\mu\tau}$ from atmospheric data [176, 191, 193]. While these were generally derived under the assumption of real NSI, the relaxation to complex NSI should not significantly weaken the constraints. Nonetheless, we show the preferred region in Fig. 5.4 for NOvA and T2K data while marginalizing over $\theta_{23}$, $\Delta m^2_{31}$ (including a pull from Daya Bay), and $\delta$ while the other three standard oscillation parameters were set to their best fit values from Daya Bay and KamLAND. SK has a bound on $\epsilon_{\mu\tau}$ that is slightly stronger than IceCube's at $\phi_{\mu\tau} = 0, \pi$ [176], since this bound is only valid for CP conserving NSI, and since IceCube thoroughly rules out the regions of parameter space preferred by NOvA and T2K we do not show it on Fig. 5.4.

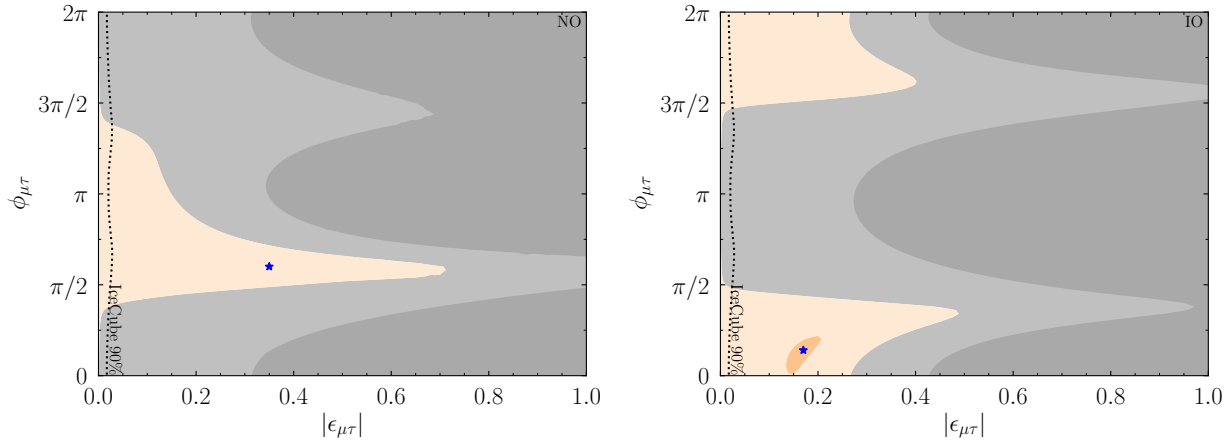


Figure 5.4: The preferred parameter region for $\epsilon_{\mu\tau}$ using the newest appearance and disappearance data from NOvA and T2K and assuming the NO (left) or the IO (right). The gray region is disfavored compared to the SM and the blue star shows the best fit point. The orange contours are drawn at integer values of $\Delta\chi^2$. See the table in the main text (Table 5.1) for the best parameters. IceCube disfavors the region to the right of the black dotted curve at 90% [191].

# Chapter 6

# Conclusions

As the lightest and least known particle of the Standard Model fermions, yet one of the most plentiful fermions in the universe, neutrinos are fascinating to study. In the age of "precision measurements" of neutrinos, neutrino oscillation experiments can be a great probe for testing the foundations of quantum mechanics, for example by observing quantum interference (as shown in Chapter 3), and also for testing Beyond the Standard Model physics scenarios, such as neutrino Non-Standard Interactions (NSIs) (as shown in Chapter 5). If our solution to the T2K-NO$\nu$A tension is correct, the NSI would be another source of $CP$ violation in particle physics. As the last of the standard oscillation parameters are measured, informing us of how much neutrinos violate $CP$ via oscillation, let us not confuse the value of the parameterization-dependent $CP$-violating phase $\delta$ with the amount of $CP$ violation that exists in neutrino oscillations, which is better measured by the Jarlskog invariant (as discussed in Chapter 4). Various unresolved anomalies that have arisen in neutrino physics underscore our need of being extra careful with analyzing all the uncertainties involved in experiments and predictions, including spectral fine structure for neutrinos produced from a nuclear reactor (as discussed in Chapter 2). We showed that this spectral fine structure uncertainty

was particularly important for JUNO, and that the spectrum needs to be determined with an energy resolution that is at least as good as JUNO's, which is now being addressed by the JUNO-TAO proposal [52]. We look forward to discovering the reasons behind the neutrino anomalies and to figuring out what else neutrinos can tell us about physics.

# Bibliography


[1] T. A. Mueller et al., Phys. Rev. C **83**, 054615 (2011).

[2] P. Huber, Phys.Rev. **C84**, 024617 (2011).

[3] C. Jensen, *Controversy and Consensus: Nuclear Beta Decay 1911-1934*, volume 24 of *Science Networks Historical Studies*, Springer Basel AG, 2000.

[4] J. Chadwick, Verh. Phys. Gesell. **16**, 383 (1914).

[5] E. Fermi, Ric. Sci. **4**, 491 (1933).

[6] C. L. Cowan, F. Reines, F. B. Harrison, H. W. Kruse, and A. D. McGuire, Science **124**, 103 (1956).

[7] G. Danby et al., Phys. Rev. Lett. **9**, 36 (1962).

[8] K. Kodama et al., Phys. Lett. B **504**, 218 (2001).

[9] P. Aarnio et al., Phys. Lett. B **231**, 539 (1989).

[10] B. Adeva et al., Phys. Lett. B **237**, 136 (1990).

[11] M. Z. Akrawy et al., Phys. Lett. B **231**, 530 (1989).

[12] D. Decamp et al., Phys. Lett. B **231**, 519 (1989).

[13] M. Tanabashi et al., Phys. Rev. D **98**, 030001 (2018).

[14] B. Pontecorvo, Sov. Phys. JETP **6**, 429 (1957).

[15] Z. Maki, M. Nakagawa, and S. Sakata, Prog. Theor. Phys. **28**, 870 (1962).

[16] L. Wolfenstein, Phys. Rev. D **17**, 2369 (1978).

[17] S. P. Mikheyev and A. Y. Smirnov, Sov. J. Nucl. Phys. **42**, 913 (1985).

[18] P. Huber, M. Lindner, T. Schwetz, M. Rolinec, and W. Winter, Nucl. Phys. B Proc. Suppl. **143**, 565 (2005).

[19] R. Davis, Jr., D. S. Harmer, and K. C. Hoffman, Phys. Rev. Lett. **20**, 1205 (1968).

[20] T. J. Haines et al., Phys. Rev. Lett. **57**, 1986 (1986).

[21] M. Nakahata et al., J. Phys. Soc. Jap. **55**, 3786 (1986).

[22] Y. Fukuda et al., Phys. Rev. Lett. **81**, 1562 (1998).

[23] Q. R. Ahmad et al., Phys. Rev. Lett. **87**, 071301 (2001).

[24] C. Athanassopoulos et al., Phys. Rev. Lett. **75**, 2650 (1995).

[25] A. A. Aguilar-Arevalo et al., Phys. Rev. Lett. **98**, 231801 (2007).

[26] A. A. Aguilar-Arevalo et al., Phys. Rev. Lett. **105**, 181801 (2010).

[27] F. P. An et al., Phys. Rev. Lett. **116**, 061801 (2016), [Erratum: Phys.Rev.Lett. 118, 099902 (2017)].

[28] G. Mention et al., Phys. Rev. **D83**, 073006 (2011).

[29] K. N. Abazajian et al., (2012).

[30] F. An et al., J. Phys. G **43**, 030401 (2016).

[31] C. Patrignani et al., Chin. Phys. **C40**, 100001 (2016).

[32] S. T. Petcov and M. Piai, Phys. Lett. B **533**, 94 (2002).

[33] F. Von Feilitzsch, A. Hahn, and K. Schreckenbach, Phys.Lett. **B118**, 162 (1982).

[34] K. Schreckenbach, G. Colvin, W. Gelletly, and F. Von Feilitzsch, Phys.Lett. **B160**, 325 (1985).

[35] A. Hahn et al., Phys.Lett. **B218**, 365 (1989).

[36] F. P. An et al., (2016).

[37] P. Huber, Nucl. Phys. **B908**, 268 (2016).

[38] A. C. Hayes and P. Vogel, Ann. Rev. Nucl. Part. Sci. **66**, 219 (2016).

[39] M. Fallot et al., Phys. Rev. Lett. **109**, 202504 (2012).

[40] D. A. Dwyer and T. J. Langford, Phys. Rev. Lett. **114**, 012502 (2015).

[41] http://www.oecd-nea.org/dbdata/jeff/#library.

[42] T. R. England and B. Rider, ENDF-349 Evaluation and Compilation of Fission Product Yields: 1993, 1994.

[43] From ENSDF database as of Nov 23, 2013, Version available at http://www.nndc.bnl.gov/ensarchivals/.

[44] E. Ciuffoli et al., Phys. Rev. **D89**, 073006 (2014).

[45] F. Capozzi, E. Lisi, and A. Marrone, Phys. Rev. **D92**, 093011 (2015).

[46] H. Wang, L. Zhan, Y.-F. Li, G. Cao, and S. Chen, (2016).

[47] F. P. An et al., Phys. Rev. Lett. **112**, 061801 (2014).

[48] Y.-F. Li, J. Cao, Y. Wang, and L. Zhan, Phys. Rev. **D88**, 013008 (2013).

[49] F. P. An et al., (2016).

[50] P. Huber, M. Lindner, T. Schwetz, and W. Winter, Nucl. Phys. **B665**, 487 (2003).

[51] X. Qian et al., Phys. Rev. **D87**, 033005 (2013).

[52] A. Abusleme et al., (2020).

[53] J. H. Christenson, J. W. Cronin, V. L. Fitch, and R. Turlay, Phys. Rev. Lett. **13**, 138 (1964).

[54] M. Kobayashi and T. Maskawa, Prog. Theor. Phys. **49**, 652 (1973).

[55] B. Aubert et al., Phys. Rev. Lett. **87**, 091801 (2001).

[56] K. Abe et al., Phys. Rev. Lett. **87**, 091802 (2001).

[57] E. Majorana, Nuovo Cim. **14**, 171 (1937).

[58] K. Abe et al., Nature **580**, 339 (2020), [Erratum: Nature 583, E16 (2020)].

[59] M. A. Acero et al., Phys. Rev. Lett. **123**, 151803 (2019).

[60] M. Jiang et al., PTEP **2019**, 053F01 (2019).

[61] K. Abe et al., PTEP **2015**, 053C02 (2015).

[62] R. Acciarri et al., (2015).

[63] K. Eguchi et al., Phys. Rev. Lett. **90**, 021802 (2003).

[64] Q. R. Ahmad et al., Phys. Rev. Lett. **89**, 011301 (2002).

[65] A. Y. Smirnov, (2006).

[66] E. K. Akhmedov, M. Maltoni, and A. Y. Smirnov, JHEP **06**, 072 (2008).

[67] S. Choubey, S. T. Petcov, and M. Piai, Phys. Rev. D **68**, 113006 (2003).

[68] J. Learned, S. T. Dye, S. Pakvasa, and R. C. Svoboda, Phys. Rev. D **78**, 071302 (2008).

[69] H. Minakata, (2020).

[70] P. Huber, M. Lindner, and W. Winter, Comput. Phys. Commun. **167**, 195 (2005).

[71] P. Huber, J. Kopp, M. Lindner, M. Rolinec, and W. Winter, Comput. Phys. Commun. **177**, 432 (2007).

[72] J. P. A. M. de André, Physics Prospects of JUNO, Presented at the 27th International Workshop on Weak Interactions and Neutrinos in Bari, Italy, 2019.

[73] D. V. Forero, R. Hawkins, and P. Huber, (2017).

[74] S. M. Bilenky, (2012).

[75] A. D. Sakharov, Sov. Phys. Usp. **34**, 392 (1991).

[76] N. Cabibbo, Phys. Rev. Lett. **10**, 531 (1963).

[77] C. Jarlskog, Phys. Rev. Lett. **55**, 1039 (1985).

[78] M. Gonzalez-Garcia, Y. Grossman, A. Gusso, and Y. Nir, Phys. Rev. D **64**, 096006 (2001).

[79] P. Coloma, A. Donini, J. Lopez-Pavon, and H. Minakata, JHEP **08**, 036 (2011).

[80] A. Friedland and I. M. Shoemaker, (2012).

[81] R. Gandhi, B. Kayser, M. Masud, and S. Prakash, JHEP **11**, 039 (2015).

[82] Z. Rahman, A. Dasgupta, and R. Adhikari, J. Phys. G **42**, 065001 (2015).

[83] M. Masud, A. Chatterjee, and P. Mehta, J. Phys. G **43**, 095005 (2016).

[84] A. Palazzo, Phys. Lett. B **757**, 142 (2016).

[85] P. Coloma, JHEP **03**, 016 (2016).

[86] A. de Gouvêa and K. J. Kelly, Nucl. Phys. B **908**, 318 (2016).

[87] M. Masud and P. Mehta, Phys. Rev. D **94**, 013014 (2016).

[88] S. K. Agarwalla, S. S. Chatterjee, and A. Palazzo, JHEP **09**, 016 (2016).

[89] D. Dutta, R. Gandhi, B. Kayser, M. Masud, and S. Prakash, JHEP **11**, 122 (2016).

[90] J. Liao, D. Marfatia, and K. Whisnant, Phys. Rev. D **93**, 093016 (2016).

[91] J. Liao, D. Marfatia, and K. Whisnant, JHEP **01**, 071 (2017).

[92] S.-F. Ge and A. Y. Smirnov, JHEP **10**, 138 (2016).

[93] S. Fukasawa, M. Ghosh, and O. Yasuda, Phys. Rev. D **95**, 055005 (2017).

[94] D. V. Forero and P. Huber, Phys. Rev. Lett. **117**, 031801 (2016).

[95] A. de Gouvêa and K. J. Kelly, (2016).

[96] O. Miranda, M. Tortola, and J. Valle, Phys. Rev. Lett. **117**, 061804 (2016).

[97] S. Choubey, D. Dutta, and D. Pramanik, Phys. Rev. D **96**, 056026 (2017).

[98] K. Deepthi, S. Goswami, and N. Nath, Nucl. Phys. B **936**, 91 (2018).

[99] J. M. Hyde, Nucl. Phys. B **949**, 114804 (2019).

[100] S. Gupta, Z. M. Matthews, P. Sharma, and A. G. Williams, Phys. Rev. D **98**, 035042 (2018).

[101] G. Branco, J. Penedo, P. M. Pereira, M. Rebelo, and J. Silva-Marcos, JHEP **07**, 164 (2020).

[102] P. B. Denton, J. Gehrlein, and R. Pestes, Phys. Rev. Lett. **126**, 051801 (2021).

[103] J. Schechter and J. Valle, Phys. Rev. D **22**, 2227 (1980).

[104] J.-M. Gerard and Z.-z. Xing, Phys. Lett. B **713**, 29 (2012).

[105] H. Fritzsch and Z.-z. Xing, Phys. Lett. B **517**, 363 (2001).

[106] K. M. Merfeld and D. C. Latimer, Phys. Rev. C **90**, 065502 (2014).

[107] D. Boriero, D. J. Schwarz, and H. Velten, Universe **5**, 203 (2019).

[108] A. A. Davydova and K. V. Zhukovsky, Phys. Atom. Nucl. **82**, 281 (2019).

[109] K. V. Zhukovsky and A. A. Davydova, Moscow Univ. Phys. Bull. **74**, 233 (2019).

[110] R. Aleksan, B. Kayser, and D. London, Phys. Rev. Lett. **73**, 18 (1994).

[111] K. Zhukovsky and F. Melazzini, Eur. Phys. J. C **76**, 462 (2016).

[112] D. Emmanuel-Costa, N. R. Agostinho, J. Silva-Marcos, and D. Wegman, Phys. Rev. D **92**, 013012 (2015).

[113] J. Schechter and J. Valle, Phys. Rev. D **23**, 1666 (1981).

[114] W. Rodejohann and J. Valle, Phys. Rev. D **84**, 073011 (2011).

[115] A. Rasin, (1997).

[116] K. Abe et al., A Long Baseline Neutrino Oscillation Experiment Using J-PARC Neutrino Beam and Hyper-Kamiokande, 2014.

[117] B. Abi et al., (2020).

[118] E. Baussan et al., Nucl. Phys. B **885**, 127 (2014).

[119] K. Abe et al., Phys. Rev. Lett. **121**, 171802 (2018).

[120] I. Esteban, M. C. Gonzalez-Garcia, A. Hernandez-Cabezudo, M. Maltoni, and T. Schwetz, JHEP **01**, 106 (2019).

[121] A. de Gouvea et al., Working Group Report: Neutrinos, in *Community Summer Study 2013: Snowmass on the Mississippi*, 2013.

[122] S. Petcov and A. Titov, Phys. Rev. D **97**, 115045 (2018).

[123] D. Adey et al., Phys. Rev. Lett. **121**, 241805 (2018).

[124] S. H. Seo et al., Phys. Rev. D **98**, 012002 (2018).

[125] Y. Abe et al., JHEP **10**, 086 (2014), [Erratum: JHEP 02, 074 (2015)].

[126] P. B. Denton and S. J. Parke, Phys. Rev. D **100**, 053004 (2019).

[127] P. B. Denton, H. Minakata, and S. J. Parke, JHEP **06**, 051 (2016).

[128] P. B. Denton and S. J. Parke, (2018), [Addendum: JHEP 06, 109 (2018)].

[129] A. de Gouvea and H. Murayama, Phys. Lett. B **747**, 479 (2015).

[130] C. A. Argüelles Delgado, J. Salvado, and C. N. Weaver, Comput. Phys. Commun. **196**, 569 (2015).

[131] S. Toshev, Mod. Phys. Lett. A **6**, 455 (1991).

[132] V. D. Barger, S. Pakvasa, T. J. Weiler, and K. Whisnant, Phys. Lett. B **437**, 107 (1998).

[133] P. Harrison, D. Perkins, and W. Scott, Phys. Lett. B **530**, 167 (2002).

[134] Z.-z. Xing, Phys. Lett. B **533**, 85 (2002).

[135] X. G. He and A. Zee, Phys. Lett. B **560**, 87 (2003).

[136] C. H. Albright and W. Rodejohann, Eur. Phys. J. C **62**, 599 (2009).

[137] G. Altarelli and F. Feruglio, Rev. Mod. Phys. **82**, 2701 (2010).

[138] Y. Farzan and M. Tortola, Front. in Phys. **6**, 10 (2018).

[139] *Neutrino Non-Standard Interactions: A Status Report*, volume 2, 2019.

[140] D. V. Forero and W.-C. Huang, JHEP **03**, 018 (2017).

[141] P. B. Denton, Y. Farzan, and I. M. Shoemaker, Phys. Rev. D **99**, 035003 (2019).

[142] U. K. Dey, N. Nath, and S. Sadhukhan, Phys. Rev. D **98**, 055004 (2018).

[143] K. Babu, A. Friedland, P. Machado, and I. Mocioiu, JHEP **12**, 096 (2017).

[144] Y. Farzan and J. Heeck, Phys. Rev. D **94**, 053010 (2016).

[145] Y. Farzan and I. M. Shoemaker, JHEP **07**, 033 (2016).

[146] Y. Farzan, Phys. Lett. B **748**, 311 (2015).

[147] K. Babu, P. B. Dev, S. Jana, and A. Thapa, JHEP **03**, 006 (2020).

[148] S.-F. Ge and S. J. Parke, Phys. Rev. Lett. **122**, 211801 (2019).

[149] D. Aristizabal Sierra, V. De Romeri, and N. Rojas, Phys. Rev. D **98**, 075018 (2018).

[150] I. Bischer and W. Rodejohann, Nucl. Phys. B **947**, 114746 (2019).

[151] K. Babu, G. Chauhan, and P. Bhupal Dev, Phys. Rev. D **101**, 095029 (2020).

[152] O. Miranda, M. Tortola, and J. Valle, JHEP **10**, 008 (2006).

[153] T. Kikuchi, H. Minakata, and S. Uchinami, JHEP **03**, 114 (2009).

[154] S. K. Agarwalla, S. S. Chatterjee, and A. Palazzo, Phys. Lett. B **762**, 64 (2016).

[155] M. Blennow, S. Choubey, T. Ohlsson, D. Pramanik, and S. K. Raut, JHEP **08**, 090 (2016).

[156] K. Deepthi, S. Goswami, and N. Nath, Phys. Rev. D **96**, 075023 (2017).

[157] P. Coloma, P. B. Denton, M. Gonzalez-Garcia, M. Maltoni, and T. Schwetz, JHEP **04**, 116 (2017).

[158] P. Coloma, M. Gonzalez-Garcia, M. Maltoni, and T. Schwetz, Phys. Rev. D **96**, 115007 (2017).

[159] P. Coloma, I. Esteban, M. Gonzalez-Garcia, and M. Maltoni, JHEP **02**, 023 (2020).

[160] I. Esteban, M. Gonzalez-Garcia, and M. Maltoni, JHEP **06**, 055 (2019).

[161] J. Kopp, P. A. Machado, and S. J. Parke, Phys. Rev. D **82**, 113002 (2010).

[162] D. Ayres et al., (2007).

[163] K. Abe et al., Nucl. Instrum. Meth. A **659**, 106 (2011).

[164] P. Dunne, Latest Neutrino Oscillation Results from T2K, 2020.

[165] A. Himmel, New Oscillation Results from the NOvA Experiment, 2020.

[166] F. Capozzi, S. S. Chatterjee, and A. Palazzo, Phys. Rev. Lett. **124**, 111801 (2020).

[167] I. Esteban, M. C. Gonzalez-Garcia, M. Maltoni, T. Schwetz, and A. Zhou, JHEP **09**, 178 (2020).

[168] P. B. Denton and R. Pestes, (2020).

[169] A. Gando et al., Phys. Rev. D **88**, 033001 (2013).

[170] D. Ayres et al., (2004).

[171] Y. Itow et al., The JHF-Kamioka neutrino project, in *3rd Workshop on Neutrino Oscillations and Their Origin (NOON 2001)*, pages 239–248, 2001.

[172] K. Abe et al., Phys. Rev. D **97**, 072001 (2018).

[173] Y. Nakajima, Recent results and future prospects from Super-Kamiokande, 2020.

[174] P. B. Denton, (2020).

[175] S.-F. Ge and J.-y. Zhu, Chin. Phys. C **44**, 083103 (2020).

[176] G. Mitsuka et al., Phys. Rev. D **84**, 113008 (2011).

[177] A. M. Gago, H. Minakata, H. Nunokawa, S. Uchinami, and R. Zukanovich Funchal, JHEP **01**, 049 (2010).

[178] I. Girardi, D. Meloni, and S. Petcov, Nucl. Phys. B **886**, 31 (2014).

[179] M. Gonzalez-Garcia, M. Maltoni, and J. Salvado, JHEP **05**, 075 (2011).

[180] M. Guzzo, A. Masiero, and S. Petcov, Phys. Lett. B **260**, 154 (1991).

[181] N. Ribeiro, H. Minakata, H. Nunokawa, S. Uchinami, and R. Zukanovich-Funchal, JHEP **12**, 002 (2007).

[182] K. J. Kelly, P. A. Machado, S. J. Parke, Y. F. Perez Gonzalez, and R. Zukanovich-Funchal, Phys. Rev. D **103**, 013004 (2021).

[183] M. Baird, Latest Oscillation Results Combining Neutrino and Antineutrino Data from the NOvA Experiment, presented at ICHEP2020, 2020.

[184] H. Yokomakura, K. Kimura, and A. Takamura, Phys. Lett. B **496**, 175 (2000).

[185] K. Kimura, A. Takamura, and H. Yokomakura, Phys. Rev. D **66**, 073005 (2002).

[186] S. K. Agarwalla, Y. Kao, and T. Takeuchi, JHEP **04**, 047 (2014).

[187] H. Minakata and S. J. Parke, JHEP **01**, 180 (2016).

[188] P. B. Denton, S. J. Parke, and X. Zhang, Phys. Rev. D **98**, 033001 (2018).

[189] P. B. Denton, S. J. Parke, and X. Zhang, Phys. Lett. B **807**, 135592 (2020).

[190] Z. Djurcic et al., (2015).

[191] T. Ehrhardt, Search for NSI in neutrino propagationwith IceCube DeepCore, presented at 4th Uppsala workshop on Particle Physics with Neutrino Telescopes (PPNT) , 2019.

[192] J. Liao, D. Marfatia, and K. Whisnant, Phys. Lett. B **771**, 247 (2017).

[193] I. Esteban, M. Gonzalez-Garcia, M. Maltoni, I. Martinez-Soler, and J. Salvado, JHEP **08**, 180 (2018).

[194] D. Z. Freedman, Phys. Rev. **D9**, 1389 (1974).

[195] D. Akimov et al., Science **357**, 1123 (2017).

[196] D. Akimov et al., Phys. Rev. Lett. **126**, 012002 (2021).

[197] P. B. Denton and J. Gehrlein, (2020).

[198] J. Liao and D. Marfatia, Phys. Lett. B **775**, 54 (2017).

[199] O. Miranda et al., JHEP **05**, 130 (2020).

[200] C. Giunti, Phys. Rev. D **101**, 035039 (2020).

[201] D. Papoulias, T. Kosmas, and Y. Kuno, Front. in Phys. **7**, 191 (2019).

[202] A. N. Khan and D. W. McKay, JHEP **07**, 143 (2017).

[203] B. Dutta et al., JHEP **20**, 106 (2020).

[204] P. B. Denton, Y. Farzan, and I. M. Shoemaker, JHEP **07**, 037 (2018).

[205] A. Kamada and H.-B. Yu, Phys. Rev. D **92**, 113004 (2015).

[206] G.-y. Huang, T. Ohlsson, and S. Zhou, Phys. Rev. D **97**, 075009 (2018).

# Appendices

# Appendix A

# Oscillation Probability in Matter

In this appendix, we consider the case of neutrinos traveling through the crust of the Earth, and use perturbation theory to calculate the oscillation probabilities from the matter Hamiltonian $H_{\text{mat}}$, which is shown in matrix form in the mass basis in Eq. (1.16):

$$H^m_{\text{mat}} = \frac{1}{2E}\begin{bmatrix} 0 & 0 & 0 \\ 0 & \Delta m^2_{21} & 0 \\ 0 & 0 & \Delta m^2_{31} \end{bmatrix} + \sqrt{2} G_F N_e U^\dagger \begin{bmatrix} 1 & 0 & 0 \\ 0 & 0 & 0 \\ 0 & 0 & 0 \end{bmatrix} U + \left( \frac{m_1^2}{2E} + V_{NC} \right) I_3 \,.$$

Note that the matrix form of the Hamiltonian in a particular basis is actually related to the Hamiltonian $H$ by $H^\psi_{ab} = \langle \psi_a | \, H \, | \psi_b \rangle$, where $|\psi_i\rangle$ are the eigenstates of the basis and $H^\psi_{ab}$ is the $(a,b)^{\text{th}}$ component of the Hamiltonian matrix in the $\psi$ basis.

The parameterization of the neutrino mixing matrix $U$ used in this appendix is the same as in Eq. (1.9), which assumes unitarity with only three flavors of neutrinos that mix with each

other:

$$U_{\text{PDG}} = \begin{bmatrix} 1 & 0 & 0 \\ 0 & c_{23} & s_{23} \\ 0 & -s_{23} & c_{23} \end{bmatrix} \begin{bmatrix} c_{13} & 0 & s_{13}e^{-i\delta} \\ 0 & 1 & 0 \\ -s_{13}e^{i\delta} & 0 & c_{13} \end{bmatrix} \begin{bmatrix} c_{12} & s_{12} & 0 \\ -s_{12} & c_{12} & 0 \\ 0 & 0 & 1 \end{bmatrix} \equiv U_1 U_2 U_3$$
$$= \begin{bmatrix} c_{12}c_{13} & s_{12}c_{13} & s_{13}e^{-i\delta} \\ -s_{12}c_{23} - c_{12}s_{13}s_{23}e^{i\delta} & c_{12}c_{23} - s_{12}s_{13}s_{23}e^{i\delta} & c_{13}s_{23} \\ s_{12}s_{23} - c_{12}s_{13}c_{23}e^{i\delta} & -c_{12}s_{23} - s_{12}s_{13}c_{23}e^{i\delta} & c_{13}c_{23} \end{bmatrix} \equiv \begin{bmatrix} U_{e1} & U_{e2} & Ue3 \\ U_{\mu 1} & U_{\mu 2} & U\mu 3 \\ U_{\tau 1} & U_{\tau 2} & U\tau 3 \end{bmatrix}.$$

## A.1 Perturbation Set-Up

To set up the perturbation, we need to identify a Hamiltonian $H_0$ with a known solution that is part of the neutrino matter Hamiltonian $H_{\text{mat}}$ and that can be safely assumed to be larger than the rest of $H_{\text{mat}}$. First, we will find assumptions we can safely make, and then we will identify the $H_0$ we will use.

### A.1.1 Assumptions

From experimental measurements, we know that $\Delta m^2_{21} = (7.4 \pm 0.2) \times 10^{-5}\,\text{eV}^2$ and $|\Delta m^2_{31}| = (2.51 \pm 0.03) \times 10^{-3}\,\text{eV}^2$ [167]. So, for the perturbation, we can assume that the ratio of the small to large mass-squared differences is small, or in other words,

$$\epsilon_m \equiv \left| \frac{\Delta m^2_{21}}{\Delta m^2_{31}} \right| = 2.9 \times 10^{-2} \ll 1\,. \tag{A.1}$$

As mentioned in Section 1.2.3, $V_{CC} = \sqrt{2} G_F N_e \equiv \frac{a}{2E}$ is the Wolfenstein matter potential, where $E$ is the energy of the neutrino traveling through the matter. The electron number

density for ordinary matter can be written as

$$N_e = \left(\frac{Y_e}{0.5}\right)\left(\frac{\rho}{2.83\,\mathrm{g/cm^3}}\right)\left(\frac{1.66\times10^{-22}\,\mathrm{g}}{m_n}\right)8.52\times10^{23}\,e^-\,\mathrm{cm^{-3}}\,,$$

where $Y_e$ is the ratio of electrons to nucleons in the matter, $\rho$ is the density of the matter, and $m_n$ is the average mass per nucleon in the matter. For the crust of the Earth, $Y_e$ can be approximated as 0.5 and the density is $2.83\,\mathrm{g/cm^3}$. Thus, the Wolfenstein matter potential in the crust of the Earth is $V_{CC} \approx \sqrt{2}(8.96\times10^{-38}\,\mathrm{eV\,cm^3})(8.52\times10^{23}\,\mathrm{cm^{-3}}) = 1.08\times10^{-13}\,\mathrm{eV}$. So, for our assumption of a small matter potential, we will use

$$\epsilon_a \equiv \frac{2EV_{CC}}{\Delta m^2_{31}} = \frac{E}{1.16\times10^{10}\,\mathrm{eV}} \ll 1\,. \tag{A.2}$$

This means that for this appendix, the neutrino energy needs to satisfy $E \ll 12\,\mathrm{GeV}$.

### A.1.2 The Hamiltonian

The Hamiltonian $H_{\mathrm{mat}}$ (from Eq. (1.16)) in the flavor basis is

$$H^f_{\mathrm{mat}} = \Delta_{31}\left(U\begin{bmatrix}0&0&0\\0&\epsilon_m&0\\0&0&1\end{bmatrix}U^\dagger + \epsilon_a\begin{bmatrix}1&0&0\\0&0&0\\0&0&0\end{bmatrix}\right),$$

where $\Delta_{ij} \equiv \frac{\Delta m^2_{ij}}{2E}$. By rearranging and plugging in $U_{\mathrm{PDG}}$ for $U$, we find

$$H^f_{\mathrm{mat}} = \Delta_{31}U_1U_2\left(\begin{bmatrix}0&0&0\\0&0&0\\0&0&1\end{bmatrix} + \epsilon_m U_3\begin{bmatrix}0&0&0\\0&1&0\\0&0&0\end{bmatrix}U_3^\dagger + \epsilon_a U_2^\dagger\begin{bmatrix}1&0&0\\0&0&0\\0&0&0\end{bmatrix}U_2\right)U_2^\dagger U_1^\dagger\,.$$

**The Hat Basis**

For simplicity, we want to find a basis for which the large term in this equation is a diagonal matrix. So, we will define that basis, which we will call the hat basis, as follows:

$$|\hat{\nu}_i\rangle \equiv (U_1 U_2)_{\alpha i} |\nu_\alpha\rangle \tag{A.3}$$

for $\alpha = e, \mu, \tau$ and $i = 1, 2, 3$. In that basis, the Hamiltonian becomes

$$\begin{aligned}\hat{H}_{\text{mat}} =& U_2^\dagger U_1^\dagger H^f_{\text{mat}} U_1 U_2 \\ =& \Delta_{31} \left( \begin{bmatrix} 0 & 0 & 0 \\ 0 & 0 & 0 \\ 0 & 0 & 1 \end{bmatrix} + \epsilon_m U_3 \begin{bmatrix} 0 & 0 & 0 \\ 0 & 1 & 0 \\ 0 & 0 & 0 \end{bmatrix} U_3^\dagger + \epsilon_a U_2^\dagger \begin{bmatrix} 1 & 0 & 0 \\ 0 & 0 & 0 \\ 0 & 0 & 0 \end{bmatrix} U_2 \right).\end{aligned} \tag{A.4}$$

Thus, we will choose the unperturbed Hamiltonian to be

$$\hat{H}_0 \equiv \begin{bmatrix} 0 & 0 & 0 \\ 0 & 0 & 0 \\ 0 & 0 & \Delta_{31} \end{bmatrix}, \tag{A.5}$$

which leaves

$$\begin{aligned}\hat{H}_1 \equiv& U_3 \begin{bmatrix} 0 & 0 & 0 \\ 0 & \Delta_{21} & 0 \\ 0 & 0 & 0 \end{bmatrix} U_3^\dagger + U_2^\dagger \begin{bmatrix} V_{CC} & 0 & 0 \\ 0 & 0 & 0 \\ 0 & 0 & 0 \end{bmatrix} U_2 \\ =& \begin{bmatrix} s_{12}^2 & s_{12}c_{12} & 0 \\ s_{12}c_{12} & c_{12}^2 & 0 \\ 0 & 0 & 0 \end{bmatrix} \Delta_{21} + \begin{bmatrix} c_{13}^2 & 0 & s_{13}c_{13}e^{-i\delta} \\ 0 & 0 & 0 \\ s_{13}c_{13}e^{i\delta} & 0 & s_{13}^2 \end{bmatrix} V_{CC}\end{aligned} \tag{A.6}$$

as the perturbation Hamiltonian.

## A.2 $S$ Matrix Calculation

The $S$ matrix, also called the oscillation amplitude, is defined to be the matrix such that the probability of the oscillation $\nu_\alpha \to \nu_\beta$ occurring is $P(\nu_\alpha \to \nu_\beta) = |S_{\beta\alpha}|^2$.

**Properties of $S$**

Let $|\tilde{\nu}_i\rangle = A_{\alpha i} |\nu_\alpha\rangle$ $(i = 1, 2, 3)$ for a unitary matrix $A$ and $\tilde{S}_{ji}$ be defined such that $P(\tilde{\nu}_i \to \tilde{\nu}_j) = |S_{ji}|^2$. Then,

$$\tilde{S}_{ji} = \langle \tilde{\nu}_j | \tilde{\nu}_i(t) \rangle = A^*_{\beta j} A_{\alpha i} \langle \nu_\beta | \nu_\alpha(t) \rangle = (A^\dagger S A)_{\beta\alpha} \,. \tag{A.7}$$

This relation holds between any two $S$ matrices for bases related by a unitary matrix.

Now, the eigenstates of the Hamiltonian $H_{\text{mat}}$ (which we will call $|\nu_i^m\rangle$ for $i = 1, 2, 3$) propagate as plane waves, so $|\nu_i^m(t)\rangle = e^{-iH_{\text{mat}}t} |\nu_i^m\rangle = e^{-iE_i^m t} |\nu_i^m\rangle$ (assuming a constant matter density), where $E_i^m$ for $i = 1, 2, 3$ are the eigenvalues of the Hamiltonian $H_{\text{mat}}$. Let $D$ be the matrix that diagonalizes $H^f_{\text{mat}}$, so that

$$D^\dagger H^f_{\text{mat}} D = \begin{bmatrix} E_1^m & 0 & 0 \\ 0 & E_2^m & 0 \\ 0 & 0 & E_3^m \end{bmatrix} \equiv H^d_{\text{mat}} \,,$$

and let $S^d_{kj} \equiv \left\langle \nu_k^m \middle| \nu_j^m(t) \right\rangle$. Then, $S^d_{kj} = \left\langle \nu_k^m \right| e^{-iE_j t} \left| \nu_j^m \right\rangle$ , $\Rightarrow S^d = e^{-iH^d_{\text{mat}} t}$. Thus, for a

constant matter density,

$$\tilde{S} = B^\dagger S^d B = B^\dagger e^{-iH^d_{\rm mat}t} B = e^{-iB^\dagger H^d_{\rm mat} Bt} = e^{-i\tilde{H}t}\,, \tag{A.8}$$

where $B \equiv D^\dagger A$ and $\tilde{H}$ is the Hamiltonian in the $|\tilde{\nu}_i\rangle$ basis. Since $A$ was arbitrary, this is true for any basis. Another way to see this is via the evolution equation for $S$:

$$\begin{aligned}\frac{\partial}{\partial t}\tilde{S}_{mn} &= \langle\tilde{\nu}_m| \frac{\partial}{\partial t} e^{-iH_{\rm mat}t} |\tilde{\nu}_n\rangle \\ &= -i \langle\tilde{\nu}_m| H_{\rm mat} |\tilde{\nu}_l\rangle \langle\tilde{\nu}_l| e^{-iH_{\rm mat}t} |\tilde{\nu}_n\rangle = -i\tilde{H}_{ml}\tilde{S}_{ln}\,,\end{aligned}$$

$$\Rightarrow i\frac{\partial}{\partial t}\tilde{S} = \tilde{H}\tilde{S}\,. \tag{A.9}$$

The solution to the above equation is $\tilde{S} = e^{-i\tilde{H}t}$.

### A.2.1 In the Hat Basis

Let $\hat{S}$ be the oscillation amplitude for the hat basis. Then,

$$\hat{S}(t) = e^{-i\hat{H}t} = e^{-i\left(\hat{H}_0 + \hat{H}_1\right)t}\,. \tag{A.10}$$

Expanding this exponential into an infinite series will not easily yield a series in which each successive term is an order higher in $\hat{H}_1$, so let us use a different function to help us out: $\Omega(t) \equiv e^{i\hat{H}_0 t}\hat{S}(t)$. Then, using the evolution equation for $\hat{S}(t)$ (as found in Eq. (A.9)), we find

$$\begin{aligned}\frac{\partial}{\partial t}\Omega =& i\hat{H}_0\Omega - ie^{i\hat{H}_0 t}\left(\hat{H}_0 + \hat{H}_1\right)\hat{S} \\ =& -ie^{i\hat{H}_0 t}\hat{H}_1\hat{S}\,.\end{aligned}$$

So, the evolution equation for $\Omega(t)$ is

$$e^{i\hat{H}_0 t}\hat{H}_1 e^{-i\hat{H}_0 t}\Omega = i\frac{\mathrm{d}}{\mathrm{d}t}\Omega \equiv H_\Omega \Omega\,. \tag{A.11}$$

The solution to this equation is

$$\begin{aligned}\Omega(t) =& I + (-i)\int_0^t \mathrm{d}t'\, H_\Omega(t') + \frac{(-i)^2}{2!}\int_0^t \mathrm{d}t'\, H_\Omega(t')\int_0^{t'} \mathrm{d}t''\, H_\Omega(t'') + \dots \\ \equiv& \Omega(t)^{(0)} + \Omega(t)^{(1)} + \Omega(t)^{(2)} + \dots\,,\end{aligned} \tag{A.12}$$

so the $S$ matrix in the hat basis is

$$\hat{S}(t) = \sum_{n=0}^{\infty} e^{-i\hat{H}_0 t}\Omega(t)^{(n)} \equiv \sum_{n=0}^{\infty} \hat{S}^{(n)}(t)\,. \tag{A.13}$$

Now,

$$\left(\hat{H}_0\right)^0 = I_3\,,$$

$$\left(\hat{H}_0\right)^1 = \begin{bmatrix} 0 & 0 & 0 \\ 0 & 0 & 0 \\ 0 & 0 & \Delta_{31} \end{bmatrix},\ \left(\hat{H}_0\right)^2 = \begin{bmatrix} 0 & 0 & 0 \\ 0 & 0 & 0 \\ 0 & 0 & \Delta_{31}^2 \end{bmatrix},\ \dots,\ \left(\hat{H}_0\right)^n = \begin{bmatrix} 0 & 0 & 0 \\ 0 & 0 & 0 \\ 0 & 0 & \Delta_{31}^n \end{bmatrix}.$$

So,

$$e^{-i\hat{H}_0 t} = \sum_{n=0}^{\infty} \frac{(-it)^n}{n!}\hat{H}_0^n = \begin{bmatrix} 1 & 0 & 0 \\ 0 & 1 & 0 \\ 0 & 0 & e^{-i\Delta_{31}t} \end{bmatrix}.$$

Plugging this equation into Eq. (A.11) yields

$$\begin{aligned} H_\Omega \equiv & e^{i\hat{H}_0 t}\hat{H}_1 e^{-i\hat{H}_0 t} \\ = & \begin{bmatrix} s_{12}^2 & s_{12}c_{12} & 0 \\ s_{12}c_{12} & c_{12}^2 & 0 \\ 0 & 0 & 0 \end{bmatrix} \Delta_{21} + \begin{bmatrix} c_{13}^2 & 0 & s_{13}c_{13}e^{-i(\delta+\Delta_{31}t)} \\ 0 & 0 & 0 \\ s_{13}c_{13}e^{i(\delta+\Delta_{31}t)} & 0 & s_{13}^2 \end{bmatrix} V_{CC}\,, \end{aligned} \tag{A.14}$$

which, as desired, is on the order of $\hat{H}_1$. So, the series expansion of $\Omega(t)$ in Eq.A.12 is a quickly converging one with $\Omega(t)^{(n)} \sim \mathcal{O}\Big(\Big(\hat{H}_1\Big)^n\Big)$, $\Rightarrow \hat{S}^{(n)} \sim \mathcal{O}\Big(\Big(\hat{H}_1\Big)^n\Big)$. Therefore, $\hat{S}$ to first order in $\epsilon_a$ and $\epsilon_m$ is $\hat{S} = \hat{S}^{(0)} + \hat{S}^{(1)}$. Now, we plug Eq. (A.14) into Eq. (A.12) to find

$$\Omega(t)^{(1)} = -i \begin{bmatrix} s_{12}^2 & s_{12}c_{12} & 0 \\ s_{12}c_{12} & c_{12}^2 & 0 \\ 0 & 0 & 0 \end{bmatrix} \Delta_{21} t - \begin{bmatrix} \frac{ic_{13}^2\Delta_{31}t}{1-e^{-i\Delta_{31}t}} & 0 & s_{13}c_{13}e^{-i\delta} \\ 0 & 0 & 0 \\ s_{13}c_{13}e^{i\delta}e^{i\Delta_{31}t} & 0 & \frac{is_{13}^2\Delta_{31}t}{1-e^{-i\Delta_{31}t}} \end{bmatrix} \big(1 - e^{-i\Delta_{31}t}\big)\epsilon_a\,,$$

which, combined with Eq. (A.13), gives us

$$\hat{S}^{(1)} = -i \begin{bmatrix} s_{12}^2 & s_{12}c_{12} & 0 \\ s_{12}c_{12} & c_{12}^2 & 0 \\ 0 & 0 & 0 \end{bmatrix} \Delta_{21} t - \begin{bmatrix} \frac{ic_{13}^2\Delta_{31}t}{1-e^{-i\Delta_{31}t}} & 0 & s_{13}c_{13}e^{-i\delta} \\ 0 & 0 & 0 \\ s_{13}c_{13}e^{i\delta} & 0 & \frac{is_{13}^2\Delta_{31}t}{e^{i\Delta_{31}t}-1} \end{bmatrix} \big(1 - e^{-i\Delta_{31}t}\big)\epsilon_a\,. \tag{A.15}$$

### A.2.2 In the Flavor Basis

The relation between $S$ and $\hat{S}$ is given by $S = U_1 U_2 \hat{S} U_2^\dagger U_1^\dagger$. So, let $S^{(n)}(t) \equiv U_1 U_2 \hat{S}^{(n)}(t) U_2^\dagger U_1^\dagger$ for all non-negative integer values of $n$. Then,

$$S(t) = \sum_{n=0}^{\infty} S^{(n)}(t)\,,$$

where the first two $S^{(n)}(t)$'s are

$$
\begin{aligned}
S^{(0)} =& U_1 U_2 e^{-i\hat{H}_0 t} U_2^\dagger U_1^\dagger \\
=& \begin{bmatrix} c_{13} & 0 & s_{13}e^{-i\delta} \\ -s_{13}s_{23}e^{i\delta} & c_{23} & c_{13}s_{23} \\ -s_{13}c_{23}e^{i\delta} & -s_{23} & c_{13}c_{23} \end{bmatrix} \begin{bmatrix} 1 & 0 & 0 \\ 0 & 1 & 0 \\ 0 & 0 & e^{-i\Delta_{31}t} \end{bmatrix} \begin{bmatrix} c_{13} & -s_{13}s_{23}e^{-i\delta} & -s_{13}c_{23}e^{-i\delta} \\ 0 & c_{23} & -s_{23} \\ s_{13}e^{i\delta} & c_{13}s_{23} & c_{13}c_{23} \end{bmatrix} \\
=& I_3 - \left(1 - e^{-i\Delta_{31}t}\right) \begin{bmatrix} s_{13}^2 & s_{13}c_{13}s_{23}e^{-i\delta} & s_{13}c_{13}c_{23}e^{-i\delta} \\ s_{13}c_{13}s_{23}e^{i\delta} & c_{13}^2 s_{23}^2 & c_{13}^2 s_{23}c_{23} \\ s_{13}c_{13}c_{23}e^{i\delta} & c_{13}^2 s_{23}c_{23} & c_{13}^2 c_{23}^2 \end{bmatrix}
\end{aligned} \tag{A.16}
$$

and

$$
\begin{aligned}
S^{(1)} =& U_1 U_2 \hat{S}^{(1)} U_2^\dagger U_1^\dagger \\
=& i \begin{bmatrix} -s_{12}^2 c_{13} & -s_{12}c_{12}c_{13} & 0 \\ s_{12}^2 s_{13}s_{23}e^{i\delta} - s_{12}c_{12}c_{23} & s_{12}c_{12}s_{13}s_{23}e^{i\delta} - c_{12}^2 c_{23} & 0 \\ s_{12}^2 s_{13}c_{23}e^{i\delta} + s_{12}c_{12}s_{23} & s_{12}c_{12}s_{13}c_{23}e^{i\delta} + c_{12}^2 s_{23} & 0 \end{bmatrix} \\
& \cdot \begin{bmatrix} c_{13} & -s_{13}s_{23}e^{-i\delta} & -s_{13}c_{23}e^{-i\delta} \\ 0 & c_{23} & -s_{23} \\ s_{13}e^{i\delta} & c_{13}s_{23} & c_{13}c_{23} \end{bmatrix} \Delta_{21} t \\
& + \begin{bmatrix} -c_{13}\left(\frac{ic_{13}^2\Delta_{31}t}{1-e^{-i\Delta_{31}t}} + s_{13}^2\right) & 0 & -s_{13}\left(c_{13}^2 + \frac{is_{13}^2\Delta_{31}t}{e^{i\Delta_{31}t}-1}\right)e^{-i\delta} \\ s_{13}c_{13}^2 s_{23}\left(\frac{i\Delta_{31}t}{1-e^{-i\Delta_{31}t}} - 1\right)e^{i\delta} & 0 & s_{13}^2 c_{13}s_{23}\left(1 - \frac{i\Delta_{31}t}{e^{i\Delta_{31}t}-1}\right) \\ s_{13}c_{13}^2 c_{23}\left(\frac{i\Delta_{31}t}{1-e^{-i\Delta_{31}t}} - 1\right)e^{i\delta} & 0 & s_{13}^2 c_{13}c_{23}\left(1 - \frac{i\Delta_{31}t}{e^{i\Delta_{31}t}-1}\right) \end{bmatrix} \\
& \cdot \begin{bmatrix} c_{13} & -s_{13}s_{23}e^{-i\delta} & -s_{13}c_{23}e^{-i\delta} \\ 0 & c_{23} & -s_{23} \\ s_{13}e^{i\delta} & c_{13}s_{23} & c_{13}c_{23} \end{bmatrix} \left(1 - e^{-i\Delta_{31}t}\right)\epsilon_a \,.
\end{aligned} \tag{A.17}
$$

**$\nu_\mu \to \nu_e$ Channel**

From Eq. (A.16),

$$S^{(0)}_{e\mu} = -s_{13}c_{13}s_{23}e^{-i\delta}\left(1 - e^{-i\Delta_{31}t}\right).$$

From Eq. (A.17),

$$\begin{aligned} S^{(1)}_{e\mu} =& is_{12}c_{13}\Delta_{21}t\left(s_{12}s_{13}s_{23}e^{-i\delta} - c_{12}c_{23}\right) \\ &+ s_{13}c_{13}s_{23}e^{-i\delta}\left[i\left(c^2_{13} - s^2_{13}e^{-i\Delta_{31}t}\right)\Delta_{31}t + \left(s^2_{13} - c^2_{13}\right)\left(1 - e^{-i\Delta_{31}t}\right)\right]\epsilon_a \,. \end{aligned}$$

So, to first order,

$$\begin{aligned} S_{e\mu} =& S^{(0)}_{e\mu} + S^{(1)}_{e\mu} \\ =& \frac{1}{2}\sin(2\theta_{13})s_{23}e^{-i\delta}\left[i\Delta_{31}\epsilon_a t\left(c^2_{13} - s^2_{13}e^{-i\Delta_{31}t}\right) - \left(1 + \cos(2\theta_{13})\epsilon_a\right)\left(1 - e^{-i\Delta_{31}t}\right)\right] \\ &+ is_{12}c_{13}\Delta_{21}t\left(s_{12}s_{13}s_{23}e^{-i\delta} - c_{12}c_{23}\right). \end{aligned}$$

**$\nu_\mu \to \nu_\mu$ Channel**

From Eq. (A.16),

$$S^{(0)}_{\mu\mu} = 1 - c^2_{13}s^2_{23}\left(1 - e^{-i\Delta_{31}t}\right).$$

From Eq. (A.17),

$$\begin{aligned} S^{(1)}_{\mu\mu} =& -i\Delta_{21}t\left[s^2_{12}s^2_{13}s^2_{23} + c^2_{12}c^2_{23} - \frac{1}{2}\sin(2\theta_{12})s_{13}\sin(2\theta_{23})\cos(\delta)\right] \\ &+ s^2_{13}c^2_{13}s^2_{23}\left[2\left(1 - e^{-i\Delta_{31}t}\right) - i\Delta_{31}t\left(1 + e^{-i\Delta_{31}t}\right)\right]\epsilon_a \,. \end{aligned}$$

So, to first order,

$$S_{\mu\mu} = S^{(0)}_{\mu\mu} + S^{(1)}_{\mu\mu} = 1 - c^2_{13}s^2_{23}\left[\left(1 - 2s^2_{13}\epsilon_a\right)\left(1 - e^{-i\Delta_{31}t}\right) + is^2_{13}\Delta_{31}\epsilon_a t\left(1 + e^{-i\Delta_{31}t}\right)\right] - i\Delta_{21}t\left[s^2_{12}s^2_{13}s^2_{23} + c^2_{12}c^2_{23} - \frac{1}{2}\sin(2\theta_{12})s_{13}\sin(2\theta_{23})\cos(\delta)\right].$$

## A.3 Oscillation Probability

For $U_{\text{PDG}}$, we define $J_r \equiv s_{12}c_{12}s_{13}c^2_{13}s_{23}c_{23}$ and $J_{rr} \equiv s_{12}c_{12}s_{13}s_{23}c_{23}$.

### A.3.1 $\nu_\mu \to \nu_e$ Channel

To first order in $\epsilon_a$ and $\epsilon_m$, the oscillation probability for $\nu_\mu \to \nu_e$ is given by

$$\begin{aligned} P(\nu_\mu \to \nu_e) &= |S_{e\mu}|^2 \\ &\approx 2s^2_{13}c^2_{13}s^2_{23}\left[2(1 + 2\cos(2\theta_{13})\epsilon_a)\sin^2\left(\frac{\Delta_{31}}{2}t\right) - \left(\cos(2\theta_{13})\epsilon_a + s^2_{12}\epsilon_m\right)\Delta_{31}t\sin(\Delta_{31}t)\right] \\ &\quad + 2J_r\Delta_{21}t\left(\cos(\delta)\sin(\Delta_{31}t) - 2\sin(\delta)\sin^2\left(\frac{\Delta_{31}}{2}t\right)\right). \end{aligned}$$

### A.3.2 $\nu_\mu \to \nu_\mu$ Channel

To first order in $\epsilon_a$ and $\epsilon_m$, the oscillation probability for $\nu_\mu \to \nu_\mu$ is given by

$$\begin{aligned} P(\nu_\mu \to \nu_\mu) &= |S_{\mu\mu}|^2 \\ &\approx 1 - 4c^2_{13}s^2_{23}\left[1 - c^2_{13}s^2_{23} + 2s^2_{13}\left(2c^2_{13}s^2_{23} - 1\right)\epsilon_a\right]\sin^2\left(\frac{\Delta_{31}}{2}t\right) \\ &\quad + 2c^2_{13}s^2_{23}\left[s^2_{13}\left(2c^2_{13}s^2_{23} - 1\right)\epsilon_a + \left(s^2_{12}s^2_{13}s^2_{23} + c^2_{12}c^2_{23} - 2J_{rr}\cos(\delta)\right)\epsilon_m\right]\Delta_{31}t\sin(\Delta_{31}t). \end{aligned}$$

# Appendix B

# Neutrino Energy Spectrum from a Beam of Pions

## B.1 Off-axis Neutrino Beam Kinematics

(following arXiv:1005.0574v2)

For $\pi \to \mu + \nu_\mu$ decays in the pion's center of mass frame (variables in this frame are labeled with an asterisk),

$$E^*_\mu + E^*_\nu = m_\pi \,, \quad \text{and} \quad p^*_\mu + p^*_\nu = 0 \,,$$

where $E_\mu$ and $E_\nu$ are the energies of the muon and muon neutrino, respectively, $m_\pi$ is the mass of the pion, and $p_\mu$ and $p_\nu$ are the momenta of the muon and muon neutrino, respectively. In the approximation of a massless neutrino ($m_\nu = 0$),

$$p^*_\nu = E^*_\nu = -p^*_\mu \,.$$

From relativity, we know that $E^2 = m^2 + p^2$. So, using conservation of energy, we find

$$E^*_\nu = m_\pi - E^*_\mu = m_\pi - \sqrt{\left(E^*_\nu\right)^2 + m^2_\mu}\,,$$

$$=> E^*_\nu = \frac{\left(m^2_\pi - m^2_\mu\right)}{(2m_\pi)} = 29.8\,\mathrm{MeV}\,, \tag{B.1}$$

where $m_\mu$ is the mass of the muon.

Let the polar axis be the direction of the pion's velocity in the lab frame, and let $\theta^*$ be the angle between the polar axis and the neutrino's velocity in the pion's center of mass frame. Then, the neutrino's momentum in the pion's rest frame is

$$\vec{p^*_\nu} = E^*_\nu \cos(\theta^*)\hat{z} + E^*_\nu \sin(\theta^*)\hat{\rho}\,.$$

Now, the Lorenz transformation equations for energy and momentum are

$$E = \gamma\left(E^* + \beta p^*_\parallel\right), \quad p_\parallel = \gamma\left(p^*_\parallel + \beta E^*\right), \quad \text{and} \quad p_\perp = p^*_\perp\,,$$

where $\beta \equiv \frac{p_\pi}{E_\pi} = \frac{\sqrt{E^2_\pi - m^2_\pi}}{E_\pi}$ and $\gamma \equiv \frac{1}{\sqrt{1-\beta^2}} = \frac{E_\pi}{\sqrt{E^2_\pi - p^2_\pi}} = \frac{E_\pi}{m_\pi}$. So, the neutrino's energy and momentum in the lab frame are

$$\vec{p}_\nu = \gamma E^*_\nu(\cos(\theta^*) + \beta)\hat{z} + E^*_\nu \sin(\theta^*)\hat{\rho} \equiv E_\nu \cos(\theta)\hat{z} + E_\nu \sin(\theta)\hat{\rho}\,, \tag{B.2}$$

and

$$E_\nu = \gamma E^*_\nu(1 + \beta\cos(\theta^*))\,. \tag{B.3}$$

## B.2 Relationship Between $E_\nu$, $E_\pi$, and $\theta$ for a Single Pion Decay

Let $\xi_\pi \equiv \frac{m_\pi}{E_\pi} = \frac{1}{\gamma} = \sqrt{1-\beta^2}$. From Eqs. (B.2) and (B.3), we find $\sin(\theta^*) = \frac{E_\nu}{E_\nu^*}\sin(\theta)$, and

$$\begin{aligned}
&\beta + \cos(\theta^*) = (1 + \beta\cos(\theta^*))\cos(\theta)\,, \\
&\Rightarrow \cos(\theta) = \frac{\beta + \cos(\theta^*)}{1 + \beta\cos(\theta^*)} \qquad \text{and} \qquad \cos(\theta^*) = \frac{\cos(\theta) - \beta}{1 - \beta\cos(\theta)} \\
&\qquad\quad = \frac{E_\pi\cos(\theta^*) + \sqrt{E_\pi^2 - m_\pi^2}}{E_\pi + \cos(\theta^*)\sqrt{E_\pi^2 - m_\pi^2}} \qquad\qquad = \frac{\cos(\theta) - \sqrt{1-\xi_\pi^2}}{1 - \cos(\theta)\sqrt{1-\xi_\pi^2}}\,.
\end{aligned} \tag{B.4}$$

Plugging the second expression in Eq. (B.4) into Eq. (B.3) yields

$$\begin{aligned}
E_\nu =& \frac{E_\nu^*}{\xi_\pi}\left(1 + \frac{\cos(\theta) - \sqrt{1-\xi_\pi^2}}{1 - \cos(\theta)\sqrt{1-\xi_\pi^2}}\sqrt{1-\xi_\pi^2}\right) \\
=& \frac{E_\nu^*\xi_\pi}{1 - \cos(\theta)\sqrt{1-\xi_\pi^2}} = \frac{E_\nu^* m_\pi}{E_\pi - \cos(\theta)\sqrt{E_\pi^2 - m_\pi^2}}\,.
\end{aligned} \tag{B.5}$$

The plot of this function is shown in Fig. B.1 for various values of $\cos(\theta)$. Notice that the neutrino energy is only greater than $E_\nu^*$ if $\cos(\theta) > 0$, and only in that case (while $E_\nu \geq E_\nu^*$, except for $\theta = 0$) are there multiple (2 to be exact) values of $E_\pi$ for each value of $E_\nu$.

Rearranging equation B.5, we find

$$E_\nu E_\pi - E_\nu\cos(\theta)\sqrt{E_\pi^2 - m_\pi^2}) = E_\nu^* m_\pi$$

$$\Rightarrow \begin{cases} E_\pi = \frac{m_\pi\left(\xi_\nu^2+1\right)}{2\xi_\nu} & \text{for } \cos(\theta) = \pm 1 \\ \left|E_\pi - \frac{m_\pi\xi_\nu}{\sin^2(\theta)}\right| = \frac{m_\pi|\cos(\theta)|\sqrt{\xi_\nu^2 - \sin^2(\theta)}}{\sin^2(\theta)} & \text{otherwise} \end{cases},$$

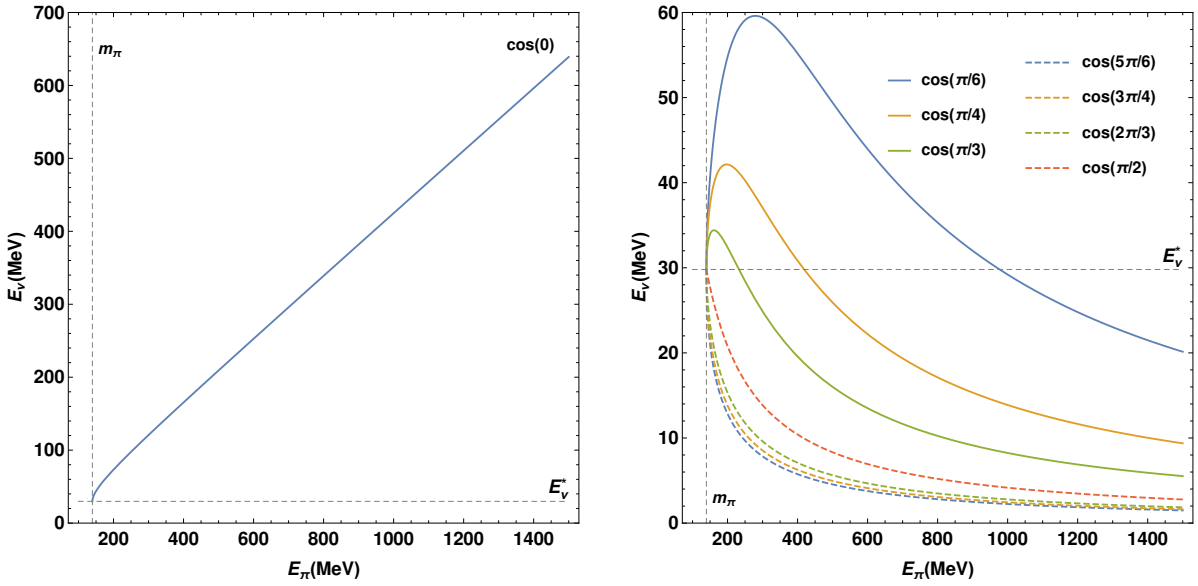


Figure B.1: Neutrino energy versus pion energy for a neutrino from a pion beam. The neutrino is assumed to be traveling 1) in the same direction as the pion (left) or 2) with different angles from the direction in which the pion is traveling (right; curves labeled with cosine of those angles).

where $\xi_\nu \equiv \frac{E_\nu^*}{E_\nu}$. Now, from equation B.5,

$$E_\pi - \frac{m_\pi \xi_\nu}{\sin^2(\theta)} = \frac{-E_\pi \cos^2(\theta) + \cos(\theta)\sqrt{E_\pi^2 - m_\pi^2}}{\sin^2(\theta)}$$

So, for $-1 < \cos(\theta) \leq 0$, $E_\pi - \frac{m_\pi \xi_\nu}{\sin^2(\theta)} \leq 0$, and for $0 < \cos(\theta) < 1$,

$$E_\nu < E_\nu^* \Rightarrow \xi_\nu > 1 \Rightarrow E_\pi - \cos(\theta)\sqrt{E_\pi^2 - m_\pi^2} > m_\pi$$
$$\Rightarrow \left| E_\pi - \frac{m_\pi}{\sin^2(\theta)} \right| > \sqrt{\frac{m_\pi^2\left(1 - \sin^2(\theta)(1 + \cos^2(\theta))\right)}{\sin^4(\theta)}} = \frac{m_\pi \cos^2(\theta)}{\sin^2(\theta)}.$$

So, since $E_\pi \geq m_\pi$, the above inequality implies

$$E_\pi > \frac{m_\pi(1 + \cos^2(\theta))}{\sin^2(\theta)}.$$

Also for $0 < \cos(\theta) < 1$,

$$E_\pi - \frac{m_\pi \xi_\nu}{\sin^2(\theta)} \leq 0 \Rightarrow - E_\pi \cos(\theta) + \sqrt{E_\pi^2 - m_\pi^2} \leq 0$$
$$\Rightarrow E_\pi \leq \frac{m_\pi}{\sin(\theta)} = \frac{m_\pi \sin(\theta)}{\sin^2(\theta)} < \frac{m_\pi(1+\cos^2(\theta))}{\sin^2(\theta)} .$$

So, $E_\pi - \frac{m_\pi \xi_\nu}{\sin^2(\theta)} > 0$ for $\xi_\nu > 1$ when $0 < \cos(\theta) < 1$. Thus,

$$E_\pi - \frac{m_\pi \xi_\nu}{\sin^2(\theta)} = \begin{cases} \frac{m_\pi |\cos(\theta)| \sqrt{\xi_\nu^2 - \sin^2(\theta)}}{\sin^2(\theta)} & \text{for } \xi_\nu > 1 \text{ and } 0 < \cos(\theta) < 1 \\ \frac{-m_\pi |\cos(\theta)| \sqrt{\xi_\nu^2 - \sin^2(\theta)}}{\sin^2(\theta)} & \text{for } -1 < \cos(\theta) \leq 0 \\ \frac{\pm m_\pi |\cos(\theta)| \sqrt{\xi_\nu^2 - \sin^2(\theta)}}{\sin^2(\theta)} & \text{for } \xi_\nu \leq 1 \text{ and } 0 < \cos(\theta) < 1 \end{cases} ,$$

$$\Rightarrow E_\pi = \begin{cases} \frac{m_\pi \left(\xi_\nu^2 + 1\right)}{2\xi_\nu} & \text{for } \cos(\theta) = \pm 1 \\ \frac{m_\pi \left(\xi_\nu \pm \cos(\theta) \sqrt{\xi_\nu^2 - \sin^2(\theta)}\right)}{\sin^2(\theta)} & \text{for } \xi_\nu \leq 1 \text{ and } 0 < \cos(\theta) < 1 \\ \frac{m_\pi \left(\xi_\nu + \cos(\theta) \sqrt{\xi_\nu^2 - \sin^2(\theta)}\right)}{\sin^2(\theta)} & \text{otherwise} \end{cases} .$$

So,

$$\beta = \sqrt{1 - \left(\frac{m_\pi}{E_\pi}\right)^2} = \begin{cases} \frac{\cos(\theta)\left(1 - \xi_\nu^2\right)}{\xi_\nu^2 + 1} & \text{for } \cos(\theta) = \pm 1 \\ \frac{\xi_\nu \cos(\theta) \pm \sqrt{\xi_\nu^2 - \sin^2(\theta)}}{\xi_\nu \pm \cos(\theta) \sqrt{\xi_\nu^2 - \sin^2(\theta)}} & \text{for } \xi_\nu \leq 1 \text{ and } 0 < \cos(\theta) < 1 \\ \frac{\xi_\nu \cos(\theta) + \sqrt{\xi_\nu^2 - \sin^2(\theta)}}{\xi_\nu + \cos(\theta) \sqrt{\xi_\nu^2 - \sin^2(\theta)}} & \text{otherwise} \end{cases} ,$$

$$\Rightarrow \cos(\theta^*) = \frac{\cos(\theta) - \beta}{1 - \beta \cos(\theta)} = \begin{cases} \cos(\theta) & \text{for } \cos(\theta) = \pm 1 \\ \frac{\mp 1}{E_\nu^*} \sqrt{\left(E_\nu^*\right)^2 - E_\nu^2 \sin^2(\theta)} & \text{for } \xi_\nu \leq 1 \text{ and } 0 < \cos(\theta) < 1 \\ \frac{-1}{E_\nu^*} \sqrt{\left(E_\nu^*\right)^2 - E_\nu^2 \sin^2(\theta)} & \text{otherwise} \end{cases} .$$

## B.3 Joint Probability Density Function of $E_\nu$ and $\theta$ Given a Gaussian $E_\pi$ Distribution

In the pion center of mass frame, there is a uniform probability that the decay products from a single pion decay would go in any direction in three dimensions, so the probability density of $\cos(\theta^*)$ is

$$f_{\theta^*}(\cos(\theta^*)) = \frac{1}{2} \text{ for } -1 \leq \cos(\theta^*) \leq 1\,.$$

Assuming the distribution of $E_\pi$ is a gaussian (i.e. the probability density function for $E_\pi$ is

$$f_\pi(E_\pi) = \frac{1}{\sqrt{2\pi\sigma_\pi^2}} e^{-\frac{(E_\pi - \bar{E}_\pi)^2}{2\sigma_\pi^2}}\,,$$

where $\bar{E}_\pi$ and $\sigma_\pi$ are the mean and standard deviation of the energy of the pions in the beam, respectively),the probability of a neutrino from the pion beam source being detected at an off-axis angle $\theta_0$ with an energy $E_{\nu 0}$ (i.e. $\xi_\nu = \xi_{\nu 0} \equiv \frac{E_\nu^*}{E_{\nu 0}}$) in the lab frame is

$$\begin{aligned}
&P\left(E_\nu = E_{\nu 0} \cap \cos(\theta) = \cos(\theta_0)\right) \\
&= \sum_{\substack{E_{\pi 0}, \cos\left(\theta_0^*\right) \\ \text{corresponding} \\ \text{to } E_{\nu 0}, \cos(\theta_0)}} P(E_\pi = E_{\pi 0}) P(\cos(\theta^*) = \cos(\theta_0^*)) \\
&= \begin{cases}
P\left(E_\pi = \frac{m_\pi\left(\xi_{\nu 0}^2 + 1\right)}{2\xi_{\nu 0}}\right) P(\cos(\theta^*) = \pm 1) & \text{for } \cos(\theta) = \pm 1 \\
\sum\limits_{k=\pm 1} P\left(\frac{E_\pi}{m_\pi} = \frac{\xi_{\nu 0} + k\cos(\theta_0)\sqrt{\xi_{\nu 0}^2 - \sin^2(\theta_0)}}{\sin^2(\theta_0)}\right) P\left(\cos(\theta^*) = \frac{-k\sqrt{(E_\nu^*)^2 - E_{\nu 0}^2 \sin^2(\theta_0)}}{E_\nu^*}\right) & \text{for } \substack{\sin(\theta) < \xi_\nu \leq 1 \\ \text{and} \\ 0 < \cos(\theta) < 1} \\
P\left(E_\pi = \frac{m_\pi\left(\xi_{\nu 0} + \cos(\theta_0)\sqrt{\xi_{\nu 0}^2 - \sin^2(\theta_0)}\right)}{\sin^2(\theta_0)}\right) P\left(\cos(\theta^*) = \frac{-\sqrt{(E_\nu^*)^2 - E_{\nu 0}^2 \sin^2(\theta_0)}}{E_\nu^*}\right) & \text{otherwise}
\end{cases} \\
&\equiv f_{\nu,\theta}(E_{\nu 0}, \cos(\theta_0))\, \mathrm{d}E_\nu\, \mathrm{d}(\cos(\theta))
\end{aligned}$$

Now,

$$P(E_\pi = \alpha_E)P(\cos(\theta^*) = \alpha_c) = f_\pi(\alpha_E) f_{\theta^*}(\alpha_c)\,\mathrm{d}E_\pi\,\mathrm{d}(\cos(\theta^*)) = \frac{1}{\sigma_\pi\sqrt{8\pi}} e^{-\frac{(\alpha_E-\bar{E}_\pi)^2}{2\sigma_\pi^2}} \left| \begin{matrix} \frac{\partial E_\pi}{\partial E_\nu} & \frac{\partial E_\pi}{\partial \cos(\theta)} \\ \frac{\partial \cos(\theta^*)}{\partial E_\nu} & \frac{\partial \cos(\theta^*)}{\partial \cos(\theta)} \end{matrix} \right|_{E_\pi=\alpha_E,\theta^*=\alpha_\theta} \mathrm{d}E_\nu\,\mathrm{d}\cos(\theta)\ ,$$

where $\left| \begin{matrix} \frac{\partial E_\pi}{\partial E_\nu} & \frac{\partial E_\pi}{\partial \cos(\theta)} \\ \frac{\partial \cos(\theta^*)}{\partial E_\nu} & \frac{\partial \cos(\theta^*)}{\partial \cos(\theta)} \end{matrix} \right|$ is the Jacobian for this transformation of variables (absolute value of the determinate of this matrix). Also,

$$\frac{\partial E_\pi}{\partial E_\nu} = \frac{\partial E_\pi}{\partial \xi_\nu}\frac{\partial \xi_\nu}{\partial E_\nu} = \frac{-\xi_\nu^2}{E_\nu^*} \begin{cases} \frac{m_\pi\left(\xi_\nu^2-1\right)}{2\xi_\nu^2} & \text{for } \cos(\theta) = \pm 1 \\ \frac{\pm m_\pi\left(\xi_\nu\cos(\theta)\pm\sqrt{\xi_\nu^2-\sin^2(\theta)}\right)}{\sin^2(\theta)\sqrt{\xi_\nu^2-\sin^2(\theta)}} & \text{for } \xi_\nu \le 1 \text{ and } 0 < \cos(\theta) < 1 \\ \frac{m_\pi\left(\xi_\nu\cos(\theta)+\sqrt{\xi_\nu^2-\sin^2(\theta)}\right)}{\sin^2(\theta)\sqrt{\xi_\nu^2-\sin^2(\theta)}} & \text{otherwise} \end{cases}$$

$$\frac{\partial E_\pi}{\partial \cos(\theta)} = m_\pi \begin{cases} \frac{-\cos(\theta)\left(1-\xi_\nu^2\right)^2}{4\xi_\nu^3} & \text{for } \cos(\theta) = \pm 1 \\ \pm\frac{\left(\xi_\nu\cos(\theta)\pm\sqrt{\xi_\nu^2-\sin^2(\theta)}\right)^2}{\sin^4(\theta)\sqrt{\xi_\nu^2-\sin^2(\theta)}} & \text{for } \begin{smallmatrix}\xi_\nu\le 1 \text{ and} \\ 0<\cos(\theta)<1\end{smallmatrix} \\ \frac{\left(\xi_\nu\cos(\theta)+\sqrt{\xi_\nu^2-\sin^2(\theta)}\right)^2}{\sin^4(\theta)\sqrt{\xi_\nu^2-\sin^2(\theta)}} & \text{otherwise} \end{cases},$$

$$\frac{\partial \cos(\theta^*)}{\partial E_\nu} = \begin{cases} 0 & \text{for } \cos(\theta) = \pm 1 \\ \frac{\pm\sin^2(\theta))}{E_\nu^*\sqrt{\xi_\nu^2-\sin^2(\theta)}} & \text{for } \xi_\nu \le 1 \text{ and } 0 < \cos(\theta) < 1 \\ \frac{\sin^2(\theta)}{E_\nu^*\sqrt{\xi_\nu^2-\sin^2(\theta)}} & \text{otherwise} \end{cases},$$

and

$$\frac{\partial\cos(\theta^*)}{\partial\cos(\theta)} = \begin{cases} \frac{1}{\xi_\nu^2} & \text{for } \cos(\theta) = \pm 1 \\ \frac{\mp\cos(\theta)}{\xi_\nu\sqrt{\xi_\nu^2-\sin^2(\theta)}} & \text{for } \xi_\nu \leq 1 \text{ and } 0 < \cos(\theta) < 1 \\ \frac{-\cos(\theta)}{\xi_\nu\sqrt{\xi_\nu^2-\sin^2(\theta)}} & \text{otherwise} \end{cases} .$$

So,

$$\det\begin{pmatrix} \frac{\partial E_\pi}{\partial E_\nu} & \frac{\partial E_\pi}{\partial\cos(\theta)} \\ \frac{\partial\cos(\theta^*)}{\partial E_\nu} & \frac{\partial\cos(\theta^*)}{\partial\cos(\theta)} \end{pmatrix}$$

$$= \frac{-\xi_\nu^2 m_\pi}{E_\nu^*} \begin{cases} \frac{\left(\xi_\nu^2-1\right)}{2\xi_\nu^2}\left(\frac{1}{\xi_\nu^2}\right) & \text{for } \cos(\theta) = \pm 1 \\ \frac{\pm\left(\xi_\nu\cos(\theta)\pm\sqrt{\xi_\nu^2-\sin^2(\theta)}\right)}{\sin^2(\theta)\sqrt{\xi_\nu^2-\sin^2(\theta)}}\left(\frac{\mp\cos(\theta)}{\xi_\nu\sqrt{\xi_\nu^2-\sin^2(\theta)}}\right) & \text{for } \substack{\xi_\nu\leq 1 \text{ and} \\ 0<\cos(\theta)<1} \\ \frac{\left(\xi_\nu\cos(\theta)+\sqrt{\xi_\nu^2-\sin^2(\theta)}\right)}{\sin^2(\theta)\sqrt{\xi_\nu^2-\sin^2(\theta)}}\left(\frac{-\cos(\theta)}{\xi_\nu\sqrt{\xi_\nu^2-\sin^2(\theta)}}\right) & \text{otherwise} \end{cases}$$

$$- m_\pi \begin{cases} 0 & \text{for } \cos(\theta) = \pm 1 \\ \frac{\pm\left(\xi_\nu\cos(\theta)\pm\sqrt{\xi_\nu^2-\sin^2(\theta)}\right)^2}{\sin^4(\theta)\sqrt{\xi_\nu^2-\sin^2(\theta)}}\left(\frac{\pm\sin^2(\theta)}{E_\nu^*\sqrt{\xi_\nu^2-\sin^2(\theta)}}\right) & \text{for } \substack{\xi_\nu\leq 1 \text{ and} \\ 0<\cos(\theta)<1} \\ \frac{\left(\xi_\nu\cos(\theta)+\sqrt{\xi_\nu^2-\sin^2(\theta)}\right)^2}{\sin^4(\theta)\sqrt{\xi_\nu^2-\sin^2(\theta)}}\left(\frac{\sin^2(\theta)}{E_\nu^*\sqrt{\xi_\nu^2-\sin^2(\theta)}}\right) & \text{otherwise} \end{cases} ,$$

$$\Rightarrow \left|\begin{matrix} \frac{\partial E_\pi}{\partial E_\nu} & \frac{\partial E_\pi}{\partial\cos(\theta)} \\ \frac{\partial\cos(\theta^*)}{\partial E_\nu} & \frac{\partial\cos(\theta^*)}{\partial\cos(\theta)} \end{matrix}\right| = \frac{m_\pi}{E_\nu^*} \begin{cases} \frac{\cos(\theta)\left(1-\xi_\nu^2\right)}{2\xi_\nu^2} & \text{for } \cos(\theta) = \pm 1 \\ \frac{\xi_\nu\cos(\theta)\pm\sqrt{\xi_\nu^2-\sin^2(\theta)}}{\sin^2(\theta)\sqrt{\xi_\nu^2-\sin^2(\theta)}} & \text{for } \substack{\xi_\nu\leq 1 \text{ and} \\ 0<\cos(\theta)<1} \\ \frac{\xi_\nu\cos(\theta)+\sqrt{\xi_\nu^2-\sin^2(\theta)}}{\sin^2(\theta)\sqrt{\xi_\nu^2-\sin^2(\theta)}} & \text{otherwise} \end{cases} .$$

Thus, the joint probability density function for neutrino energy $E_\nu$ and off-axis angle $\theta$ is

$$f_{\nu,\theta}(E_\nu,\theta) = \frac{1}{s_\pi k}\begin{cases} \frac{\cos(\theta)\left(\eta_\nu^2-1\right)}{2} e^{-\frac{\left(1+\eta_\nu^2-2\bar{\gamma}\eta_\nu\right)^2}{8\eta_\nu^2 s_\pi^2}} & \text{for } \cos(\theta)=\pm 1 \\ \frac{\cos(\theta)+\sqrt{1-\eta_\nu^2\sin^2(\theta)}}{\sin^2(\theta)\sqrt{1-\eta_\nu^2\sin^2(\theta)}} e^{-\frac{\left(1+\cos(\theta)\sqrt{1-\eta_\nu^2\sin^2(\theta)}-\bar{\gamma}\eta_\nu\sin^2(\theta)\right)^2}{2\eta_\nu^2 s_\pi^2\sin^4(\theta)}} & \\ \quad + \frac{\cos(\theta)-\sqrt{1-\eta_\nu^2\sin^2(\theta)}}{\sin^2(\theta)\sqrt{1-\eta_\nu^2\sin^2(\theta)}} e^{-\frac{\left(1-\cos(\theta)\sqrt{1-\eta_\nu^2\sin^2(\theta)}-\bar{\gamma}\eta_\nu\sin^2(\theta)\right)^2}{2\eta_\nu^2 s_\pi^2\sin^4(\theta)}} & \text{for } \begin{smallmatrix}\eta_\nu\geq 1 \text{ and} \\ 0<\cos(\theta)<1\end{smallmatrix} \\ \frac{\cos(\theta)+\sqrt{1-\eta_\nu^2\sin^2(\theta)}}{\sin^2(\theta)\sqrt{1-\eta_\nu^2\sin^2(\theta)}} e^{-\frac{\left(1+\cos(\theta)\sqrt{1-\eta_\nu^2\sin^2(\theta)}-\bar{\gamma}\eta_\nu\sin^2(\theta)\right)^2}{2\eta_\nu^2 s_\pi^2\sin^4(\theta)}} & \text{otherwise} \end{cases}, \tag{B.6}$$

where $\eta_\nu \equiv \frac{E_\nu}{E_\nu^*} = \frac{1}{\xi_\nu}$, $s_\pi \equiv \frac{\sigma_\pi}{m_\pi}$, $\bar{\gamma} \equiv \frac{\bar{E}_\pi}{m_\pi}$, and $k \equiv E_\nu^*\sqrt{8\pi} = 149\,\text{MeV}$. This result (once integrated according to equation B.7) is consistent with a Monte Carlo simulation done for $10^6$ pion decays, as shown in Fig. B.2.

## B.4 Gaussian Approximation for Neutrino Energy Distribution

The energy distribution ($f_E(E_\nu,\theta_0)$) for the fraction of neutrinos from a pion beam that are in line to go to a detector centered at a given off-axis angle $\theta_0$, spanning $\frac{\phi(\theta)}{2\pi}$ of the space of azimuthal angles (at each value of $\theta$ covered by the detector) and $\frac{\Delta\theta_1+\Delta\theta_2}{\pi}$ of the off-axis angles, is given by

$$\frac{\Phi_i(\theta_0)}{\Phi_{\text{total}}} = \frac{1}{2\pi}\int_{E_i-\Delta E_\nu}^{E_i+\Delta E_\nu} \mathrm{d}E_\nu \int_{\theta_0-\Delta\theta_1}^{\theta_0+\Delta\theta_2} \mathrm{d}\theta\,\phi(\theta) f_{\nu,\theta}(E_\nu,\theta) \equiv \int_{E_i-\Delta E_\nu}^{E_i+\Delta E_\nu} \mathrm{d}E_\nu\, f_E(E_\nu,\theta_0)\,, \tag{B.7}$$

where $\Phi_i(\theta_0)$ is the number of neutrinos detected in the $i^{\text{th}}$ energy bin (centered on neutrino energy $E_i$ and with width $2\Delta E_\nu$) and $\Phi_{\text{total}}$ is the total number of neutrinos produced by the pion beam. To approximate $f_E(E_\nu,\theta_0)$ as a gaussian distribution, we need to find the mean

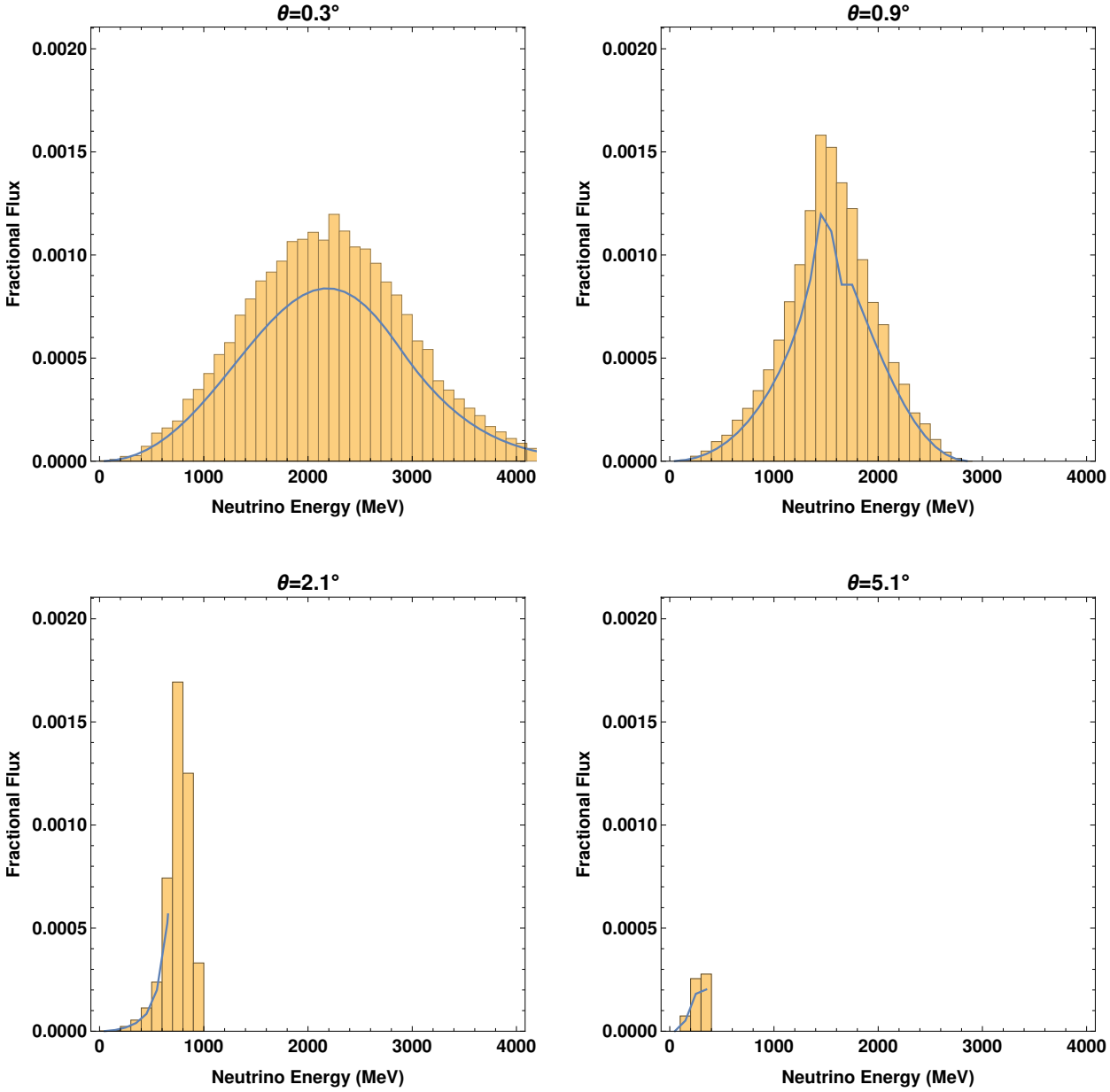


Figure B.2: Fraction of neutrinos from a pion beam having an energy contained in each 100 MeV wide energy bin and that are in line to go to a detector centered at the off-axis angles listed above each plot. The detector spans $\frac{\phi(\theta)}{2\pi} = \frac{1}{\pi}\sin^{-1}\left(\frac{1}{200\sin(\theta)}\right)$ of the space of azimuthal angles (at each value of $\theta$ covered by the detector) and $\frac{2\Delta\theta}{\pi} = \frac{0.6}{180}$ of the off-axis angles. The histogram is obtained from a simulation, and the curve is obtained using Eqs. (B.6) and (B.7).

($\bar{E}_\nu$) and standard deviation ($\sigma_\nu$) of $E_\nu$, using $f_E(E_\nu, \theta_0)$ as the probability density function, as follows:

$$\bar{E}_\nu = \langle E_\nu \rangle = \frac{1}{A} \int_0^\infty \mathrm{d}E_\nu \, E_\nu f_E(E_\nu, \theta_0) \,,$$

and

$$\sigma_\nu = \sqrt{\langle E_\nu^2 \rangle - \langle E_\nu \rangle^2} = \sqrt{\frac{1}{A} \int_0^\infty \mathrm{d}E_\nu \, E_\nu^2 f_E(E_\nu, \theta_0) - \bar{E}_\nu^2} \,,$$

where $A$ is the fraction of neutrinos produced by the pion beam that are in line to go to the detector, which is given by

$$A = \int_0^\infty \mathrm{d}E_\nu \, f_E(E_\nu, \theta_0) \,.$$

Then, the neutrino energy distribution would be approximated as

$$f_E(E_\nu, \theta_0) \approx \frac{A}{\sqrt{2\pi\sigma_\nu^2}} e^{-\frac{(E_\nu - \bar{E}_\nu)^2}{2\sigma_\nu^2}} \,. \tag{B.8}$$

Thus, the number of neutrinos we would expect in the $i^{\text{th}}$ energy bin, as long as the energy bins are sufficiently narrow, is approximated by

$$\Phi_i(\theta_0) \approx \Phi_{\text{total}} f_E(E_i, \theta_0)(2\Delta E_\nu) \,. \tag{B.9}$$

The results of using this approximation for various off-axis angles is shown in Fig. B.3 as the dotted lines.

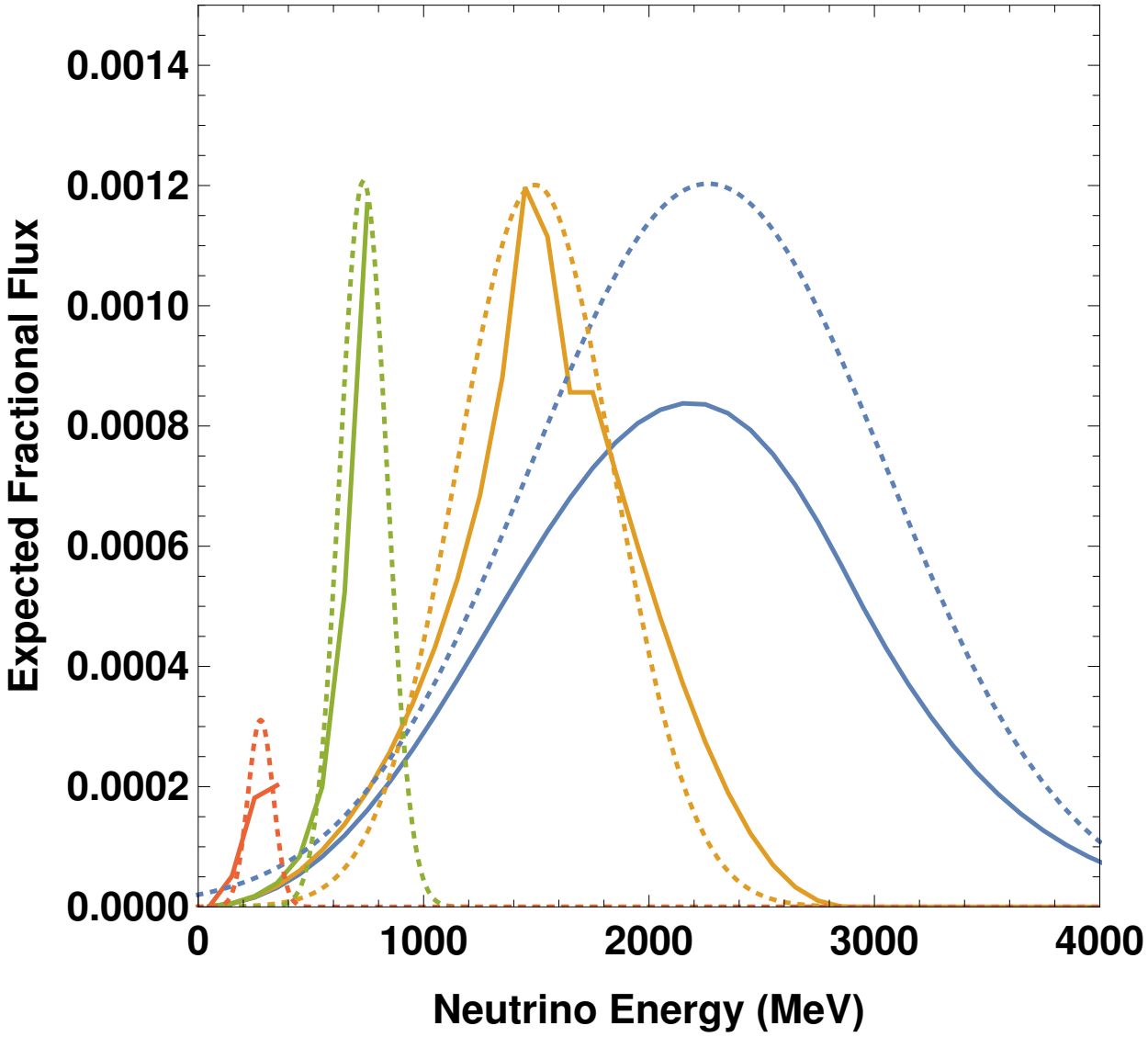


Figure B.3: Approximations of the fraction of neutrinos from a pion beam having an energy contained in each 100 MeV wide energy bin and that are in line to go to a detector centered at various off-axis angles. The detector spans $\frac{\phi(\theta)}{2\pi}$ of the space of azimuthal angles (at each value of $\theta$ covered by the detector) and $\frac{2\Delta\theta}{\pi} = \frac{0.6}{180}$ of the off-axis angles. The colors corresponding to the various off-axis angles are as follows: blue$\Rightarrow$ $\theta_0 = 0.3°$, orange$\Rightarrow$ $\theta_0 = 0.9°$, green$\Rightarrow$ $\theta_0 = 2.1°$, and red$\Rightarrow$ $\theta_0 = 5.1°$. The solid lines are obtained using equations B.6 and B.7 and the dotted black lines are obtained using equations B.8 and B.9.

# Appendix C

# Minimizing $\chi^2$ for JUNO Simulation

In GLoBES, the energy response ($R^I_\beta(E_\nu, E)$ from Eq. (1.18)) is implemented as a matrix called the smearing matrix [18]. Assuming the post-smearing efficiencies are approximately constant over each bin of reconstructed energy, we can take a sample of points throughout the relevant values of $E_\nu$ that are close enough together that $R^I_\beta$ (as well as the flux, oscillation probability, and interaction cross section) is approximately constant on intervals surrounding each sampling point, and define the smearing matrix for channel $c$ (corresponding to a neutrino of flavor $\beta$ interacting with the detector via an $I$ interaction) by

$$M^c_{in} \equiv \int_{E_i}^{E_{i+1}} \mathrm{d}E\, R^I_\beta(E_{\nu,n}, E)\,, \tag{C.1}$$

where the $i^{\text{th}}$ energy bin is given by $E_i \leq E \leq E_{i+1}$ and $E_{\nu,n}$ is the neutrino energy of the $n^{\text{th}}$ sampling point. In GLoBES, the energy response is assumed to be a Gaussian of the form

$$R^I_\beta(E_\nu, E) = \frac{1}{\sigma_c(E)\sqrt{2\pi}} e^{-\frac{(E_\nu - E)^2}{2(\sigma_c(E))^2}}\,, \tag{C.2}$$

where $\sigma_c(E)$ is the detector's energy resolution for channel $c$. We can determine the number of events detected in energy bin $i$ for channel $c$ (from Eq. (1.17); also called the post-smearing channel rates) with the following equation:

$$N_i^c \approx \sum_n M_{in}^c \phi_n^c \,, \tag{C.3}$$

where $\phi_n^c \approx f\Phi_\alpha(E_{\nu,n})P_{\alpha\to\beta}(E_{\nu,n})\sigma_\beta^I(E_{\nu,n})$ is the pre-smearing number of channel $c$ events for sampling point $n$.

In the case of JUNO, only electron antineutrinos are produced by the source, and the energy range being considered is below the threshold for being able to produce muons, so the only interactions being observed in the detector are electron antineutrino charged current interactions. Thus, there will be only be two event rate vectors: one for each detector.

## C.1 Spectral Nuisance Parameters

To add in the nuisance parameters corresponding to the uncertainty in the fine structure of the neutrino flux spectrum, we need to have a parameter multiplying the flux in each bin. As seen in the definition of $\phi_n^c$, $\Phi_\alpha(E_{\nu,n}) \to \xi_n\Phi_\alpha(E_{\nu,n}) \Rightarrow \phi_n^c \to \xi_n\phi_n^c$, where $\xi_n$ are the spectral nuisance parameters. So, let $\phi_n^D$ be the pre-smearing event rate for sample point $n$ in detector $D$ without modifying the flux, and let $M^D$ be the smearing matrix for detector $D$. Then, the modified post-smearing number of events in energy bin $i$ in detector $D$ is given by

$$N_i^D = \sum_n M_{in}^D \xi_n \phi_n^D \,. \tag{C.4}$$

We will use $N_i^{D,0}$ for the unmodified post-smearing event vector (i.e. same as the above equation, except with all the $\xi_n$ set to 1). In GLoBES, we use these $\xi_n$ as the pre-smearing

efficiencies. NOTE: All nuisance parameters are used in calculating the "fit" rates, not the "true" rates.

## C.2 Formula for $\chi^2$

The test statistic we will be using to determine how well our model fits the data is

$$\chi^2 = \sum_{i,D} \frac{\left(N^D_{\text{true},i} - N^D_{\text{fit},i}\right)^2}{N^D_{\text{true},i}} + \text{pull terms}\,, \tag{C.5}$$

where the "pull terms" inflict penalties on our test statistic when the oscillation parameters or nuisance parameters stray outside the boundaries of our prior knowledge of their values, as talked about in Section 1.2.4. We do not use any pulls on the spectral nuisance parameters, so $\xi_n$ does not appear in any of the pull terms, thus enabling us to neglect them when minimizing $\chi^2$ with respect to $\xi_n$.

## C.3 Minimizing $\chi^2$

To find the values of $\xi_n$ that minimize $\chi^2$ (while neglecting all other modifications to the fit rates), let us take the derivative of $\chi^2$ with respect to $\xi_n$ and set it equal to 0. Now,

$$\frac{\mathrm{d}N^D_{\text{fit},i}}{\mathrm{d}\xi_m} = \frac{\mathrm{d}}{\mathrm{d}\xi_m}\left[\sum_n M^D_{in}\xi_n\phi^D_{\text{fit},n}\right] = M^D_{im}\phi^D_{\text{fit},m}\,.$$

So, the values of $\xi_n$ that minimize $\chi^2$ are given by

$$\frac{\mathrm{d}\chi^2}{\mathrm{d}\xi_m} = \sum_{i,D} \frac{2\left(N^D_{\text{true},i} - N^D_{\text{fit},i}\right)}{N^D_{\text{true},i}} \frac{\mathrm{d}N^D_{\text{fit},i}}{\mathrm{d}\xi_m} = 0\,,$$

$$\Rightarrow \sum_n \left[ \sum_{i,D} \frac{M^D_{im} M^D_{in} \phi^D_{\text{fit},m} \phi^D_{\text{fit},n}}{N^D_{\text{true},i}} \right] \xi_n = \sum_{i,D} \frac{N^D_{\text{true},i} M^D_{im} \phi^D_{\text{fit},m}}{N^D_{\text{true},i}} \,. \tag{C.6}$$

Thus, we can use the matrix equation $\sum_n K_{mn}\xi_n = a_m$, where $K_{mn} = \sum_{i,D} \frac{M^D_{im} M^D_{in} \phi^D_{\text{fit},m} \phi^D_{\text{fit},n}}{N^D_{\text{true},i}}$ and $a_m = \sum_{i,D} \frac{N^D_{\text{true},i} M^D_{im} \phi^D_{\text{fit},m}}{N^D_{\text{true},i}}$, to solve for the $\xi_n$. This has to be solved every time the nuisance or oscillation parameters change (i.e. every time $\chi^2$ is calculated).